This thesis deals with an advanced experimental investigation of infrared radiation induced gyrotropic photocurrents in semiconductor nanostructures. These provide an access to non-equilibrium processes in low-dimensional materials like quantum wells allowing especially studies of spin and orbital properties of carriers. Even though a noticeable progress in both the basic research and utilisation of the gyrotropic currents has been achieved, their complete understanding is still a challenge. The conducted measurements improve the knowledge by revealing a number of new phenomena. Among them are a first experimental observation of circular photon drag effect demonstrating a simultaneous transfer of photon linear and angular momenta to carriers and a detection of a nonlinear magneto-gyrotropic photocurrent. The latter effect coheres with the heavy-hole type of the lowest conduction band in HgTe quantum wells allowing, for instance, determination of the quantum spin Hall insulator state.

Universitätsverlag Regensburg

ISBN 978-3-86845-051-4

gefördert von:

Alumni der physikalischen Fakultät der Universität Regensburg e.V.

Universität Regensburg

Dissertationsreihe Physik - Band 13

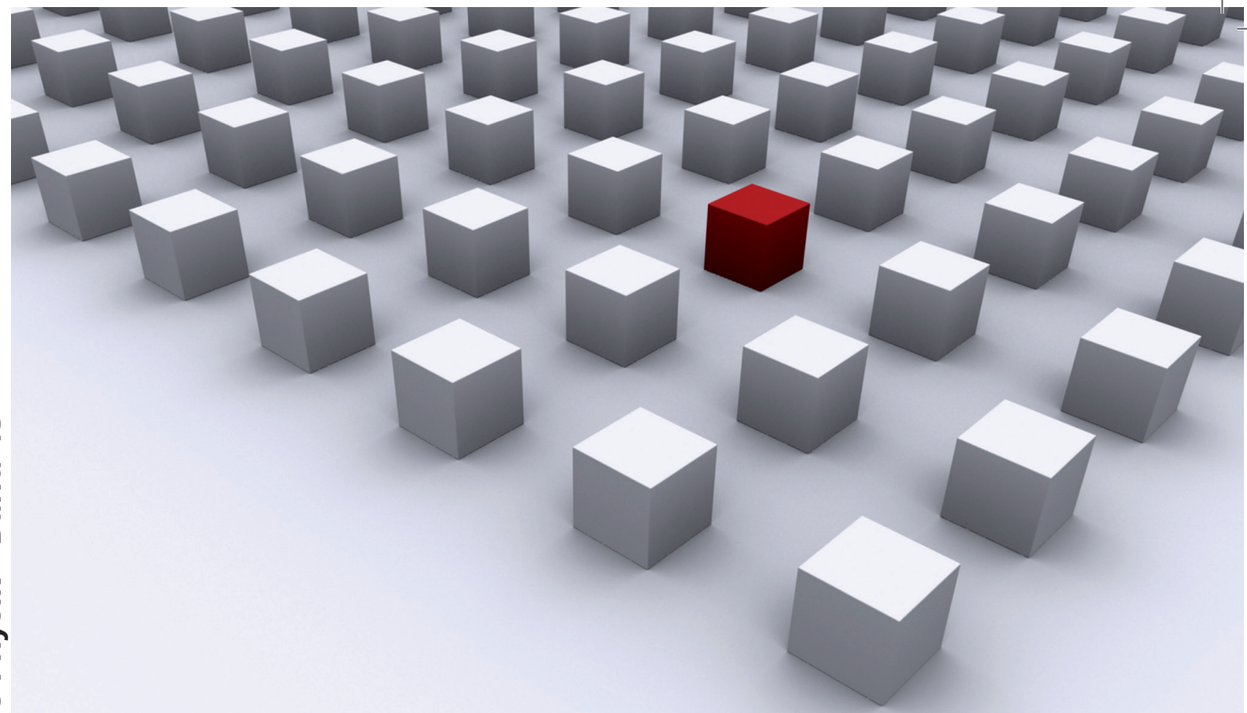

Helgi Diehl

Infrared Radiation Induced Gyrotropic Photocurrents in Semiconductor Nanostructures

Universitätsverlag Regensburg

Helgi Diehl

13

Dissertationsreihe Physik

Helgi Diehl

Infrared Radiation Induced Gyrotropic Photocurrents in Seminconductor Nanostructures

Infrared Radiation Induced Gyrotropic Photocurrents in Semiconductor Nanostructures

Dissertation zur Erlangung des Doktorgrades der Naturwissenschaften (Dr. rer. nat.) der naturwissenschaftlichen Fakultät II - Physik der Universität Regensburg vorgelegt von

Helgi Diehl

aus Odessa
Januar 2010

Die Arbeit wurde von Prof. Dr. S. Ganichev angeleitet.
Das Promotionsgesuch wurde am 12.01.2010 eingereicht.
Das Kolloquium fand am 10.03.2010 statt.

Prüfungsausschuss:	Vorsitzender:	Prof. Dr. M. Grifoni
	1. Gutachter:	Prof. Dr. S. Ganichev
	2. Gutachter:	Prof. Dr. Ch. Schüller
	weiterer Prüfer:	Prof. Dr. J. Zweck

Dissertationsreihe der Fakultät für Physik der Universität Regensburg, Band 13

Herausgegeben vom Präsidium des Alumnivereins der Physikalischen Fakultät:
Klaus Richter, Andreas Schäfer, Werner Wegscheider, Dieter Weiss

Helgi Diehl

Infrared Radiation Induced Gyrotropic Photocurrents in Semiconductor Nanostructures

Universitätsverlag Regensburg

Bibliografische Informationen der Deutschen Bibliothek.
Die Deutsche Bibliothek verzeichnet diese Publikation
in der Deutschen Nationalbibliografie. Detailierte bibliografische Daten
sind im Internet über http://dnb.ddb.de abrufbar.

1. Auflage 2010

Leibnitzstraße 13, 93055 Regensburg

Konzeption: Thomas Geiger
Umschlagentwurf: Franz Stadler, Designcooperative Nittenau eG
Layout: Helgi Diehl
Druck: Docupoint, Magdeburg
ISBN: 978-3-86845-051-4

Weitere Informationen zum Verlagsprogramm erhalten Sie unter:
www.univerlag-regensburg.de

Infrared Radiation Induced Gyrotropic Photocurrents in Semiconductor Nanostructures

DISSERTATION ZUR ERLANGUNG DES DOKTORGRADES DER NATURWISSENSCHAFTEN (DR. RER. NAT.)
DER FAKULTÄT II - PHYSIK

DER UNIVERSITÄT REGENSBURG

vorgelegt von

Helgi Diehl

aus

Odessa

im Jahr 2010

Promotionsgesuch eingereicht am: 12.01.2010
Die Arbeit wurde angeleitet von: Prof. Dr. S. Ganichev

Prüfungsausschuss:	Vorsitzender:	Prof. Dr. M. Grifoni
	1. Gutachter:	Prof. Dr. S. Ganichev
	2. Gutachter:	Prof. Dr. Ch. Schüller
	weiterer Prüfer:	Prof. Dr. J. Zweck

Contents

List of Figures

List of Tables

Chapter 1

Introduction

Transport of electrons and holes in semiconductor nanostructures belongs to key problems of the contemporary electronics [1, 2]. One of its major applications is the charge transfer for the sake of information processing. In the last decades, a significant progress in the enhancement of the operation capability has been achieved due to the decrease of RC time constants and minituarisation of the device fabrication [3]. Although the Moore's empirical law which describes the doubling of performance every 2 years is still valid [4], this development is faced with various problems. One of them is the ascending heating of structures accompanying the charge flow. Seeking for alternative solutions, another root of the information transduction can be realised exploiting the axial rotation quantum number of the electron, i.e., its spin, being a candidate for a qubit in quantum computers [5, 6]. The spin degree of freedom is utilised in the section of electronics called spintronics which is a rapidly developing field of modern physics regarding the basic research as well as its applications [7, 8]. An example of spin-dependent effects is the tunnel magnetoresistance in ferromagnetic metals which has been recently successfully implemented for information storage in non-volatile magnetic random access memories [9]. Developing spin-based logical components, besides spin injection and detection, the middle cornerstone builds a controlled spin manipulation. In semiconductors, this ability arises in low-symmetrical structures and is related to the gyrotropy of the material. This feature allows a linear coupling of polar and axial vectors and leads, for instance, to linear spin-orbit coupling terms in the Hamilton function [10, 11]. Discussing spin-dependent processes in nanostructures, one should mention the spin-orbit induced spin relaxation via D'yakonov-Perel' mechanism [12–14] as well as direct and inverse spin Hall effects [15–18]. Recently, different novel phenomena have attracted a considerable attention. Among them are spin-galvanic effect [19], zero-bias spin separation [20], circular photogalvanic effect [21–23] and quantum spin Hall effect [24, 25]. Although most phenomena are based on the spin-orbit coupling, the reduction of symmetry enables also spin-independent phenomena such as orbital circular photogalvanic effect [26, 27]. Photocurrents which require simultaneously gyrotropy and the presence of a magnetic field may be gathered in a class of magneto-optical phenomena denoted as magneto-gyrotropic photogalvanic effects [28, 29].

Gyrotropic and magneto-gyrotropic photocurrents have excelled in the fundamental research of the elementary processes of the electrons and holes in semiconductors as they allow a direct access

to spin and orbital properties of carriers. An extensive understanding of carrier basic principles becomes important for an efficient implementation of nanostructures in modern devices. While the features of the electron orbital motion are crucial for the electron transport, a comprehensive knowledge about spin properties is indispensable for the field of spintronics and its applications. One of such applications is the recently introduced all-electric polarisation detector which is based on the sensitivity of photocurrents to the polarisation state of the incident radiation [30,31]. Moreover, photocurrents have been successfully used for the characterisation of structures giving information on structure symmetry, doping level position, band structure and spin relaxation times (for review see [32, 33]). Even though a noticeable progress in both basic research and utilisation has been achieved, a complete understanding of photogalvanics is still a challenge.

The objectives of the present work are experimental studies of new photogalvanic effects in wide and narrow bandgap semiconductor nanomaterials such as n-type GaAs- and HgTe-based QW structures by means of mid-infrared and terahertz optical excitation. The reported results in GaAs structures comprise the observation of two novel phenomena under intersubband absorption of radiation: the circular photon drag effect and the resonant magneto-gyrotropic effect. Investigating narrow bandgap HgTe structures, a nonlinear magneto-induced photocurrent has been detected and is related to the inverted band structure where the ground conduction subband is of heavy-hole-type. Since the current is linear for normal band sequence, the method of magneto-gyrotropic photogalvanics can give a quick and reliable experimental feedback to theoretical calculations concerning band structure.

Chapter 2

Basics

Much current interest in condensed matter physics is directed towards understanding of carrier spin and orbital phenomena. An effective access to basic features of electrons and holes provide gyrotropic photocurrents. In the present chapter, various gyrotropic and magneto-gyrotropic photogalvanic effects are discussed. As it will be shown, these can originate from both asymmetrical spin-dependent as well as orbital processes in semiconductor nanostructures. Those photogalvanic effects which involve the spin of carriers are called spin photocurrents and require the $\boldsymbol{k}$-linear spin-orbit coupling. Independent of the current formation art, the generation ability of either photogalvanic effect is related to the gyrotropy. In the following section, starting with the standard band structure of bulk semiconductors this feature will be introduced as it removes the spin degeneracy by $\boldsymbol{k}$-linear terms in the effective Hamilton function creating a precondition for any further photocurrent treatment.

2.1 Band structure

Discussing electrical and optical properties of semiconductors, the basic knowledge of the band structure is indispensable. If one neglects the high-order effects such as strain and the spin-orbit interaction, the basic band structure of a direct bandgap bulk semiconductor can be imagined as shown in Fig. 2.1(a) where electron, heavy- and light-hole bands are spin degenerated [3]. Due to the fact, however, that quantum phenomena in semiconductors such as spin photocurrents are highly sensitive to subtle details of the carrier energy spectrum, this picture does not allow their correct description and should be modified. Below, an upgrade of the basic band structure owing to the relativistic effect of the spin-orbit interaction is considered. The latter leads to the removal of the spin degeneracy in low-symmetrical systems.

2.1.1 Removal of spin degeneracy

Step by step, moving from diamond to zinc blende bulk structures and over symmetric, finally, to asymmetric low-dimensional structures, the removal of the spin degeneracy by $\boldsymbol{k}$-linear terms in the Hamiltonian becomes apparent. Spin degeneracy of the electron bands in bulk semiconductors and subbands in heterostructures originates from the simultaneous presence of the spatial and time

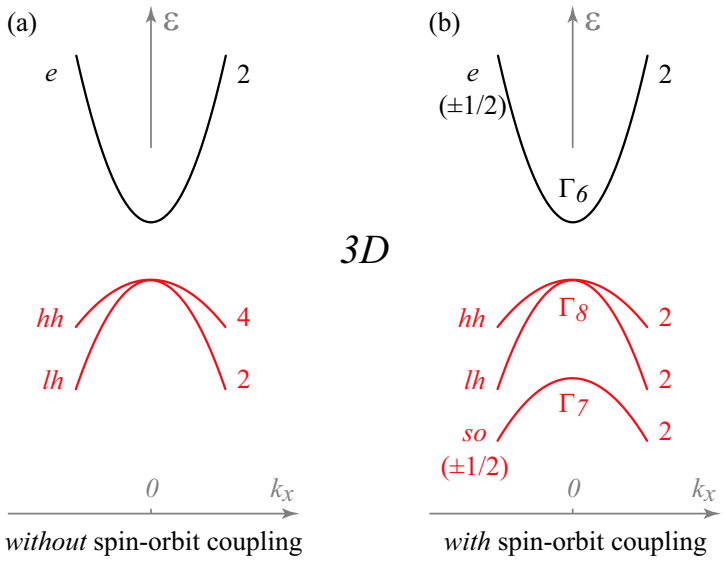

Figure 2.1: Electronic band structure of a bulk semiconductor with a direct bandgap both (a) neglecting and (b) accounting the spin-orbit interaction. Energy dispersions are sketched together with correspondent degeneracy numbers.

inversion symmetry [8]. Indeed, in bulk materials with only one sort of atoms (diamond cubic crystal structure) like bulk Si, the electron bands are spin degenerated. Here, the spatial inversion symmetry

$$E_\uparrow(\boldsymbol{k}) = E_\uparrow(-\boldsymbol{k}) \qquad \text{or} \qquad E_\downarrow(\boldsymbol{k}) = E_\downarrow(-\boldsymbol{k}) \tag{2.1}$$

together with the Kramers doublets due to the symmetry of the time reversal

$$E_\uparrow(\boldsymbol{k}) = E_\downarrow(-\boldsymbol{k}) \tag{2.2}$$

results in the spin degeneracy at any wave vector $\boldsymbol{k}$

$$E_\uparrow(\boldsymbol{k}) = E_\downarrow(\boldsymbol{k}). \tag{2.3}$$

From equations (2.1) and (2.2) it is obvious that there are two general ways to remove the spin degeneracy. An application of an external magnetic field $\boldsymbol{B}$ breaks the Kramers doublets in Eq. (2.2) and lifts the degeneracy of the spin states $\boldsymbol{\sigma}$ due to the Zeeman effect. This situation may be expressed by an additional term in the Hamiltonian as

$$H_Z = -(\boldsymbol{\sigma} \cdot \boldsymbol{B}). \tag{2.4}$$

Another possibility to remove the spin degeneracy arises in spatially asymmetric structures. In this context, two asymmetries should be mentioned: the bulk and structure inversion asymmetry. While the first one is an inherent feature of the host material, the latter appears due to any additional asymmetry in the particular structure.

Bulk Inversion Asymmetry (BIA)

In contrast to the diamond cubic, bulk zinc blende structures have 2 sorts of atoms and lack

the centre of inversion. This results in the so called Bulk Inversion Asymmetry (BIA). In bulk non-centrosymmetric structures belonging to the T_d point group, the spin-orbit interaction induces spin-dependent contributions to the conduction-band Hamiltonian starting with k^3 [32]

$$H_{\mathrm{BIA},3} = \kappa \left[\sigma_x k_x (k_y^2 - k_z^2) + \sigma_y k_y (k_z^2 - k_x^2) + \sigma_z k_z (k_x^2 - k_y^2)\right], \tag{2.5}$$

where σ_α are the Pauli matrices, κ is a pseudo-scalar and x, y, z indicate the space directions along the cubic axes

$$x \parallel [100], \quad y \parallel [010], \quad z \parallel [001]. \tag{2.6}$$

Although in materials of T_d symmetry the spin degeneracy is lifted by $\boldsymbol{k}$-cubic terms, the spin splitting of the conduction band along any cubic axis, however, is absent as shown in Fig. 2.1(b). Moreover, the generation of spin-dependent and orbital photocurrents remains forbidden as these are related to $\boldsymbol{k}$-linear splitting in gyrotropic media. The gyrotropy could be either the immanent property of a material or be induced extrinsically, for instance, by means of an externally applied magnetic field or uniaxial deformation [34]. Generally speaking, the gyrotropic point group symmetry makes no difference between components of axial vector $\boldsymbol{A}$ (e.g., spin, magnetic field, angular momentum) and polar vector $\boldsymbol{P}$ (e.g., momentum, electric current) and allows their linear coupling over the second-rank pseudotensor $\boldsymbol{T}$

$$P_l = T_{lm} A_m \tag{2.7}$$

Once the symmetry of the system is reduced to one of the gyrotropic crystal classes, the spin-dependent $\boldsymbol{k}$-linear terms in the Hamiltonian due to the spin-orbit interaction appear and can be written as

$$H_{SO} = \sum_{lm} \chi_{lm} \sigma_l k_m. \tag{2.8}$$

Such downgrade can be achieved experimentally in low-dimensional materials like zinc-blende-based QWs. For instance, (001)-grown GaAs *symmetrical* QW structures belong to the already gyrotropic D_{2d} point group symmetry. In the cubic coordinate system (2.6), the spin-orbit interaction excites $\boldsymbol{k}$-linear contributions given by [35]

$$H_{\mathrm{BIA},1} = \beta(\sigma_x k_x - \sigma_y k_y), \tag{2.9}$$

where pseudo-scalar β is the Dresselhaus linear coupling parameter. It is quiet obvious that BIA-induced $\boldsymbol{k}$-linear splitting can be easily derived from the Eq. (2.5) for the bulk material taking into account the quantum confinement of the QW structure $\left(\beta = -\kappa \langle k_z^2 \rangle\right)$.

Structure Inversion Asymmetry (SIA)

Besides Bulk Inversion Asymmetry, both unrequested or intended on purpose additional asymmetries in structures result in the so called Structure Inversion Asymmetry (SIA). This can originate from a lattice stress, atom diffusion in the epitaxially grown structures, inhomogeneity due to an externally applied electric field, doping asymmetry and so on. As a result of the SIA contribution, (001)-grown GaAs QW structures become *asymmetrical* belonging now to the C_{2v} point group symmetry and the corresponding linear-in-$\boldsymbol{k}$ contributions to the Hamiltonian are given by [36]

$$H_{\mathrm{SIA},1} = \alpha(\sigma_x k_y - \sigma_y k_x), \tag{2.10}$$

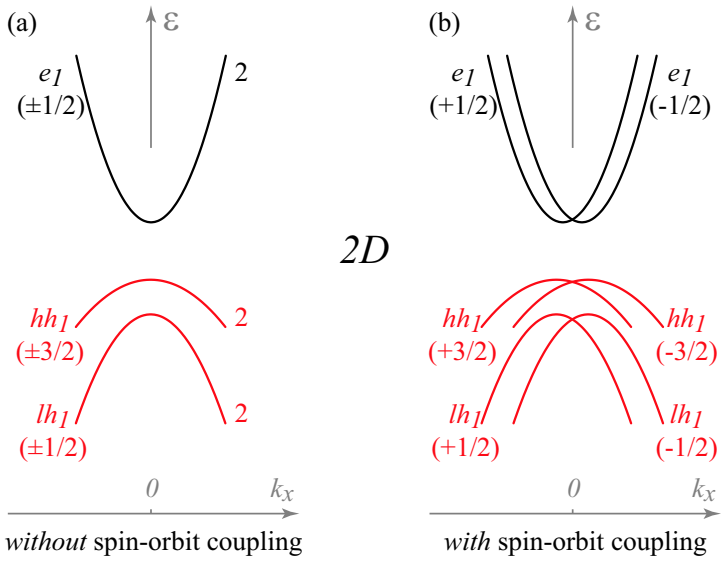

Figure 2.2: Electronic band structure of two-dimensional material like QW structure both (a) neglecting and (b) accounting the spin-orbit interaction. In the case of zinc-blende-based structures, the electron, heavy- and light-hole energy dispersions become spin-split due to $\boldsymbol{k}$-linear terms given by general Eq. (2.8).

where pseudo-scalar α is the Rashba parameter. Since all structures under investigation are asymmetrical QWs, thus calculating the band energy splitting, a combination of both BIA and SIA contributions must be taken into account. The relative shift $\Delta(\boldsymbol{k})$ of the spin-split sublevels in the energy spectrum is given by [37]

$$\Delta(\boldsymbol{k}) = 2|\boldsymbol{k}|\sqrt{\alpha^2 + \beta^2 + 2\alpha\beta\sin 2\theta_{\boldsymbol{k}}}, \tag{2.11}$$

where $\theta_{\boldsymbol{k}}$ is an angle between $\boldsymbol{k}$ and the cubic x axis. The interference term on the rhs of (2.11) causes anisotropy of the energy dispersions $E(\boldsymbol{k})$ in the QW plane. Assuming a particular case $\alpha = \beta$, electrons moving in $[1\bar{1}0]$ direction are spin-degenerated, while those with the wave vector $\boldsymbol{k}$ in [110] direction feature the maximum possible value of the energy splitting. Figures 2.2(a) and (b) sketch qualitatively the $\boldsymbol{k}$-linear spin splitting of the electron and hole subbands in 2-dimensional structures while the effect of the size quantisation separates energetically the light and heavy hole states at the Γ-point [3]. Since in the absence of an external magnetic field the Kramers doublets are conserved, the energetic parabolas shift symmetrically in respect to $k = 0$ and their relative shift Δ is given by Eq. (2.11). It should be noted that in real structures the energy dispersions $E(\boldsymbol{k})$ of the conduction band become nonparabolical, for instance, due to the admixture of the valence band, and the shift given by Eq. (2.11) remains valid for small values of $\boldsymbol{k}$ only.

2.1.2 Effective magnetic field

Comparison of the mathematical expressions (2.4), (2.9) and (2.10) for spin splittings induced by external magnetic field and BIA/SIA terms suggests to express the removal of the spin degeneracy

by either spatial asymmetry similar to the Zeeman splitting in terms of the *effective* magnetic field. As an example, for (001)-grown asymmetrical zinc-blende-based QWs, the $\boldsymbol{k}$-linear effective magnetic fields $\boldsymbol{B}^{\text{eff}}$ caused by BIA and SIA are given by

$$\begin{aligned} \boldsymbol{B}^{\text{eff}}_{\text{BIA},1} &= \beta\,(k_x, -k_y, 0)\,, \\ \boldsymbol{B}^{\text{eff}}_{\text{SIA},1} &= \alpha\,(k_y, -k_x, 0)\,. \end{aligned} \tag{2.12}$$

Before pointing out the benefits of such representation, first, several important differences between effective and real magnetic fields should be mentioned. As it can be seen from the equation array (2.12), the effective field $\boldsymbol{B}^{\text{eff}}$ acting on the spin of a particular electron depends on the momentary wave vector $\boldsymbol{k}$ of the electron itself. Moreover, in contrast to the external magnetic field, its effective counterpart $\boldsymbol{B}^{\text{eff}}$ does not break the time reversal symmetry. However, an introduction of such a field appears to be very useful, since both spin splitting and dynamics within it can be described similar to that in a real magnetic field. Indeed, the spin splitting originating from either spatial asymmetry can be written as

$$H_{SO} = \left(\boldsymbol{\sigma} \cdot \boldsymbol{B}^{\text{eff}}(\boldsymbol{k})\right). \tag{2.13}$$

and by any means injected non-equilibrium electron spin $\boldsymbol{S}$ starts precessing around the vector $\boldsymbol{B}^{\text{eff}}(\boldsymbol{k})$ with the frequency

$$|\boldsymbol{\Omega}(\boldsymbol{k})| = \frac{2}{\hbar}\left|\boldsymbol{B}^{\text{eff}}(\boldsymbol{k})\right|. \tag{2.14}$$

This spin precession will play in the following investigations of the spin phenomena an important role as it influences directly the spin polarisation providing a tool of the spin manipulation. Indeed, at small values of Ω the effective magnetic field rotates the non-equilibrium spin at an average angle generating a nonzero orthogonal spin component and, therefore, acts as an inductor of the spin. On the other side, it is the driving force of an efficient spin dephasing mechanism.

2.2 D'yakonov-Perel' spin relaxation mechanism

The precession of the spin polarisation in the effective magnetic field between scattering events is the basis of the spin depolarisation in the terms of the D'yakonov-Perel' (DP) spin relaxation theory [12–14]. The DP mechanism dominates in n-type low-dimensional wide bandgap structures with inherent spin splitting like GaAs-based QW structures [38]. At high frequencies, $\Omega > 1/\tau_p$, the transversal component of the spin vanishes before the first momentum scattering event, i.e., $\tau_s \propto \tau_p$. In the opposite limiting case, $\Omega < 1/\tau_p$, the angular rotation between elementary scattering events is small and the spin relaxation is a result of successive accidental small precessions. Indeed, as the orientation of $\boldsymbol{\Omega}$ depends on the momentary wave vector $\boldsymbol{k}$ of the electron after every stochastic scattering event (see equations (2.12) and (2.14)), the DP spin relaxation mechanism becomes anisotropic. In the collision-dominated regime, which holds in typical III-V-based semiconductors, one obtains the condition $\Omega\tau_p \ll 1$ [39]. The resultant spin relaxation time is, therefore, reciprocally proportional to the scattering time τ_p [12]

$$\tau_s \propto \frac{C}{\langle \boldsymbol{\Omega}^2(\boldsymbol{k})\,\tau_{\text{p}}\rangle} \tag{2.15}$$

with C given by [39]

$$C^{-1} = \frac{(k_B T)^3}{E_g}. \tag{2.16}$$

As it is seen from the equations (2.15) and (2.16), the spin dephasing occurs between the scattering events and becomes longer at low temperatures and in wide bandgap materials. Moreover, the DP spin relaxation mechanism may be even suppressed for specific directions of the electron momentum and spin by an appropriate choice of the confinement axis as it has been demonstrated on the example of (110)-grown GaAs-based QWs [14, 40].

2.3 Gyrotropic Photogalvanic Effects

In the first section of this chapter, it has been shown that the reduction of symmetry by introduction of low-dimensional materials influences the electronic band properties. The modification of the carrier energy spectrum by $\boldsymbol{k}$-linear terms enables a wide class of photogalvanic phenomena called gyrotropic photocurrents. These currents arise in low-symmetrical homogeneous structures due to a uniform illumination. For instance, absorption of a circularly polarised light in zinc-blende-based QWs may lead to current generation due to circular photogalvanic effect [21] and optically induced spin-galvanic effect [19]. In either case, a characteristic feature of these photocurrents, which occur in unbiased samples, is that both currents reverse their direction upon changing the radiation helicity from left-handed to right-handed and vice versa. However, one of the principal differences between these helicity-dependent effects is their temporal behaviour. While current caused by the circular photogalvanic effect decays with the momentum relaxation time of free carriers, the spin-galvanic effect induced current is limited by the relaxation time of the non-equilibrium spin in the system.

2.3.1 Circular Photogalvanic Effect

The Circular Photogalvanic Effect (CPGE) was predicted in [41, 42] and then observed in bulk tellurium applying mid-infrared laser radiation [43]. The effect has been entirely investigated in different materials like GaAs [44, 45], InAs [21], SiGe [46], HgTe [31, 47], strained InGaAs QWs [22, 23], GaN/AlGaN heterojunctions [48, 49] as well as Si-MOSFETs [27] and could be utilised in different applications like in all-electric polarisation detectors [30, 31] and experimental separation of Rashba and Dresselhaus spin splittings [50]. The CPGE can be imagined as a transfer of an angular momentum of a photon into a directed motion of free carriers. This process is comparable in conventional life, for instance, with a rotating motion of a screwdriver while moving straightforward. Similar to the removal of the spin degeneracy by the $\boldsymbol{k}$-linear terms in the Hamilton function, the CPGE is allowed in gyrotropic structures only. Neither in bulk diamond crystals like Si and Ge nor in bulk structures of zinc-blende-type the appearance of the CPGE is possible. However, in nanostructures like GaAs QWs the CPGE is enabled due to the reduction of symmetry.

General phenomenological description

Without any knowledge about the microscopic processes leading to the current formation, on the

phenomenological level the CPGE current $\boldsymbol{j}$ can be described by [41]

$$j_\lambda = \sum_\rho \gamma_{\lambda\rho}\, \hat{e}_\rho E^2 P_{\mathrm{circ}}, \tag{2.17}$$

where $\boldsymbol{\gamma}$ is the second-rank pseudotensor coupling the dc electric current $\boldsymbol{j}$ and the radiation propagation direction given by the unity vector $\hat{\boldsymbol{e}}$. Maybe the most characteristic fingerprint of this gyrotropic photocurrent is its proportionality to the radiation helicity P_{circ} given by

$$P_{\mathrm{circ}} = \frac{I(\sigma^+) - I(\sigma^-)}{I(\sigma^+) + I(\sigma^-)}, \tag{2.18}$$

where $I(\sigma^+)$ and $I(\sigma^-)$ are intensities of right- and left-handed circularly polarised light, respectively. Light helicity P_{circ} can be considered as a normed average spin projection of photons on their propagation direction: $(\boldsymbol{S}_{ph}\cdot\hat{\boldsymbol{e}})/\hbar$. Therefore, for completely right-handed (σ^+) or left-handed (σ^-) circularly polarised light the helicity P_{circ} is equal to $+1$ or -1, respectively. Following the phenomenological Eq. (2.17), the CPGE arises under illumination with circularly or elliptically polarised light only. Moreover, the photocurrent $\boldsymbol{j}$ is determined by the point group symmetry, which discloses the non-vanishing components of the pseudotensor $\boldsymbol{\gamma}$ for a certain coordinate system. In respect to the helicity-dependent photogalvanic experiments carried out on (110)-oriented asymmetrical QWs, in the following phenomenological and microscopical discussion, the description of the CPGE is given for the case of the relevant C_s point group.

Phenomenological description in C_s-Symmetry

The asymmetric (110)-oriented GaAs/GaAlAs QW structures under investigation belong to media of C_s point group symmetry which corresponds to the monoclinic-domatic crystal class. The C_s point group has only two symmetry elements: (E, σ_h), the identity operator and the $(1\bar{1}0)$ reflection plane [51]. It is convenient to use the coordinate system along the crystallographic axes

$$x'' \parallel [1\bar{1}0], \quad y'' \parallel [00\bar{1}], \quad z'' \parallel [110], \tag{2.19}$$

where the x'' and y'' lie in the plane of the QW and z'' is the structure growth direction. The projections of the CPGE current on the both in-plane directions for the arbitrary aligned light in respect to the interface plane are then given by [33]

$$j_{x''} = \left(\gamma_{x''y''}\, \hat{e}_{y''} + \gamma_{x''z''}\, \hat{e}_{z''}\right) I P_{\mathrm{circ}} \qquad \text{and} \qquad j_{y''} = \gamma_{y''x''}\, \hat{e}_{x''} I P_{\mathrm{circ}}, \tag{2.20}$$

where the intensity is set as $I = E_0^2$. While the tensor component $\gamma_{x''z''}$ arises due to the BIA of the low-dimensional structure, components $\gamma_{x''y''}$ and $\gamma_{y''x''}$ are due to the SIA and present in asymmetric QWs only. For instance, normal incidence illumination ($\hat{e}_{x''} = \hat{e}_{y''} = 0$) yields CPGE current in the direction x'' which is normal to the symmetry reflection plane $(1\bar{1}0)$. Below, the spin-dependent microscopic mechanism of the current formation under normal excitation is given.

Microscopical description in C_s-Symmetry

Up to the present, several microscopic mechanisms of the CPGE have been proposed. The latest one is the pure orbital mechanism which is based on the interference of different pathways contributing to the light absorption [26]. It does not involve the spin of carriers and is expected to

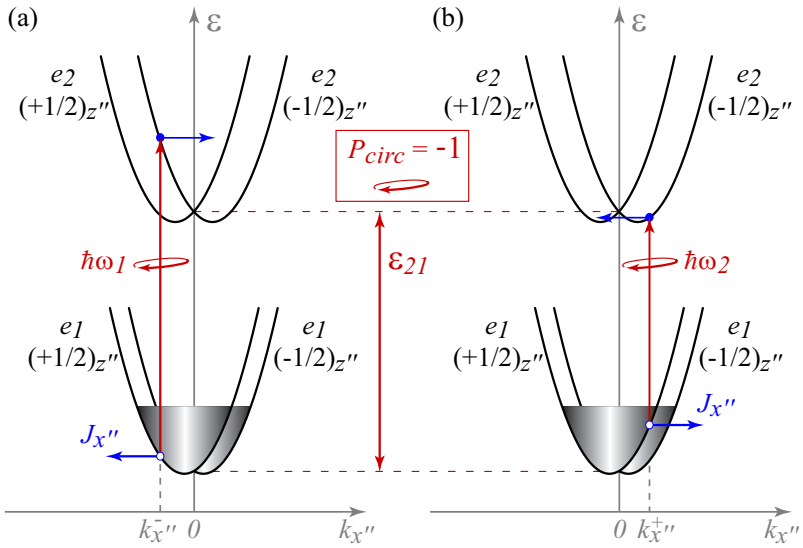

Figure 2.3: Mechanism of the CPGE current at intersubband resonance induced by the normal incident circularly polarised radiation in structures of C_s-symmetry.

be the predominant in the Drude-like absorption range. However, the experimental observation of CPGE under intersubband resonant absorption of mid-infrared light suggests to introduce here the intersubband dominating spin-related model [45] which is the original one and bases on the spin-orbit splitting.

In (110)-oriented QW structures of C_s point group symmetry the electron spin degeneracy along the growth direction (z'') is lifted by spin-orbit coupling,

$$H_{\rm SO} = \beta_{z''x''}\,\sigma_{z''}k_{x''}, \tag{2.21}$$

where $\beta_{z''x''}$ is the Dresselhaus spin splitting constant. As a result, the conduction band splits in two sublevels with the spin components $\sigma_{z''} = \pm 1/2$ as given by

$$\varepsilon_{\nu,\pm 1/2}(k_{x''}) = \varepsilon^{(\nu)} + \frac{\hbar^2 k_{x''}^2}{2m^*} \pm \beta^{(\nu)}_{z''x''}k_{x''}, \tag{2.22}$$

where the $\varepsilon^{(\nu)}$ is the energy of size-quantised subbands and $\nu = 1, 2$ denominates the first and the second subband, respectively. Irradiation of the material with a polarised light leads to an intersubband absorption in the structure. However, it occurs only if energy and momentum conservation laws as well as optical selection rules are satisfied. For example, a single photon with helicity $P_{\rm circ} = -1$ and energy $\hbar\omega_1$ can be absorbed only by a certain electron with the spin $\sigma_{z''} = +1/2$ and quasi-momentum $k^-_{x''}$ as shown in Fig. 2.3(a). As a result, under normal incidence a spin-flip transition from the ground conduction subband e_1 to the upper subband e_2 occurs [52] and the angular momentum conservation relation

$$\sigma^{e_1}_{z''} + P_{\rm circ} = \sigma^{e_2}_{z''} \tag{2.23}$$

is fulfilled. The non-uniform electron distributions in *both* subbands originating from the depleted electron state (quasi-hole) in the ground subband e_1 and the created electron state in the upper

subband e_2 drive currents of the same magnitude ($|k^-_{x''}|$) but opposite signs compensating each other. However, for the typical n-type QW structures the contribution from the electrons in the upper subband e_2 to the total current is temporally controlled by the fast emission of the LO-phonons[1]. Therefore, the electric current in x'' direction is determined by the spin polarised (here: $\sigma_{z''} = +1/2$) quasi-holes in the ground subband e_1 and decays with the momentum relaxation time $\tau_p^{(1)}$. From the angular momentum selection rule (2.23), it is obvious that switching helicity from $+1$ to -1 the whole picture mirrors and the current inverts its direction. Holding the helicity constant and scanning the photon energy around the intersubband resonance maximum ε_{21}, the current changes its sign as well while passing the frequency $\varepsilon_{21}/\hbar$ (see Fig. 2.3(b)). These qualitative features of the CPGE current as well as an essential need of the spin splitting are reflected in the following expression for the averaged CPGE current

$$\bar{j}_{x''} \propto (\beta^{(1)}_{z''x''} + \beta^{(2)}_{z''x''})\tau_p^{(1)} \frac{d\bar{\eta}_{\|}(\hbar\omega)}{d\hbar\omega} I P_{\mathrm{circ}} \tag{2.24}$$

where $\bar{\eta}_{\|}$ is the averaged intersubband absorbance of the normally incident light[2], I is the light intensity and $\beta^{(1,2)}_{z''x''}$ the spin splitting constants of the first and second electron subband, respectively. At pulsed excitation, the CPGE current vanishes with the momentum relaxation time $\tau_p^{(1)}$, i.e., the time is needed to achieve the uniform distribution of the photoexcited carriers in $\boldsymbol{k}$-space. However, if the spin relaxation time $\tau_s^{(1)}$ is longer than the $\tau_p^{(1)}$ and some general symmetry requirements are met, than the uniformly distributed but still spin polarised electrons may give rise to an electric current due to the spin-galvanic effect.

2.3.2 Spin-galvanic Effect

Spin-galvanic effect (SGE), predicted in [34], has been observed for the first time in n-type GaAs QWs by means of optical spin orientation [19] and thus belongs to the class of spin-related photocurrents. Even though the optical way of spin injection is a natural one, the method itself, however, is not crucial. Indeed, by any means induced uniform non-equilibrium spin polarisation $\boldsymbol{S}$ may give rise to an electric current $\boldsymbol{j}$,

$$j_\alpha = \sum_\beta Q_{\alpha\beta} S_\beta \,, \tag{2.25}$$

where $\boldsymbol{Q}$ is a second-rank pseudotensor. In every particular material, the non-equilibrium spin S_β may drive an electric current j_α if the relevant coupling pseudotensor component $Q_{\alpha\beta}$ is not equal to zero. In general, non-vanishing components of the SGE tensor $\boldsymbol{Q}$ can only exist in non-centrosymmetric systems belonging to one of the gyrotropic classes. Regarding the experimental investigations, two relevant symmetry classes should be mentioned. In (001)-grown asymmetrical GaAs-based QWs belonging to the C_{2v} point group, the nonzero components in the cubic coordinate system are Q_{xy} and Q_{yx}. As a result, in such structures only in-plane spin polarisation may drive an electric current. In contrast to (001)-oriented QWs, the (110)-oriented asymmetrical QWs allow

[1] Energy of LO-phonons in n-GaAs QWs is about 35 meV.

[2] The resonant intersubband absorbance of the normally incident light is known to be forbidden by the dipole selection rules [53, 54]. However, these rules were shown to be not rigorous [55].

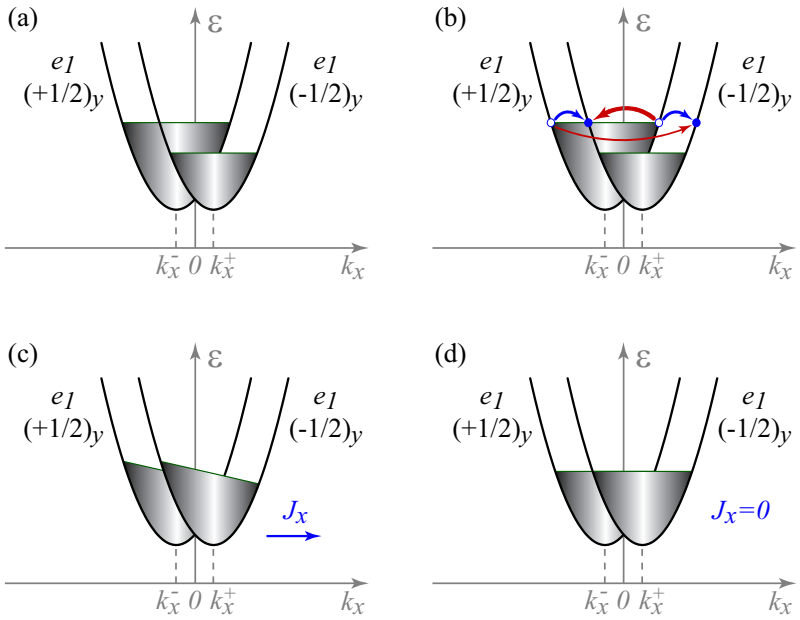

Figure 2.4: Mechanism of the spin-galvanic effect based on the asymmetry of the spin-flip relaxation processes in the $\boldsymbol{k}$-space.

conversion of even out-of-plane spin component in a dc current. The latter nanomaterials are related to the C_s symmetry and possess in the double-prime coordinate system (2.19) three non-vanishing components $Q_{x''y''}$, $Q_{y''x''}$ and $Q_{x''z''}$. Microscopically, two models of the SGE current formation exist. The newest one bases on the combination of the anisotropy of spin-preserving and spin-flip scattering and is expected to be the predominant at room temperature [56]. In a much simple way, however, microscopic picture of SGE can be understood in terms of the originally proposed mechanism. This is due to the asymmetry of the spin-flip relaxation processes in the $\boldsymbol{k}$-space [19].

Spin-galvanic effect due to asymmetry of the spin-flip relaxation

Injection of non-equilibrium spin in a system activates relaxation processes tending to an equilibrium situation. In general, these processes do not lead to electric current generation. However, in media with a spin non-degenerated electron gas, relaxation of the spin polarisation can drive an electric current. In addition, both spin-up and spin-down subbands should be shifted linearly in $\boldsymbol{k}$-space. This requirement is satisfied in all nanostructures used in the experiments. Figure 2.4(a) demonstrates the subband shift in the $\boldsymbol{k}$-space along x together with the uniform non-equilibrium spin polarisation S_y. In this band structure, spin polarisation means that one subband is occupied up to higher energies than the another. On their way to the equilibrium, electrons from the higher filled subband (spin-up) scatter to the less filled subband (spin-down) performing a spin-flip. In this respect, four quantitatively different events exist and are shown in Fig. 2.4(b) by bent arrows. Since the electron scattering rate depends on the values of the wave vectors of the initial and final states, an asymmetry of relaxation processes arises. Although transitions shown by blue arrows have the same rates preserving the uniformity of the electron populations in the both subbands,

scattering events sketched by thick and thin red arrows depopulate the right branch of the spin-up subband while preferably populating the left branch of the spin-down subband. The resulting non-uniform distribution of the electrons in the $\boldsymbol{k}$-space after these elementary spin-flip events is shown qualitatively in Fig. 2.4(c). The current of electrons starts flowing in x direction and decays for the already spin relaxed electrons with the momentum relaxation time $\tau_p^{(1)}$ [57]. However, new spin-flip processes will occur as far the electron gas is still spin polarised and, therefore, the total SGE current decays with the spin relaxation time $\tau_s^{(1)}$. Within the model of the elastic scattering, the electric current caused by the non-uniform distribution of the electrons shown in Fig. 2.4(c) is not spin polarised because the same number of the spin-up and spin-down electrons move in the same direction with the same velocity. The situation of the relaxed sublevels is shown in the Fig. 2.4(d) whereas the current vanishes.

2.4 Magneto-Gyrotropic Photogalvanic Effects

In contrast to photocurrents caused by circular photogalvanic and spin-galvanic effects, magneto-gyrotropic photogalvanic effects (MGPGE) allow current generation in homogeneously illuminated structures only if an external magnetic field $\boldsymbol{B}$ is applied. After the first experimental report on circular MGPGE in [58], an essential progress has been achieved. The effect has so far been detected in GaAs, InAs, GaN and SiGe QWs (for a review see [29]) and applied for characterisation of structures giving information on structure symmetry and doping level position [59, 60]. On the macroscopical level, within the linear approximation in the magnetic field strength B, the MGPGE current is given by [33]

$$j_\alpha = \sum_{\beta\gamma\delta} \phi_{\alpha\beta\gamma\delta} B_\beta \left\{E_\gamma E_\delta^\star\right\} + \sum_{\beta\gamma} \mu_{\alpha\beta\gamma} B_\beta \hat{e}_\gamma E_0^2 P_{\rm circ}. \tag{2.26}$$

Here, the fourth-rank pseudotensor $\boldsymbol{\phi}$ is symmetric in the last two indices, $\phi_{\alpha\beta\gamma\delta} = \phi_{\alpha\beta\delta\gamma}$, E_γ are components of the complex amplitude of the radiation electric field $\boldsymbol{E}$ which is presented as $\boldsymbol{E} = E_0\boldsymbol{e}$ with E_0 being the modulus $|\boldsymbol{E}|$ and $\boldsymbol{e}$ indicating the polarisation unit vector. The symbol $\{E_\gamma E_\delta^\star\}$ means the symmetrised product of the electric field with its complex conjugate

$$\left\{E_\gamma E_\delta^\star\right\} = \frac{1}{2}\left(E_\gamma E_\delta^\star + E_\delta E_\gamma^\star\right). \tag{2.27}$$

In the second term on rhs of Eq. (2.26), μ is a regular third-rank tensor, $P_{\rm circ}$ is the helicity of the radiation and $\hat{\boldsymbol{e}}$ is the unit vector pointing in the direction of light propagation. While the second term requires elliptically polarised light, the first term may be nonzero even for unpolarised radiation.

In the present work, MGPGE photocurrents have been investigated in (001)- and (013)-oriented QWs. While the latter belongs to the C_1 point group possessing only the identity as a symmetry operation and, therefore, provides the highest possible number of the non-vanishing components of the pseudotensor ϕ and regular tensor μ, the phenomenological picture can, however, be specified for (001)-grown asymmetrical QWs which are related to the C_{2v} symmetry. In this case, it is convenient to use the prime coordinate system

$$x' \parallel [1\bar{1}0], \quad y' \parallel [110], \quad z' \parallel [001], \tag{2.28}$$

S_1	=	$\frac{1}{2}\left(\phi_{x'y'x'x'}+\phi_{x'y'y'y'}\right)$	T_1	=	$\frac{1}{2}\left(\phi_{y'x'x'x'}+\phi_{y'x'y'y'}\right)$
S_2	=	$\frac{1}{2}\left(\phi_{x'y'x'x'}-\phi_{x'y'y'y'}\right)$	T_2	=	$\frac{1}{2}\left(\phi_{y'x'x'x'}-\phi_{y'x'y'y'}\right)$
S_3	=	$\phi_{x'x'x'y'}=\phi_{x'x'y'x'}$	T_3	=	$\phi_{y'y'x'y'}=\phi_{y'y'y'x'}$
S_4	=	$\mu_{x'x'z'}$	T_4	=	$\mu_{y'y'z'}$

Table 2.1: Definition of the parameters S_i and T_i ($i=1...4$) in Eq. (2.29) in terms of the non-vanishing components of the pseudotensor ϕ and the regular tensor μ for the C_{2v} symmetry in the prime coordinate system (2.28) under assumption of normally incident light [28].

where x' and y' are oriented along the crystallographic axes in the QW plane and z' is the growth direction. For the normally incident light and the magnetic field oriented in the interface plane of the QW, the intensity normed projections of the MGPGE photocurrent on both in-plane directions x' and y' are then given by [28]

$$\begin{aligned} j_{x'}/I &= S_1 B_{y'} + 2S_2 B_{y'} P_{\rm lin} + 2S_3 B_{x'} P'_{\rm lin} + S_4 B_{x'} P_{\rm circ}, \\ j_{y'}/I &= T_1 B_{x'} + 2T_2 B_{x'} P_{\rm lin} + 2T_3 B_{y'} P'_{\rm lin} + T_4 B_{y'} P_{\rm circ}, \end{aligned} \tag{2.29}$$

where, again for simplicity, the intensity is set to be $I=E_0^2$. The coefficients S_1 to S_4 and T_1 to T_4 expressed in terms of non-vanishing components of tensors ϕ and μ in the C_{2v} symmetry group are given in Tab. 2.1. The set $P_{\rm lin}$, $P'_{\rm lin}$ and $P_{\rm circ}$ are Stokes parameters describing the polarisation state of the light. While the latter parameter $P_{\rm circ}$ is the light helicity given by Eq. (2.18), $P_{\rm lin}$ and $P'_{\rm lin}$ describe the degree of linear polarisation and are defined via polarisation unit vector components as

$$\begin{aligned} P_{\rm lin} &\equiv \frac{1}{2}\left(|e_{x'}|^2 - |e_{y'}|^2\right), \\ P'_{\rm lin} &\equiv \frac{1}{2}\left(e_{x'}e^{\star}_{y'} + e_{y'}e^{\star}_{x'}\right). \end{aligned} \tag{2.30}$$

From the equation set (2.29) it can be seen that the terms described by S_1 and T_1 are polarisation-independent and appear even at illumination with unpolarised light. However, all other contributions on the rhs of (2.29) require either linear (S_2,T_2 and S_3,T_3) or circular (S_4,T_4) radiation polarisation. For the case of the elliptically polarised light all current contributions are present. Studying MGPGE currents in a particular nanostructure, observation of the polarisation dependences is an important investigation tool as it helps to conclude on the microscopic origin of the observed signal.

Microscopically, there are different mechanisms for involving magnetic field in the current formation processes. In the case of orbital (diamagnetic) mechanisms, the magnetic field $\boldsymbol{B}$ acts on the orbital motion of the electrons $\boldsymbol{k}$ rather than on their spin and induces a directed electron flow. Basically, diamagnetic mechanisms originate from the Lorentz force, which pushes electrons to the right or the left interface depending on their velocity direction and, therefore, changes their electron wave function and energy. Since the Lorentz force is proportional to the magnetic field and the electron velocity, the resulting small diamagnetic corrections to the wave function and energy are linear in $\boldsymbol{k}$ as well as linear in $\boldsymbol{B}$. However, these $\boldsymbol{k}$-linear corrections arise similar to $\sigma_l k_m$-terms

in gyrotropic materials only. Below, linear-in-$\boldsymbol{k}$ corrections caused by SIA are considered. The corresponding contribution to the effective Hamiltonian induced by the in-plane magnetic field has in the prime coordinate system (2.28) the form [53]

$$H_{\rm dia}^{\rm SIA} = \frac{\hbar e}{m^* c}(B_{x'}k_{y'} - B_{y'}k_{x'})z' \,, \tag{2.31}$$

where e is the electron charge, m^* is the effective electron mass, $B_{x'}$ and $B_{y'}$ are the in-plane components of the magnetic field, and z' is the coordinate operator. Up to date, several diamagnetic mechanisms of the MGPGE current formation based on the $B_l k_m$-terms have been proposed. One of them originates from $B_l k_m$-corrections in the hot electron scattering probability leading to current formation [61]. Another example is the diamagnetic shift of the subbands $\delta\varepsilon_\nu \propto B_l k_m$ [53] while the current is determined by the relative shift of the two participating subbands which is nonzero in heterostructures and asymmetrical QWs [62]. Regarding paramagnetic mechanisms of the MGPGE, where the magnetic field $\boldsymbol{B}$ acts on the spin of electrons $\boldsymbol{\sigma}$, one should mention the magnetic field induced conversion of pure spin currents into electric current due to the introduction of an equilibrium spin polarisation in the system by means of the Zeeman effect. In the following elaboration, first the diamagnetic mechanism of the MGPGE current generation due to the diamagnetic band shift and then the paramagnetic mechanism due to the Zeeman conversion of pure spin currents are discussed.

2.4.1 Diamagnetic band shift induced photocurrent

Magnetic field induced shift of the energy dispersions in the $\boldsymbol{k}$-space was investigated theoretically [63, 64] and observed experimentally for direct interband optical transitions [65, 66]. Originating from orbital effects and excluding any relation to the relativistic spin-orbit coupling, the asymmetry of the energy spectrum, $\varepsilon(\boldsymbol{k}, \boldsymbol{B}) \neq \varepsilon(-\boldsymbol{k}, \boldsymbol{B})$, was shown to be large and the diamagnetic shift mechanism proven to be efficient. Regarding MGPGE investigations under intersubband absorption of light in the chapter 5), it is reasonable to discuss the mechanism of the current formation based on the diamagnetic shift of size-quantised subbands.

An application of an in-plane magnetic field to an asymmetric two-dimensional electron gas (2DEG) induces in each size-quantised subband a spin-independent diamagnetic shift of the electron spectrum in $\boldsymbol{k}$-space. The corresponding corrections to the electron energies are determined by the diagonal matrix elements of the Hamiltonian (2.31) and have the form [53]

$$\delta\varepsilon_\nu = \frac{\hbar e}{m^* c}(B_{x'}k_{y'} - B_{y'}k_{x'})z'_{\nu\nu} \,, \tag{2.32}$$

where ν is the subband index, $z'_{\nu\nu} = \int \varphi_\nu^2(z')z'dz'$ is the coordinate matrix element and φ_ν is the function of size quantisation in the subband ν in zero magnetic field. This situation is sketched in Fig. 2.5 for e_1 and e_2 subbands. Although in QWs the spin degeneracy is removed even in the absence of an external magnetic field, in the following description, both the zero-field spin-orbit splitting and the Zeeman spin splitting are neglected. The value of the diamagnetic shift depends on $z'_{\nu\nu}$ and is generally different for e_1 and e_2 subbands. Due to the relative shift of the two subbands $\Delta k_{x'} \propto B_{y'}$, intersubband optical transitions induced by the monochromatic radiation of the photon

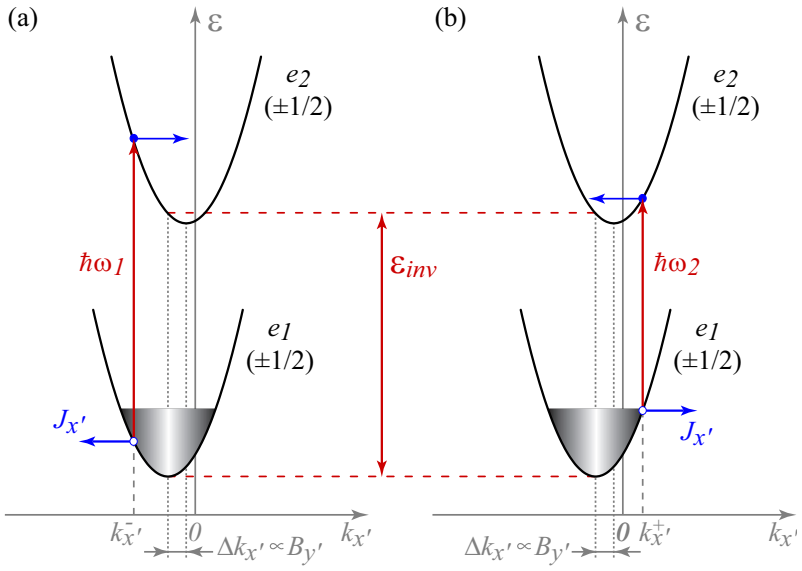

Figure 2.5: Mechanism of MGPGE current at intersubband resonance induced by asymmetric optical excitation due to diamagnetic shift of subbands in the $\boldsymbol{k}$-space.

energy $\hbar\omega_1$ occur only at a fixed wave vector $k_{x'}^-$ where the energy of the incident light matches the transition energy as it is indicated by the red vertical arrow in Fig. 2.5(a). As a result, optical transitions generate an imbalance of momentum distribution in both subbands yielding an electric current. However, a non-equilibrium distribution of carriers in the upper subband rapidly relaxes due to the very effective relaxation channel of *LO*-phonon emission. Thus, the contribution of the e_2 subband to the electric current vanishes and the electron flow is determined by the momentum distribution of carriers in the lowest subband resulting in a negative current $J_{x'}$. As directly follows from this model picture, the variation of the incident light frequency causes the inversion of the current direction at the photon energy $\hbar\omega = \varepsilon_{inv}$ corresponding to the optical transitions at the minimum of e_1. Indeed, at small photon energies, $\hbar\omega_2 < \varepsilon_{inv}$, excitation occurs at $k_{x'}^+$ shifted to the right from the e_1 minimum resulting in a positive current $J_{x'}$ as shown in Fig. 2.5(b). Calculations show that, for the case of optical transitions between the subbands e_1 and e_2 and the magnetic field aligned along y', the diamagnetic band shift induced photocurrent has the form [62]

$$j_{x'} = (z'_{11} - z'_{22})\frac{e^2 B_{y'}}{m^* c}\left[\tau_p^{(2)}\,\eta(\hbar\omega) + (\tau_p^{(1)} - \tau_p^{(2)})\,\bar{\varepsilon}\,\frac{d\,\eta(\hbar\omega)}{d\,\hbar\omega}\right]\frac{I}{\varepsilon_{21}}\,, \tag{2.33}$$

where $\tau_p^{(1)}$ and $\tau_p^{(2)}$ are the momentum scattering times in the first and second subbands, respectively, $\eta(\hbar\omega)$ is the QW absorbance which is calculated neglecting $\boldsymbol{k}$-linear terms but taking into account the inhomogeneous spectral broadening of the intersubband resonance, ε_{21} is the energy separation between the subbands e_1 and e_2, and $\bar{\varepsilon}$ is the *average* electron kinetic energy. The latter equals to $k_B T$ and $\varepsilon_F/2$ for a non-degenerate and degenerate 2DEG, respectively, whereas T is the temperature and ε_F the Fermi energy. In accordance to general symmetry arguments, the MGPGE current given by Eq. (2.33) is related to SIA of the QW and vanishes in symmetric structures where $z'_{11} = z'_{22}$. If the relaxation time of carriers in the excited subband is much shorter than that in

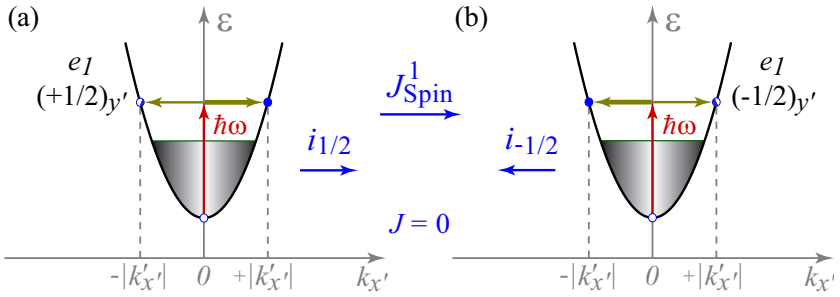

Figure 2.6: Mechanism of the pure spin current formation due to the spin-dependent asymmetry of the photoexcitation.

the ground subband, $\tau_p^{(2)} \ll \tau_p^{(1)}$, than the current contribution due to the diamagnetic shift of the electron subbands is proportional to the spectral derivative of the QW absorbance. This is similar to the spectral behaviour of the circular photogalvanic effect caused by intersubband transitions.

2.4.2 Magnetic field induced pure spin current conversion

Another mechanism of the MGPGE is based on the magnetic field conversion of pure spin currents and can be considered in two stages. The first stage is the zero-bias spin separation which has been considered theoretically in [67] for interband as well as inter- and intrasubband optical transitions. The experimental observation of the MGPGE under intrasubband absorption of the terahertz radiation in GaAs- and InAs-based QWs and heterostructures has been shown to stem from the zero-bias spin currents and, in the second stage, their subsequent conversion in an electric current applying magnetic field [20, 68]. This spin-dependent mechanism has been verified to cause the MGPGE current in diluted magnetic semiconductor (DMS) structures [69] by means of g-factor control.

1st Stage: Pure spin currents generation

Pure spin currents can be considered as fluxes of magnetisation without charge current and result in a spatial spin separation. In contrast to the spin Hall effect, in structures with suitable symmetry the spin separation can be achieved even at zero bias either due to the spin-dependent asymmetry of the photoexcitation or/and due to the spin-dependent asymmetry of the hot electron relaxation processes.

The first mechanism of the spin separation is related to the asymmetry of the photoexcitation and is shown in Fig. 2.6 for spin-up ($\sigma_{y'} = +1/2$) and spin-down ($\sigma_{y'} = -1/2$) subbands separately. An illumination in the terahertz range results for the typical QWs like InAs and GaAs in an absorption of Drude-type where an incident photon can be absorbed by an electron only if a third particle like a phonon or an impurity attends the process in order to satisfy the energy and momentum conservation laws. In gyrotropic media, however, the electron scattering on a third particle becomes asymmetrical due to an additional term in the scattering matrix element proportional to components of $[\boldsymbol{\sigma} \times (\boldsymbol{k} + \boldsymbol{k}')]$, where $\boldsymbol{\sigma}$ is the vector composed of Pauli matrices, and

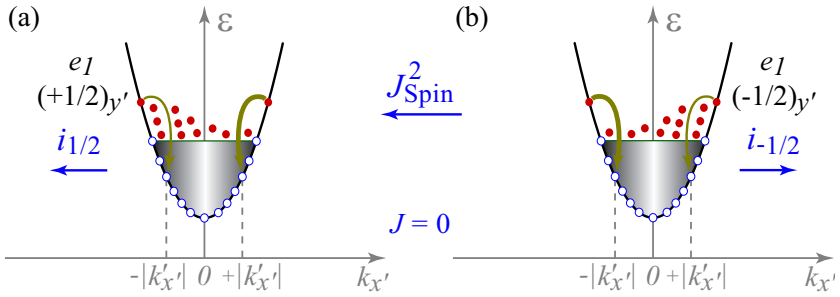

Figure 2.7: Mechanism of the pure spin current formation due to the spin-dependent asymmetry of the hot electron relaxation.

$\boldsymbol{k}$ and $\boldsymbol{k}'$ are the electron wave vectors of the initial and scattered state, respectively. Thus, for the spin-up subband the scattering to the positive $k'_{x'}$ occurs with higher probability than to negative $k'_{x'}$ as it is demonstrated by horizontal arrows of different thickness in the Fig. 2.6(a). For the sake of simplicity, it has been assumed that $k_{x'} = 0$, even though the argument holds for any $k_{x'}$. The asymmetry of electron scattering results in the non-equilibrium non-uniform distribution of the spin-up electrons in the $\boldsymbol{k}$-space. For the spin-down subband the whole picture mirrors in respect to the $k_{x'} = 0$ axis as sketched in the Fig 2.6(b). The asymmetric relaxation of the hot electrons exhibits the second mechanism of the spin separation and is shown in the Fig. 2.7. It should be pointed out that whereas the first mechanism is sensitive to the degree of the linear polarisation of the light, the second one is polarisation-independent [20]. In the framework of either mechanism, opposite sign spin currents $\boldsymbol{i}_{\pm 1/2}$ of an equal magnitude drift in opposite directions, $\boldsymbol{i}_{+1/2} = -\boldsymbol{i}_{-1/2}$, leading to spin separation without any charge flow. The *total* spin currents for the first ($\boldsymbol{J}^1_{\mathrm{Spin}}$) and the second ($\boldsymbol{J}^2_{\mathrm{Spin}}$) mechanism are given then by

$$\boldsymbol{J}^1_{\mathrm{Spin}} = (1/2)\left[\boldsymbol{i}^1_{+1/2} - \boldsymbol{i}^1_{-1/2}\right], \qquad \boldsymbol{J}^2_{\mathrm{Spin}} = (1/2)\left[\boldsymbol{i}^2_{+1/2} - \boldsymbol{i}^2_{-1/2}\right]. \tag{2.34}$$

Since total spin currents in (2.34) for both mechanisms have opposite signs, in a particular case for a specific radiation polarisation state, these contributions may compensate each other vanishing the total spin current $\boldsymbol{J}_{\mathrm{Spin}} = \boldsymbol{J}^1_{\mathrm{Spin}} + \boldsymbol{J}^2_{\mathrm{Spin}}$. In the general case, however, the spin separation is nonzero and can be visualised. For instance, the method of magneto-optical Kerr rotation is one of the experimental techniques which has been successfully used to demonstrate the spatial spin separation due to spin Hall effect [70]. However, a much simple method is to introduce an average spin in the system by means of an externally applied magnetic field. The resultant conversion of pure spin currents in an electric current represents the second stage of the spin-dependent mechanism.

2nd stage: Current conversion by magnetic field

An application of an external magnetic field breaks the time inversion symmetry and induces a non-zero equilibrium spin $\boldsymbol{S}^{(0)}$. Due to the spin polarisation of the system, the pure spin current $\boldsymbol{J}_{Spin}$ is converted to the net electric current $\boldsymbol{j}$ as [20]

$$\boldsymbol{j}^{MGPGE} = e(\boldsymbol{i}_{+1/2} + \boldsymbol{i}_{-1/2}) = 4eS^{(0)}\boldsymbol{J}_{Spin}\,. \tag{2.35}$$

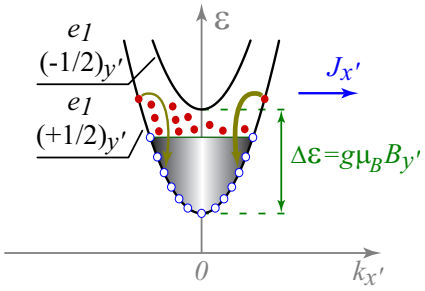

Figure 2.8: Model of MGPGE current based on the magnetic-field-induced conversion of pure spin currents due to the spin-dependent asymmetry of the hot electron relaxation into electric current. This polarisation-independent mechanism corresponds to the coefficient S_1 in the phenomenological equation set (2.29).

Here e is the electron charge and $S^{(0)} = (1/2)(n_{+1/2} - n_{+1/2})/(n_{+1/2} + n_{+1/2})$ is the average spin magnitude which depends on the different populations $n_{\pm 1/2}$ of spin-up and spin-down sublevels. In the presence of a magnetic field $\boldsymbol{B}$ the populations $n_{\pm 1/2}$ become unequal in terms of the Boltzmann distribution as a result of the Zeeman effect. The magnetic field generated equilibrium spin polarisation $\boldsymbol{S^{(0)}}$ can be written as

$$\boldsymbol{S^{(0)}} = \frac{g\mu_B \boldsymbol{B}}{4\varepsilon}\,, \tag{2.36}$$

where g is the effective Landé factor, μ_B is the Bohr magneton and ε is the characteristic electron energy conditioned by either state of the two-dimensional electron gas

$$\varepsilon = \begin{cases} \text{Fermi energy} \quad \varepsilon_F, & \text{degenerate gas} \\ \text{thermal energy} \quad k_B T, & \text{non-degenerate gas} \end{cases} \tag{2.37}$$

Figure 2.8 demonstrates the mechanism of the current conversion by an external magnetic field whereas, in particular, the spin currents originate from the asymmetric relaxation of the hot electrons ($\boldsymbol{J}^2_{\text{Spin}}$). Here, the magnetic field is aligned along y' generating the photocurrent in x' direction. This current $j_{x'}$ corresponds to the coefficient S_1 in the equation set (2.29) and is polarisation-independent. Its magnitude can be estimated as [62]

$$j_{x'} \propto e\tau_p^{(1)} S^{(0)} \frac{\xi}{\hbar} I\eta(\omega)\,, \tag{2.38}$$

where ξ is a parameter standing for the ratio of spin-dependent to spin-independent parts of the electron-phonon interaction. As one can see from the Eq. (2.38), the MGPGE current $j_{x'}$ is proportional to the frequency-dependent absorbance $\eta(\omega)$ and decays with the momentum relaxation time in the ground subband $\tau_p^{(1)}$.

Summarizing the discussion above, it has been shown that the MGPGE current may be of different microscopic nature stemming from both diamagnetic as well as paramagnetic processes. In particular, photocurrents originating from the diamagnetic band shift and magnetic field induced pure spin current conversion have been elaborated. From the basic point of view, their separation

appears to be of a fundamental interest as it allows to conclude on the elementary spin and orbital processes in every particular structure. From the Eq. (2.36) it is obvious that the paramagnetic mechanism of the MGPGE should be sensitive to any controlled variation of the parameters determining the equilibrium spin polarisation $\boldsymbol{S}^{(\mathbf{0})}$. Recently, in various sets of materials a distinctive separation of the paramagnetic and diamagnetic mechanisms has been performed. For instance, the experimental observation of the photocurrent sign inversions by the temperature controlled g-factor in the DMS structures [69] has verified the spin-related origin of the MGPGE current. Besides controlling the spin polarisation, experimental studies of current spectral and temperature dependences can give an additional information on the microscopical origin of the observed magneto-induced photogalvanic effects. Similar to the helicity-dependent CPGE and SGE, the MGPGE photocurrents allow to study the spin and orbital phenomena as well. One of the advantages of the latter method, however, is the MGPGE sensitivity even to the unpolarised light, the fact which may simplify the experimental setup.

Chapter 3

Experimental setup

All photogalvanic phenomena reported in this work are linked to the gyrotropic feature of the media. This can be achieved intrinsically, for instance, introducing low-dimensional materials such as QW structures. In the beginning, two sample sets, GaAs- and HgTe-based QWs, are presented and explicitly analysed in respect on their symmetry properties and peculiarities of the band structure. Generally, optical excitation of QWs can lead to galvanic effects due to interband, inter- and intrasubband absorption of light. Depending on the requested photon energy range, an appropriate excitation system is required. In this work, different gas laser systems such as CO_2-, NH_3- and CH_4F-lasers for the generation of radiation in the mid-infrared and terahertz spectral ranges have been applied. Besides the possibility of the wavelength selection, in all the experiments an additional optical setup has been used. An application of attenuators, polarisers and various adjustment geometries allowed variation of intensity, polarisation state as well as incidence angle of the laser beam. For investigations of magneto-gyrotropic effects in the range from room down to liquid helium temperatures different cryomagnetic systems have been used. All photogenerated currents have been evaluated in a specific electric setup which is reviewed at the end of this chapter.

3.1 Samples

Investigations of photo-induced currents have been performed on MBE[1]-grown single and multiple QW structures of n-type belonging to various gyrotropic symmetry classes. Two different zinc-blende semiconductor arrays have been grown up on differently aligned wafers. Their initial orientation determines the confinement axis of the 2DEG in the quantum well. The first set of the QW samples is based on GaAs and the second one on the narrow bandgap HgTe material. An exciting feature of HgTe-based QWs is the variation ability of the ground conduction band type in dependence on the QW width and temperature.

3.1.1 GaAs QWs

Bulk GaAs is a III-V direct bandgap zinc-blende-based semiconductor (see Fig. 3.1(a)) and belongs to the T_d point group. Preparing a QW structure, it is usually sandwiched with $Ga_xAl_{1-x}As$

[1] MBE: Molecular Beam Epitaxy.

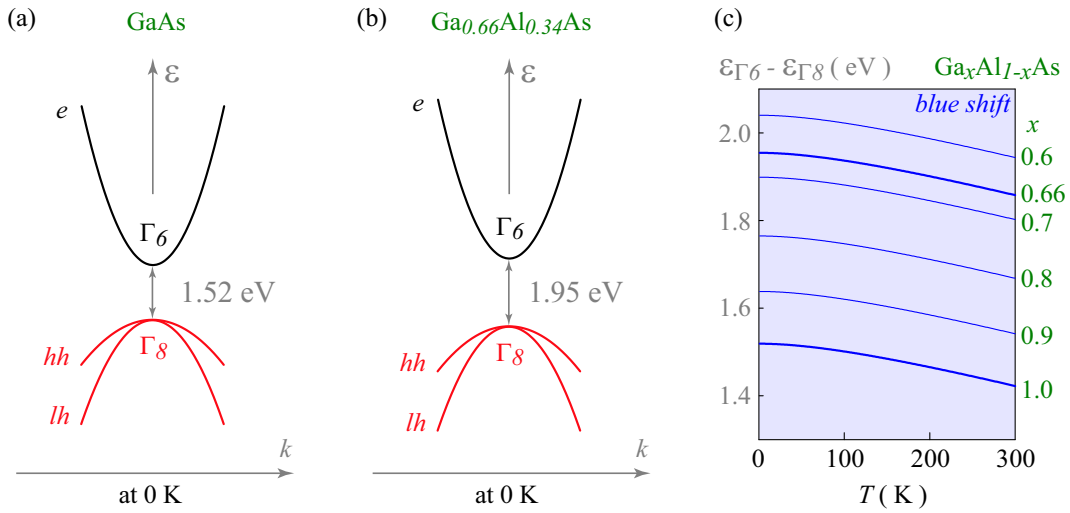

Figure 3.1: Direct bandgap of (a) GaAs and (b) $Ga_{0.66}Al_{0.34}As$ bulk semiconductors as well as (c) temperature dependence of the fundamental gap $\varepsilon_{\Gamma 6} - \varepsilon_{\Gamma 8}$ in bulk tertiary $Ga_xAl_{1-x}As$ semiconductors with direct bandgap at Γ-point [71].

which is for $x > 0.6$ a direct semiconductor as well (see Fig. 3.1(b)) and builds up the barrier. All GaAs/$Ga_xAl_{1-x}As$ structures have been doped with silicon. Below critical concentrations, the dopant atoms occupy the gallium position providing an additional electron to the system. In all QW structures such n-type doping has been displaced from the QW edge. In spite of the fact that the modulation doping lowers the density of 2DEG in comparison to the electron densities of structures doped inside the well, such technique allows, however, to increase the carrier mobility due to the reduced scattering probability of 2DEG on the ionised and neutral impurities. An example of MBE-grown (110)-oriented multilayer array and the correspondent evolution of the conduction band edge forming multiple QWs is shown in Fig. 3.2. The characteristic data of all experimentally studied GaAs/GaAlAs QW structures are summarised in the Tab. 3.1. The typical carrier mobilities of the

	QW structure	Growth axis	QW nm	Spacer 1 nm	Spacer 2 nm	QWs	Density/QW cm^{-2}
#1	GaAs/$Ga_xAl_{1-x}As$ (x=0.66)	(110)	8.2	5	25	100	$7 \cdot 10^{11}$
#2			8.2	15	15		
#3	GaAs/$Ga_xAl_{1-x}As$ (x=0.66)	(001)	7.6	15	15	30	$3 \cdot 10^{11}$
#4			8.2	15	15		
#5			8.8	15	15		

Table 3.1: GaAs-based multiple QW structures with characteristic data.

2DEG are in the range of several hundred thousands cm^2/Vs. The QW width in all the samples has been intended to be about 8 nm in order that the mid-infrared radiation of the CO_2-laser can match the separation energy between the first and second size-quantised subbands exciting resonant intersubband transitions. The generated photocurrents in the 2DEG have been measured along specific sample directions as a voltage drop in a closed circuit. For this purpose, pairs of

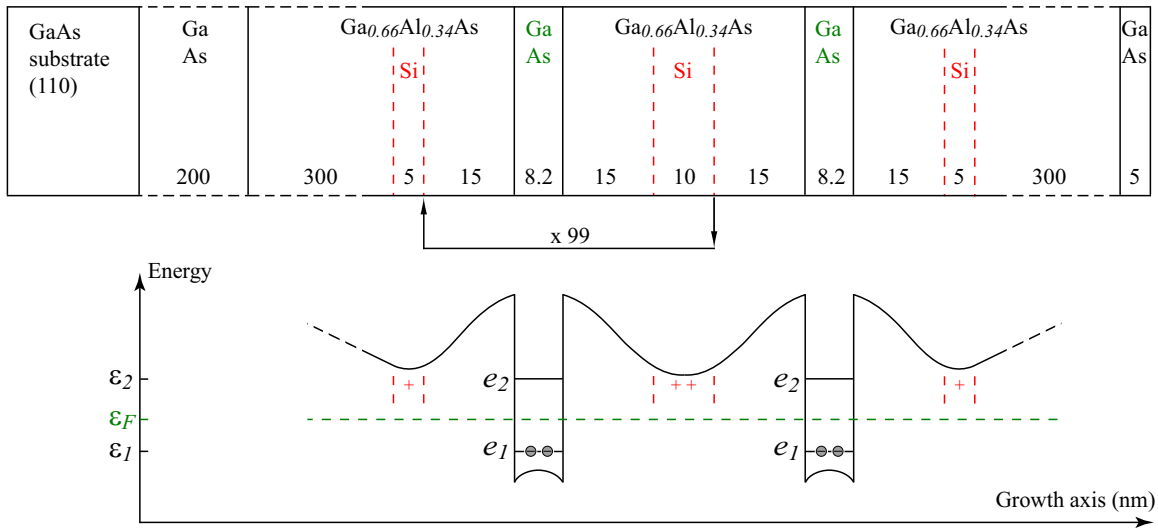

Figure 3.2: (a) MBE-grown (110)-oriented multilayer array and (b) the correspondent evolution of the conduction band edge for the GaAs-based QW structure #2 with $L_W = 8.2$ nm.

ohmic contacts have been placed along crystallographic axes $[1\bar{1}0]$, $[00\bar{1}]$ for (110)-oriented and $[1\bar{1}0]$, [110] for (001)-oriented structures while indium atoms have been thermically diffused in the multilayer array at sample edges.

Sample symmetry

Generally speaking, observation ability of photocurrents in a particular structure is governed by the point group symmetry of the structure itself. Therefore, clarification of the relevant symmetry classes for the nanomaterials under investigation appears to be of basic importance. Regarding GaAs-based QWs from the Tab. 3.1, two sample groups can be distinguished.

The first group of samples is grown along [110]-axis. Basically, (110)-grown symmetrical QWs belong to C_{2v} point group. However, any structure inversion asymmetry such as lattice stress or asymmetry of the doping position (see Sec. 2.1.1) destroys the mirror reflection symmetry of the QW downgrading the symmetry class to the C_s point group. As it can be seen from the Tab. 3.1, the sample #1 possesses asymmetric band edge profile due to the asymmetric modulation doping and belongs, therefore, to the C_s point group. Although the geometrically set profile of the sample #2 is symmetrical, this structure should be accounted, however, to the C_s symmetry class as well. This fact can be understood as following. In the MBE procedure of the sample growth, the sample surface is shelled by silicon atoms at equal spacings from the QW edges (see Fig. 3.2). However, the adsorption peak position of the silicon atoms shifts in the growth direction of the hot structure[2], the so-called segregation, and the real modulation profile differs from the geometrically set doping position. The resultant asymmetry downgrades the symmetry class from C_{2v} to C_s due to the SIA

[2](110)-oriented structures have been grown in the temperature range between 480°C and 500°C. Although the dopants diffusion was shown to be strongly suppressed [59], in the sample #2 with narrow spacer about 15 nm even a small shift modifies the symmetry affiliation.

	$\varepsilon_{\Gamma6-\Gamma8}(0)$ (eV)	α (10^{-4} eV/K)	β (K)
GaAs	1.519	−5.4	204
$Ga_{0.66}Al_{0.34}As$	1.954		

Table 3.2: Semi-empirical Varshni coefficients for bulk GaAs and $Ga_{0.66}Al_{0.34}As$ structures [71].

terms.

The second group of samples is oriented along the cubic [001]-axis. (001)-grown symmetric QWs belong to the D_{2d} point group. Introduction of any additional asymmetry, however, downgrades the symmetry class of the nanomaterial to the C_{2v} point group. Similar to the consideration above for the (110)-grown structures, the segregation of the symmetrically placed dopant atoms in (001)-oriented materials[3] allows to relate the samples #3, #4 and #5 to the C_{2v} symmetry class.

Band structure

Illumination of GaAs-based QW structures with the infrared radiation can lead to interband, inter- and intrasubband absorption of light. While the latter case of absorption predominates in a wide range of low photon frequencies (Drude-like absorption), the inter(sub)band absorption of radiation is a resonant process and depends on the relative spectral position of valence and conduction subbands in a particular structure.

Starting from bulk materials, the bandgap energy of GaAs increases while the temperature decreases leading to spectral 'blue shift' of about 100 meV as shown in Fig. 3.1(c) for differently composed $Ga_xAl_{1-x}As$ alloys with a direct bandgap at Γ-point [71]. The shift of the peak position energy (PPE) with temperature can be described by semi-empirical Varshni equation [72]

$$\varepsilon_{\Gamma6-\Gamma8}(T) = \varepsilon_{\Gamma6-\Gamma8}(0) + \frac{\alpha T^2}{T+\beta}, \tag{3.1}$$

where $\varepsilon_{\Gamma6-\Gamma8}(0)$ is the energy gap value between Γ_6 and Γ_8 band points at the theoretical temperature of 0 K, and α and β are material specific constants. The values of these parameters for bulk GaAs and $Ga_{0.66}Al_{0.34}As$, which form the well and barrier of QW structures, are given in Tab. 3.2. From the physical point of view, temperature-induced bandgap offset in a bulk material is believed to arise from following two mechanisms. Besides the thermal dilatation of the lattice [73], the major contribution to the gap variation comes from the shift in relative position of the conduction and valence bands due to a temperature-dependent electron-lattice interaction [72]. Indeed, the increasing temperature gives raise to the amplitude of atomic vibrations. Subsequently, an increased interatomic spacing decreases the potential seen by the electrons in the material, which in turn reduces the energy of the bandgap. This bandgap offset leads to the PPE red (blue) shift with the temperature increase (decrease).

[3]The growth temperature of (001)-oriented structures is about 630°C. This results in a homogeneous distribution of Ga and Al over each monolayer and decreases the number of defects. On the other hand, the temperature raise enhances the segregation of silicon atoms in the growth direction.

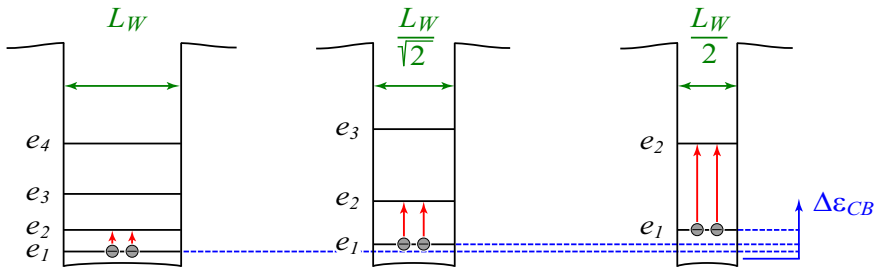

Figure 3.3: Effect of the quantum confinement on the band structure in QWs. The subsequent decrease of the well width by factor $\sqrt{2}$ doubles the intersubband separation energy.

Discussing resonant absorption of light in GaAs QWs, one should point out the spectral shift of subbands by variation of quantum well width and temperature. In QWs of the type-I like GaAs/GaAlAs QW structures, the decrease of the well width shifts the PPE position of inter(sub)band resonance to the higher energy values (blue shift) due to the effect of the size quantisation (see Fig. 3.3). In the case of intersubband transitions between the subband n and subband $n+1$, the intersubband PPE $\varepsilon_{n+1,n}$ is proportional to the inverse square of the well width L_W [74]

$$\varepsilon_{n+1,n} \propto \frac{2n+1}{L_W^2}. \tag{3.2}$$

As it is shown in Fig. 3.3, subsequent decrease of the QW width by factor $\sqrt{2}$ increases in each step the intersubband separation by factor 2. For interband transitions the effective bandgap $\varepsilon_{\Gamma 6-\Gamma 8}$ of bulk material is enhanced by the confinement-induced blue shift in the conduction band $\Delta\varepsilon_{\mathrm{CB}} = \varepsilon_{1,0}$[4] (see Fig. 3.3).

In a similar manner like the decrease of the QW width, the temperature fall causes the blue PPE shift of inter(sub)band transitions as well. However, the physical origin of the temperature-induced offset in QWs differs from that in bulk GaAs discussed above. It has been demonstrated that the blue shift of the intersubband PPE can be described correctly if depolarisation and exciton-like shifts as well as many-body effects such as exchange and direct Coulomb interactions are accounted [75]. In the modulation doped GaAs-based QW structures the intersubband PPE blue shift was shown to be about 3 meV. This value should be kept in mind while spectral measurements of the magneto-gyrotropic photocurrents due to the intersubband absorption of radiation at room and liquid helium temperatures are considered.

3.1.2 HgTe QWs

Bulk $Hg_xCd_{1-x}Te$ is a II-VI direct bandgap semiconductor alloy with a possibility of bandgap energy variation in a wide range of about 2 eV (see Fig. 3.4(a)) [76]. While the CdTe features a bandgap similar to the GaAs, the increase of Hg fraction lowers drastically the bandgap energy. Indeed, at $x \approx 0.85$ the band points Γ_8 and Γ_6 become already degenerated. Furthermore, bulk

[4] In the valence band, the qualitative picture is the same but mirrored enhancing the effective bandgap by valence-band-correction $\Delta\varepsilon_{\mathrm{VB}}$.

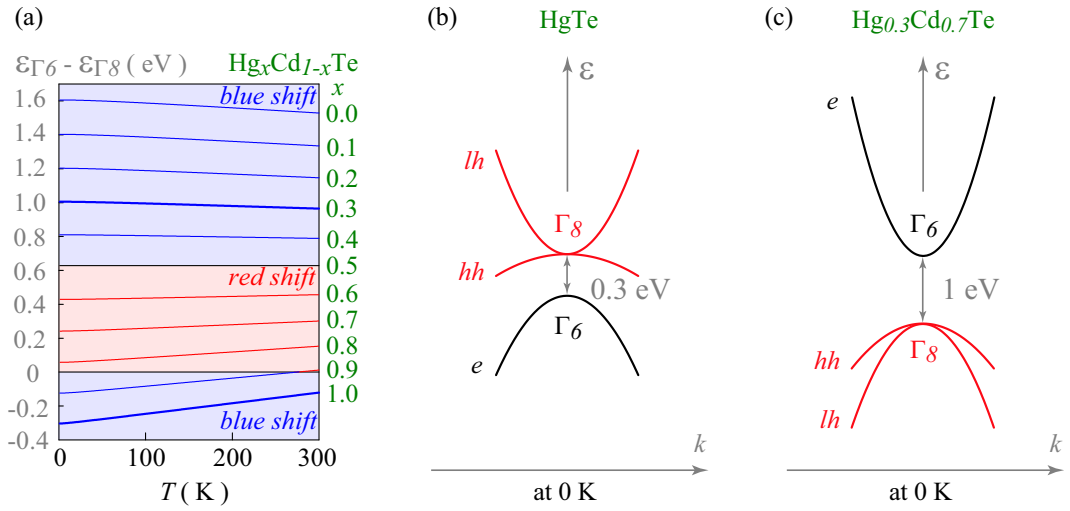

Figure 3.4: (a) Temperature variation of the fundamental gap $\varepsilon_{\Gamma 6} - \varepsilon_{\Gamma 8}$ of bulk tertiary $Hg_xCd_{1-x}Te$ for different x values as well as direct bandgap of (b) HgTe and (b) $Hg_{0.3}Cd_{0.7}Te$ bulk semiconductors.

HgTe exhibits an inverted Γ_8-Γ_6 band ordering as shown in Fig. 3.4(b). For the experimental study of HgTe-based QWs the HgTe has been combined with $Hg_{0.3}Cd_{0.7}Te$ (see Fig. 3.4(c)) forming a high barrier. In order to form the 2DEG in the QW, generally, the desired n-type doping of a II-VI semiconductor can be achieved either injecting elements of the 3rd group in the metal sublattice, or settling elements of the halogen group on the nonmetal site in the host crystal. Preparing QW samples, two different dopant elements have been employed. While the set of nanostructures oriented along the [001]-axis has been doped with iodine, the (013)-grown QW structure has been endowed with asymmetrically placed layers of indium. All investigated HgTe samples are summarised in the Tab. 3.3 possessing a single QW only. After the MBE growth procedure, (001)-oriented samples have been cleaved along the crystallographic plane (110) and for better performance a clover profile has been etched on the sample top as it is shown in the Fig. 3.5. Pairs of ohmic contacts have been placed along the cubic axes by thermal diffusion of indium on cloverleaf ends. Regarding the (013)-oriented structure, the natural cleavage will fashion a rhombus form with directions along $[3\bar{3}1]$ and $[33\bar{1}]$ as well as $[\bar{3}\bar{3}1]$ and $[\bar{3}3\bar{1}]$. In order to obtain a rectangular form, the sample has

	QW structure	Growth axis	QW nm	Spacer 1 nm	Spacer 2 nm	Density 10^{11} cm^{-2}	Mobility 10^4 cm^2/Vs
#6	$HgTe/Hg_xCd_{1-x}Te$ (x=0.3 I-doped)	(001)	5	10	10	5.6	5.6
#7			8	10	10	6.1	2.1
#8			12	10	10	6.2	17.7
#9			22	20	54†	10	17.2
#10	$HgTe/Hg_xCd_{1-x}Te$ (x=0.27 In-doped)	(013)	21	5	8	2.7	8.1

Table 3.3: HgTe-based single QW structures with characteristic data.

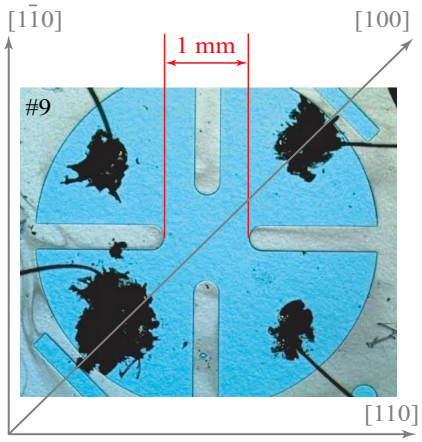

Figure 3.5: Clover profile etched on the HgTe-based QW structure #9 with two pairs of ohmic contacts along cubic axes.

been cut along two almost orthogonal directions. These are denoted using a triple-prime system as x''' and y''' building a right-handed coordinate system with the growth direction $z''' \parallel [013]$.

Sample symmetry

Before starting the experimental investigation of HgTe-based QWs, primarily, a proper determination of the sample symmetry is necessary. According to basic substrate orientation, two groups of samples can be distinguished.

The first group comprises four nanostructures oriented along the cubic [001]-axis. As it has been already noticed discussing the GaAs-based samples, (001)-grown symmetric zinc-blende-based QWs belong to the D_{2d} point group. Besides this fact, it has been demonstrated that the segregation of silicon atoms in a hot structure constitutes an asymmetric profile of the conduction band edge leading to appearance of structure inversion asymmetry and downgrading the symmetry class to the C_{2v} point group. Although the growth temperature of the HgCdTe barrier is cooled down to 180°C-190°C for better adsorption of Hg atoms, the iodine atoms being in general strongly agile diffuse along the confinement axis in the range from several up to ten nanometres as supposed from SIMS[5] measurements [77]. As a consequence, both symmetrically doped structures #6, #7 and #8 as well as the one-side-doped sample #9 with 22 nm well are in fact asymmetrical and should be accounted C_{2v} point group.

The structure #10 in the Tab. 3.3 is oriented along very unusual [013]-direction. Low-dimensional structures confined along this axis belong to the lowest possible symmetry C_1 possessing only the identity as a symmetry operation. Although the C_1 point group cannot be downgraded any more, the SIA caused by asymmetric doping position together with a strong diffusion of indium dopant atoms in the growth direction may, however, enhance effects allowed in this group.

[†]One side doped sample, the distance is given from QW edge to sample surface.
[5]SIMS: Secondary Ion Mass Spectrometry.

	$\varepsilon_{\Gamma6-\Gamma8}(0)$ (eV)	α (10^{-4} eV/K)	β (K)
HgTe	−0.303	6.3	11
$Hg_{0.3}Cd_{0.7}Te$	1.006	−1.6	58
$Hg_{0.27}Cd_{0.73}Te$	1.065	−1.8	60

Table 3.4: Semi-empirical Varshni coefficients for bulk HgTe, $Hg_{0.3}Cd_{0.7}Te$ and $Hg_{0.27}Cd_{0.73}Te$ structures [76].

Band structure

As a last point of sample analysis, peculiarities of the band structure of HgTe-based QWs should be reviewed. Indeed, the inverted band ordering of the HgTe forming the well causes a nontrivial situation different from that in GaAs-based samples.

Considering first bulk materials, the bandgap $\varepsilon_{\Gamma6-\Gamma8}$ of tertiary $Hg_xCd_{1-x}Te$ depends both on the Hg/Cd composition and temperature. Figure 3.4(a) demonstrates the temperature behaviour of the bandgap for fix compositions according to Laurenti formula [76]. As it can be seen from the figure, in cadmium dominated tertiary ($x < 0.5$) for a constant x, the energy distance between Γ_6 and Γ_8 increases with the temperature fall leading to the blue shift of the light absorption. However, in mercury surpassing regime ($x > 0.5$) the shrunken bandgap follows the temperature decrease performing the red shift. Increasing the Hg fraction at a fix temperature, the points Γ_6 and Γ_8 narrow each other until they cross at a definite inversion point $x_{\text{inv}}(T)$. For $x > x_{\text{inv}}$, the mutual trend of the bands continues and the band ordering becomes inverted. In this mode, the temperature decrease enlarges the energy distance between Γ_6 and Γ_8. For the bulk HgTe ($x = 1$) the passage from room down to liquid helium temperature results in a blue shift of about 180 meV. Tab. 3.4 summarises the Varshni coefficients for HgTe and $Hg_{0.3}Cd_{0.7}Te$ ($Hg_{0.27}Cd_{0.73}Te$) forming the well and barrier, respectively.

Discussing the band structure in a QW, similar conventions to that for GaAs-based structures can be applied, i.e., the influence of both confinement effect and temperature on the energy position of the size-quantised subbands. However, the inverted band ordering of the bulk HgTe material and a strong shift of the fundamental bandgap with temperature complicate the trivial scheme. A qualitative picture of the band structure is shown in Fig. 3.6 whereas the effective mass ratio m_h/m_e of heavy holes and electrons has been assumed to be around 6 [78]. Figure 3.6(a) demonstrates the case of quasi-bulk HgTe at 4 K where the energy distance between the lowest electron subband and the topmost hole-type subband is almost 0.3 eV. The stepwise decrease of the QW width by factor 2, figures 3.6(b) and (c), increases the separation between quantised subbands due to the Eq. (3.2) by factor 4 lifting drastically first electron subband from the well bottom. Below the inversion point $L_{\text{inv}} = 6.3$ nm [25], the lowest electron subband lies above the highest hole subband (Fig. 3.6(d)) and the band ordering becomes normal. This situation can be imagined as a quasi-bulk state of the barrier material $Hg_{0.3}Cd_{0.7}Te$ with a trivial band sequence. Moving from liquid helium to room temperature, the fundamental bandgap of the bulk HgTe scales down to 0.12 eV shifting the electron and hole subbands in the quasi-bulk material (Fig. 3.6(e)) against each other. It is obvious

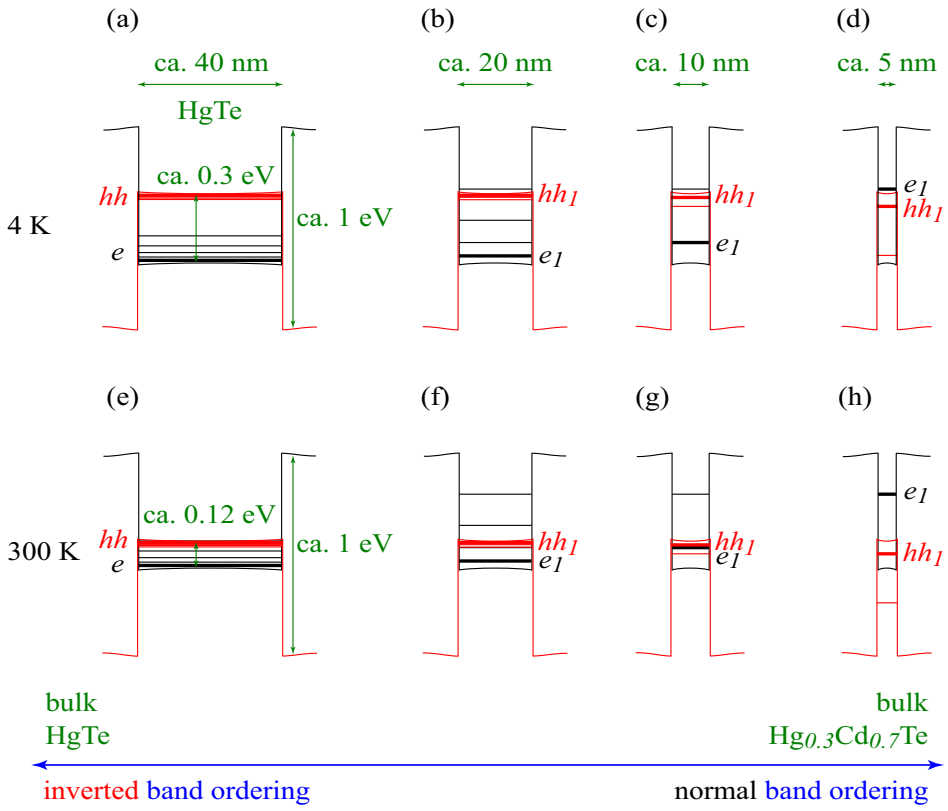

Figure 3.6: Qualitative picture of the band structure in wide and narrow HgTe/$Hg_{0.3}Cd_{0.7}Te$ QWs at liquid helium and room temperature.

that the effect of temperature increase acts in the same manner as the reduction of the well width. This leads, in particular, to an appearance of a definite well width region above $L_{\mathrm{inv}} = 6.3$ nm where simple temperature variation allows to switch between both phases. This is demonstrated by band structure calculations for QW with $L_W = 8$ nm at liquid helium and room temperatures which have been performed using the eight-band $\boldsymbol{k}\cdot\boldsymbol{p}$ model in envelope function approximation [79,80]. While at 4 K the topmost heavy-hole-like subband is energetically higher reclined than the lowest electron subband (Fig. 3.7(a)), at 300 K the band ordering becomes normal (Fig. 3.7(b)). In the qualitative consideration shown in Fig. 3.6, the shift of the size-quantised subbands with the temperature has been excluded. However, the calculations in Fig. 3.7 legitimate this neglection as the blue shifts of about 20 meV and 5 meV for electron- and heavy-hole-like subbands, respectively, have been determined which are by an order of magnitude weaker than that of the fundamental gap in a bulk material. Even though the situation around the HgTe-based QWs is complex, it is worth the effort since the narrow gap can be tuned in a wide range.

3.2 Laser systems

In the previous section, different QW structures have been considered. Depending on their band properties, optical excitation in the infrared range can lead to interband, inter- and intrasubband

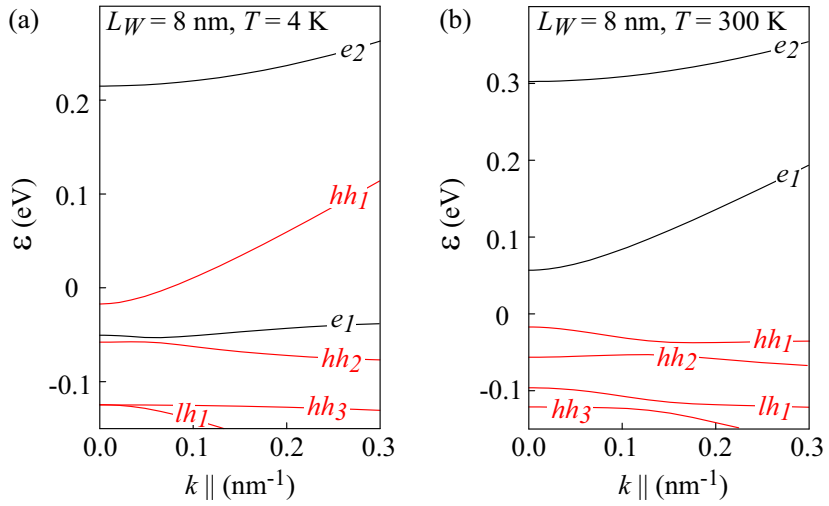

Figure 3.7: Calculated band structure for 8 nm wide HgTe quantum well at (a) $T = 4.2$ K and (b) $T = 300$ K.

light absorption. While for inter(sub)band resonance the radiation of the mid-infrared CO_2-laser, for inducing of intrasubband transitions the light of optically pumped terahertz lasers has been used.

For the purpose of the inter(sub)band excitation, radiation of CO_2 gas laser has been applied (for review see [81]). The spectral range originating from rotational-vibrational transitions of CO_2 molecule lies between 9.2 and 10.8 μm corresponding to photon energies between 115 and 135 meV. Since the laser oscillation occurs in general on transition with the largest gain, wavelength tuning away from the strongest line appears to be of interest as it allows to measure the photocurrent spectral function. For this sake, it is common to use a diffraction grating as one of the resonator mirrors. The angular setting of the grating allows to reflect the desired wavelength exactly back into the resonator. Depending on the required intensity, pulse frequency and duration, two laser systems have been utilised: transversally excited atmospheric pressure (TEA) lasers with short pulses in the range of about 100 ns and intensities up to hundred MW/cm^2 as well as a continuous-wave CO_2 laser with slow axial gas flow. The latter system has been converted in a quasi-pulse mode by an active Q-switching technique while a rotating mirror has been inserted inside the laser cavity. The average values of output pulse frequency, duration and peak intensities obtained are about 100 Hz, 300 ns and several kW/cm^2, respectively.

Studying various phenomena under intrasubband (Drude-like) absorption of light, low-dimensional structures have been irradiated with the light of terahertz molecular lasers. These have been pumped optically by TEA CO_2-laser pulses exciting rotational transitions of active medium gas molecules. Selecting the appropriate pumping line and cavity gas, here, NH_3 and CH_3F, the spectral range of the terahertz laser could be tuned from 90 μm to 496 μm. Single laser modes used in the experiments are summarised together with their relevant characteristic data in the Tab. 3.5. The temporal behaviour of the terahertz laser pulse is similar to that of the particular pumping line of the TEA CO_2-laser and is in the range of about 100 nanoseconds. Regarding the output beam,

λ	f	$\hbar\omega$	Intensity	Pulse energy	Pumping
μm	THz	meV	kW/cm^2	mJ	line
90	3.32	13.7	5000	4.8	9R(16)
148	2.03	8.4	4500	6.4	9P(36)
280	1.07	4.4	1000	2.0	10R(8)
496	0.61	2.5	10	0.02	9R(20)

Table 3.5: Single terahertz laser modes and their characteristic data [82].

either laser system emits a linearly polarised radiation.

3.3 Optical setup

Performing spectral investigations, a proper choice of the laser system appears to be sufficient. However, measurements of polarisation functions require an additional optical setup. Moreover, studying those photocurrents which behave linearly on the incident light intensity, sometimes it is necessary to attenuate the beam power. For this reason, stacks of CaF_2 and polymer plates made from teflon and pertinax have been inserted in the optical path for the CO_2-laser and terahertz radiation range, respectively [33].

Studying polarisation dependences, it is necessary to vary the polarisation state of the electromagnetic wave. The original linear polarisation of the laser emitted radiation could be either rotated on azimuthal angle α or transformed into elliptical (circular) polarisation state. In the mid-infrared range, elliptical polarisation has been obtained employing Fresnel rhombuses cut from ZnSe single crystals. Depending on the orientation of the rhombus to the electric field vector of the incident wave, the linearly polarised light performs two internal reflections in the crystal experiencing two phase shifts up to 45° at each time. The rotation of the rhombus on an angle $\varphi = (2n+1)\cdot(\pi/4)$ leads for $n = 0$ and even n to right-handed (σ^+) and for odd n to left-handed (σ^-) circular polarisation. The light helicity P_{circ} describing the degree of circular polarisation is connected with the angle φ over $P_{\mathrm{circ}} = \sin(2\varphi)$. Linear polarisation of mid-infrared light has been obtained from the circularly polarised light. For this reason, behind the Fresnel rhombus a pair of oppositely inclined Brewster windows have been installed transmitting only the desired linear polarisation and preventing the lateral shift of the beam. The rotation of the double-Brewster array on an angle α in the plane normal to the radiation propagation allowed to obtain any linear polarisation state.

Optical excitation in the terahertz range has been performed using linearly polarised light only. However, studying photocurrents as a function of the polarisation plane orientation, an azimuthal rotation of the wave electric field vector is required. In this spectral range, $\lambda/2$ birefringent wave plates made of crystal quartz have been applied. The physical principle is based on different propagation velocities of two electromagnetic wave components with the electric vector aligned along the optical (slow) and perpendicular (fast) axes of the plate. The phase shift occurs due to the outpacing of the quick wave by a half wavelength inside the plate. As a consequence, inclination

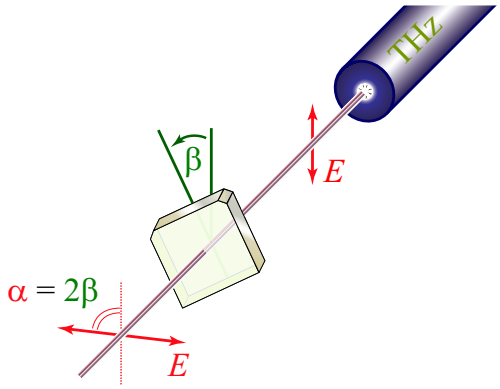

Figure 3.8: Function principle of $\lambda/2$-plate.

of the optical axis to the electric vector of the incident wave by an angle β leads to an azimuthal rotation of the emergent polarisation plane by an angle $\alpha = 2\beta$ as shown schematically in the Fig. 3.8.

3.4 Cryomagnetic systems

Optical excitation of samples with polarised light can lead to current generation. However, exploring magneto-gyrotropic photogalvanic effects, an application of external magnetic field is necessary. For this reason, different tunable magnet systems have been utilised. Moreover, studying photocurrent behaviour at low temperatures, a reliable technique of controlled sample cooling is required. Magneto-optical measurements at low and room temperatures are performed in various cryomagnetic configurations. For low magnetic fields, a continuous flow optical cryostat is installed in the variable gap of a dipole electromagnet generating fields up to 0.5 Tesla. For measurements at room temperatures the cryostat is removed from the setup allowing enhancement of the magnetic field strength by simple reduction of the magnet pole gap. Investigating photo-induced currents at high magnetic fields, superconducting magnet cryostat systems have been used permitting fields up to 7 Tesla. These are supplied with cylindrical vacuum and nitrogen jackets providing a permanent liquid helium pool for the magnet coils. The temperature in the sample chamber can be conditioned in a wide range from 4.2 up to 265 K. While cooling occurs by continuous flow of the liquid helium through the open inlet, the heating is generally achieved in the regime of the closed valve using Joule effect. Optical access to the chamber both along and perpendicular to the field allowed magneto-optical measurements in both in- and out-of-plane geometries.

3.5 Electric evaluation setup

Up to now, different initiating systems of the photocurrent generation have been discussed. Basic research, however, requires current evaluation in order to suggest on the fundamental processes under investigation. In general, photo-induced currents have been measured in a closed circuit as

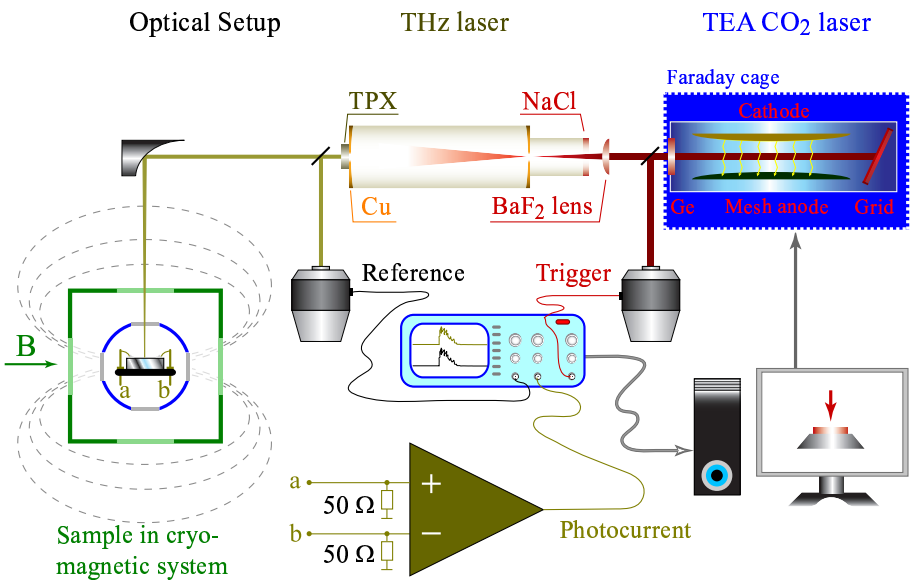

Figure 3.9: Experimental setup of photogalvanic measurements under terahertz excitation in an external magnetic field.

a voltage drop over 50 Ω load resistance by means of a storage digital oscilloscope. Although the electric evaluation of signals induced by pulsed and Q-switched laser systems are a bit different, the main concepts remain the same. In either case, the excitation and measuring system must be triggered. Experimental setup scheme shown in Fig. 3.9 describes a sample in a cryomagnetic system excited by radiation of optically pumped terahertz laser as well as the trigger and evaluation configuration. After desktop controlled discharge of a CO_2-laser, a short infrared pulse triggers the oscilloscope over Faraday cage outlet detector. Simultaneously, the latter stores at each time a set of temporal signal shapes originating from both reference photon drag detector and sample under terahertz laser pulsed excitation. While photocurrents in GaAs-based samples have been amplified, those in HgTe nanostructures have been measured simply as a voltage drop over 50 Ω resistance. In the last step, the oscilloscope has forwarded the stored information to the computer hard drive for the sake of further evaluation.

Chapter 4

Helicity-dependent photocurrents in (110)-grown GaAs QWs

Helicity-dependent photocurrents are gyrotropic effects which arise in low-symmetrical structures under homogeneous irradiation. Besides their importance for the fundamental research of carrier spin and orbital properties, such currents like circular photogalvanic effect (CPGE) and optically induced spin-galvanic-effect (SGE) have excelled as an investigation tool of spin relaxation times, spin splitting of the band structure and symmetry properties of the materials [32, 33]. A particular case of helicity-dependent effects are spin photocurrents, i.e., those photocurrents which involve the carrier spin degree of freedom. Experimental study of spin currents may provide an additional understanding about the carrier spin properties which are of essential relevance for the field of spintronics. Basically, these currents arise in low-symmetrical structures with spin-orbit interaction and are strongly controlled by the magnitude of the linear spin-orbit splitting. However, the same spin splitting is simultaneously the driving force of an efficient spin dephasing mechanism in terms of the D'yakonov-Perel'(DP) spin relaxation theory (see Sec. 2.2). Spin relaxation time determines the spin memory of the spintronics devices and, generally, should be sufficiently long for the processing of the information encoded as spin polarisation. Since the DP interaction depends on the directions of the electron momentum and spin in the host crystal, it should be possible to suppress this mechanism in QWs by an appropriate selection of the confinement axis. Recently, this 'switch-off' has been achieved in (110)-grown symmetrical GaAs-based QW structures where the spin relaxation time was shown to increase in the range of nanoseconds at room temperature [83, 84]. The suppression of the DP relaxation mechanism is sketched in Fig. 4.1. The precession of the out-of-plane spin $\boldsymbol{S}$ around the co-oriented effective magnetic field $\boldsymbol{B}^{\text{eff}}$ preserve the initial spin polarisation leading to substantially longer spin memory time which is determined by another relaxation mechanisms (for review see [18]). As a matter of fact, the experimental observation of the long spin dephasing times has attracted a great deal of attention to the spin-dependent phenomena in the (110)-oriented structures.

In the present chapter, observation and study of the helicity-dependent photocurrents in (110)-grown GaAs/GaAlAs QW structures under intersubband absorption of the mid-infrared radiation are presented. The investigated effects comprise the CPGE and the circular photon drag effect

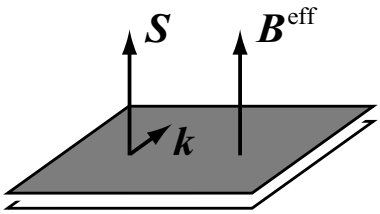

Figure 4.1: Precession of the spin polarisation $\boldsymbol{S}$ around the co-oriented effective magnetic field $\boldsymbol{B}^{\text{eff}}$ leads in collision-dominated regime via Eq. (2.15) to infinite spin relaxation time value ($\tau_s \approx \infty$).

(CPDE) predicted a long time ago [85,86] but so far not observed. The experimental data are well described by analytical expressions derived from the phenomenological theory and fit well to the microscopic picture of the CPGE (see 2.3.1). The developed microscopic model of the CPDE is related to the spin-dependent processes and bases on the optical spin orientation and the subsequent asymmetric spin-flip relaxation.

4.1 Experimental results and discussion

The experiments have been carried out at room temperature on asymmetrical (110)-grown GaAs/GaAlAs multiple QW structures. Two QW structures, #1 and #2, with the same QW width of 8.2 nm, but different doping profiles are investigated (see Tab. 3.1). The mid-infrared radiation of the Q-switched CO_2-laser in the range between 9.2 and 10.8 μm induces in both structures resonant intersubband transitions between the first and second size-quantised subbands. Illuminating the unbiased samples with the mid-infrared light under normal and oblique incidence, different polarisation-dependent as well as polarisation-independent current contributions have been observed [87]. However, in order to study the helicity-dependent photocurrents J^{circ}, in the following, the current responses to σ^+ and σ^- radiation are determined and the data evaluated after

$$J^{\text{circ}} = \left[J(\sigma^+) - J(\sigma^-)\right]/2. \tag{4.1}$$

Discussing the (110)-grown QW structures, it is convenient to use the double-prime coordinate system (2.19),

$$x'' \parallel [1\bar{1}0], \quad y'' \parallel [00\bar{1}], \quad z'' \parallel [110],$$

where x'' and y'' are oriented along crystallographic axes and z'' denotes the quantum confinement axis. Irradiating samples at normal incidence, a photocurrent proportional to the radiation helicity P_{circ} is detected. This helicity-dependent current has been observed with the contact pairs aligned along $x'' \parallel [1\bar{1}0]$ only which is in agreement with the phenomenological theory. In fact, the asymmetric (110)-oriented structures belong to media of C_s point group. In this symmetry, the circular photocurrent density $j_{x''}$ excited by light incident in the $x''z''$ plane is given by [33]

$$j_{x''} = \gamma_{x''z''} t_p t_s \frac{q_{z''}}{q} E_0^2 P_{\text{circ}}, \tag{4.2}$$

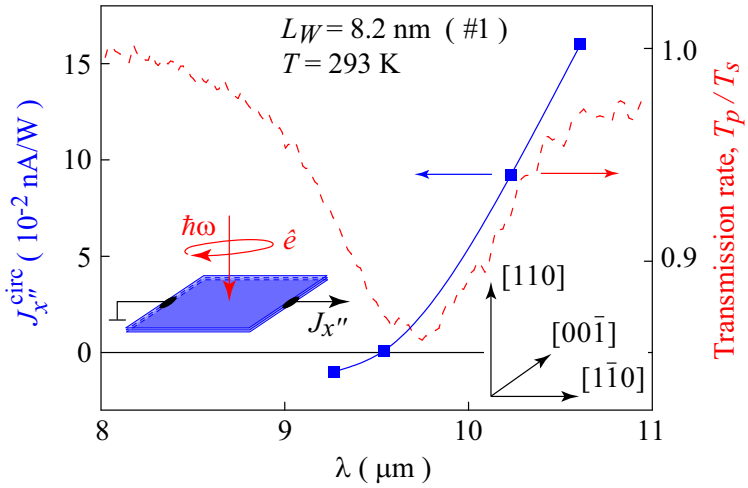

Figure 4.2: Spectrum of the helicity-dependent photocurrent $J_{x''}^{\mathrm{circ}}$ obtained in the sample #1 with $L_W = 8.2$ nm under normal incident mid-infrared excitation. The solid line is a guide for the eye. The inset sketches the experimental geometry. Spectral dependence of the optical transmission ratio T_p/T_s of p- and s-polarised radiation is shown by red dashed line.

where $\boldsymbol{\gamma}$ is the second-rank pseudotensor describing the sum of the circular photogalvanic effect (CPGE) and optically induced spin-galvanic effect (SGE), t_p and t_s are the transmission coefficients for the p and s components of the light electric field, $\boldsymbol{q}$ is the light wave vector inside the medium, E_0 is the electric field amplitude of the incident light and P_{circ} is the light helicity whereas $P_{\mathrm{circ}} = \pm 1$ for the $\sigma_\pm$ polarisation, respectively. The half difference of the currents for $P_{\mathrm{circ}} = \pm 1$ yields the helicity-dependent current density j_x^{circ}. The dependence of the photocurrent on the angle of incidence θ_0 is given by $q_{z''}/q = \cos\theta$ and Fresnel's formulas for t_p and t_s [88]

$$t_p t_s = \frac{4\cos^2\theta_0}{(\cos\theta_0 + n\cos\theta)\,(n\cos\theta_0 + \cos\theta)}, \tag{4.3}$$

where θ is the angle of refraction defined by $\sin\theta = \sin\theta_0/n$ and $n = 3.3$ is the infrared refractive index of the GaAs surface at room temperature.

An interesting question is the physical origin of the observed circular photocurrent $J_{x''}^{\mathrm{circ}}$. Since the second-rank pseudotensor $\boldsymbol{\gamma}$ characterises both helicity-dependent current contributions, i.e., the CPGE and the SGE, it is obvious that their separation by mere variation of parameters in the phenomenological Eq. (4.2) is not possible. In the case, if the spin-relaxation time exceeds the momentum relaxation time, time-resolved measurements could help to distinguish between them. However, a much easier method is to study the spectral dependence of the circular photocurrent. Whereas the CPGE behaves as a derivative of the intersubband absorption spectrum, the SGE is proportional to it. Measurements of the spectral behaviour of $J_{x''}^{\mathrm{circ}}$ in the mid-infrared range have revealed a spectral inversion at 9.5 μm as plotted in Fig. 4.2. The point of the inversion corresponds to the maximum of the resonant intersubband absorption which is measured by means of Fourier transform transmission spectroscopy. The fact that the photocurrent changes its sign by tuning the wavelength indicates that it is mainly caused by the CPGE outweighing the SGE [89]. The

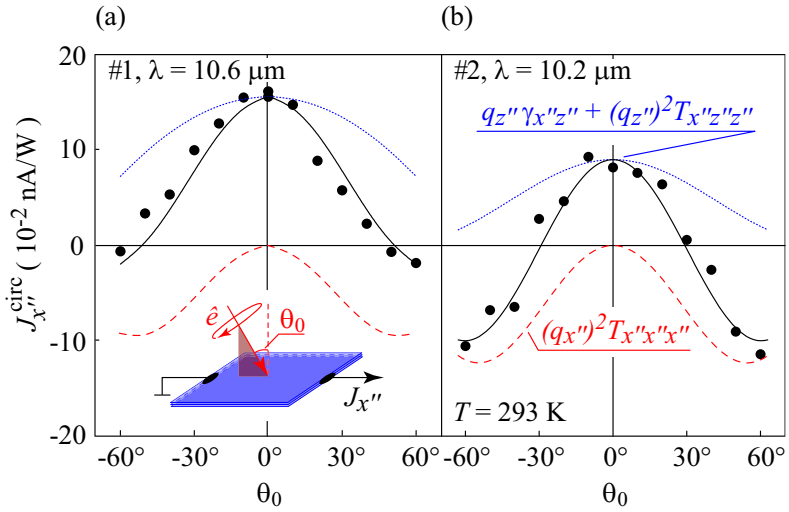

Figure 4.3: Angular dependence of the helicity-dependent current $J^{\mathrm{circ}}_{x''}$ obtained in samples (a) #1 and (b) #2 under mid-infrared excitation with $\lambda = 10.6$ μm and $\lambda = 10.2$ μm, respectively. The plotted curves represent the terms in square brackets (doted blue), the last term on the right hand side of Eq. (4.5) (dashed red), and the sum of all three terms (solid black). The inset shows the experimental geometry.

model picture of the CPGE illustrating the spectral sign inversion of the current at the centre of the absorption line is demonstrated in the Subsec. 2.3.1. This mechanism of the CPGE is based on the spin splitting due to the $\sigma_{z''}k_{x''}$-terms which arise due to the BIA in (110)-oriented both symmetrical and asymmetrical GaAs-based QW structures. In accordance with the phenomenological Eq. (4.2), it predicts that the current reaches its maximum at normal incidence and becomes smaller under oblique incidence keeping the same flow direction.

In order to verify the validity of the phenomenological Eq. (4.2) in respect to the measurements, the current response as a function of the incidence angle θ_0 is studied. In the terahertz range, where the photocurrent is caused by Drude absorption, the data are well described by this equation. However, in the mid-infrared range, a qualitative discrepancy to Eq. (4.2) is observed. In contrast to the sign conserving behaviour of the photocurrent given by $t_p t_s \cos\theta$, the signal in sample #1 changes its sign twice at $\theta_0 \approx \pm 50°$ (see Fig. 4.3(a)). The experiment carried out on sample #2 produced an even more pronounced effect: here, the inversion takes place at $\theta_0 \approx \pm 30°$ (see Fig. 4.3(b)). This angle inversion of the current direction can not be explained in the framework of the conventional theory of the CPGE or optically excited SGE, which ignores the linear momentum transfer from photons to free carriers. Taking into account the linear momentum of the photon, which was neglected in Eq. (4.2), an additional contribution to the current excited by circularly polarised light is obtained. Then, the total helicity-dependent photocurrent in structures of C_s symmetry is given by [90]

$$j_{x''} = t_p t_s \left\{ \left[\left(\gamma_{x''z''} + q_{z''} T_{x''z''z''} \right) \frac{q_{z''}}{q} \right] + q_{x''} T_{x''x''x''} \frac{q_{x''}}{q} \right\} E_0^2 P_{\mathrm{circ}}, \tag{4.4}$$

where $\boldsymbol{T}$ is the third-rank pseudotensor that describes the CPDE current. Following Eq. (4.4), one

obtains the angular dependence of the photocurrent

$$j_{x''} = t_p t_s \left\{ [(\gamma_{x''z''} + qT_{x''z''z''} \cos\theta) \cos\theta] + qT_{x''x''x''} \sin^2\theta \right\} E_0^2 P_{\mathrm{circ}}. \tag{4.5}$$

Equation (4.5) shows that the CPDE given by terms containing the linear photon momentum $\boldsymbol{q}$ can be observed, in principle, at both normal ($\theta = 0°$) and oblique incidence. The distinction between the contributions of the CPGE and CPDE for $\theta = 0°$ may be performed keeping in mind that the replacement $P_{\mathrm{circ}} \to -P_{\mathrm{circ}}$ and $q_{z''} \to -q_{z''}$ conserves the first term in the square brackets on the rhs of Eq. (4.4) while it changes the sign of the second term. Experimentally, it is realised by putting a mirror behind the sample (here, sample #2) and comparing the current magnitudes with and without the mirror. While the gained magnitude of the CPGE under normal incidence given by the coefficient $\gamma_{x''z''}$ is $7{\times}10^{-2}$ nA/W, the strength of the CPDE described by $qT_{x''z''z''}$ is obtained to be $2{\times}10^{-2}$ nA/W. This method has revealed that in the sample #2 both current contributions are nonzero, of the same order of magnitude and have the same sign, however, an application of such technique in every particular structure is difficult as it requires a very high accuracy of adjustment.

Much more reliable access to the CPDE is provided by studying the angular dependence of the photocurrent. Indeed, the terms in square brackets in Eq. (4.5) have a maximum at normal incidence and their contribution to the current decreases with increasing the angle of incidence. At the same time, the CPDE given by the last term in Eq. (4.5) vanishes at normal incidence and increases with $|\theta|$. This interplay of the current contributions may result in the observed twofold sign inversion of the total current by the variation of θ_0 from $-\pi/2$ to $\pi/2$ if the CPDE and CPGE currents have opposite sign. The fits of Eq. (4.5) to the experimental data for both QW structures are shown in figures 4.3(a) and (b). The plotted curves represent the terms in square brackets (doted blue), the last term on the rhs of Eq. (4.5) (dashed red), and the sum of all three contributions (solid black). The correct application of the phenomenological equations is shown for the sample #2 in the Fig. 4.3(b), where the coefficients $\gamma_{x''z''}$ and $qT_{x''z''z''}$ have been obtained from the experiment with the mirror. However, in each sample the value in the round brackets in Eq. (4.5) can be set as a constant, since the CPDE under normal incidence was shown to be small as compared to CPGE. Therefore, in order to fit the data, first, an ordinate scaling parameter for the doted blue curve is estimated to obtain agreement at normal incidence, where the last term on the rhs of Eq. (4.5) vanishes. Then, the dashed curve is scaled to fit the data in the whole range of the incidence angles θ_0. As a result, it can be seen that phenomenological Eq. (4.5) describes well the experimental angular dependence of the photocurrent. The contribution to the circular photon drag effect given by the component $T_{x''x''x''}$ reaches its maximum in GaAs/GaAlAs QW structures at $\theta_0 \approx \pm 50°$ and its magnitude for the sample #2 is $32{\times}10^{-2}$ nA/W demonstrating that the CPDE under oblique incidence is the strongest observed helicity-dependent photocurrent in the particular QW structure.

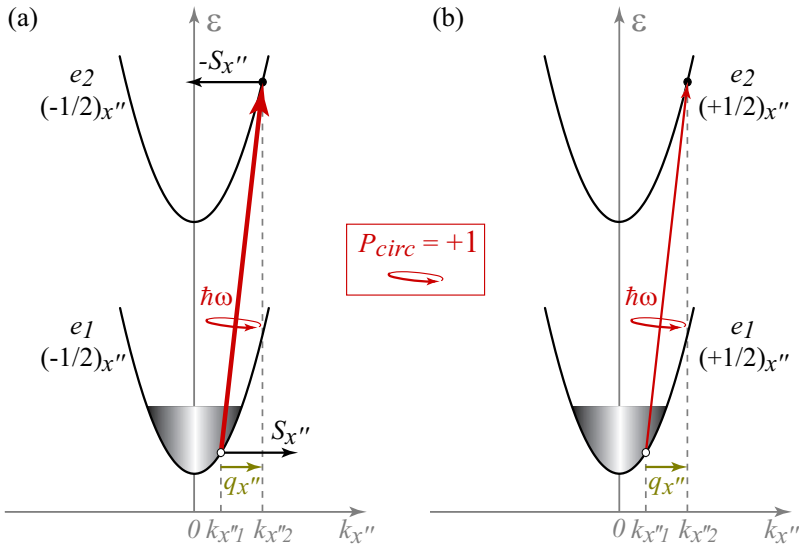

Figure 4.4: Spin-dependent model of the CPDE current. 1st stage: helicity and photon wave vector dependent photoexcitation.

4.2 Microscopical model of circular photon drag effect

The experimental observation of the CPDE has motivated an exciting discussion on its microscopic mechanism. As a result of collaboration, a new spin-related model has been developed [90]. In the following microscopic analysis, the CPDE current excited under oblique incidence is considered which corresponds to the last term on the rhs of the Eq. (4.5) proportional to $T_{x''x''x''}$. Since the tensor $\boldsymbol{T}$ is not invariant under time inversion, dissipative processes should be involved in the microscopic model of the effect. The proposed model includes three stages.

1st stage: Optical spin orientation

The first stage is a helicity and photon wave vector dependent photoexcitation. The intersubband absorption of circularly polarised radiation is a spin-dependent process. While at normal incidence the absorption of circularly polarised light occurs due to spin-flip processes (see Fig. 2.3), under oblique excitation due to selection rules the absorption is dominated by spin-conserving transitions [52]. However, the rates of these transitions are different for electrons with the spin oriented parallel and antiparallel to the in-plane direction of the light wave vector ($q_{x''}$ in Fig. 4.4). For instance, the right-handed circularly polarised light ($P_{\mathrm{circ}} = +1$) excites electrons in the spin-down subband $\sigma_{x''} = -1/2$ with higher probability than those in the spin-up subband $\sigma_{x''} = +1/2$. These spin-conserving transitions are shown by thick and thin tilted arrows in figures 4.4(a) and (b), respectively. Although the arrows are sketched extremely inclined, they point, however, out that the photon wave vector cannot be neglected any more by this type of the optical orientation. As a result of the linear momentum transfer, the optical transitions occur at a distinct initial electron wave vector determined by energy and momentum conservation. The angular momenta of photons yield a spin polarisation $S_{x''}$ at $k_{x''1}$ and $-S_{x''}$ at $k_{x''2}$ in the subbands e_1 and e_2, respectively.

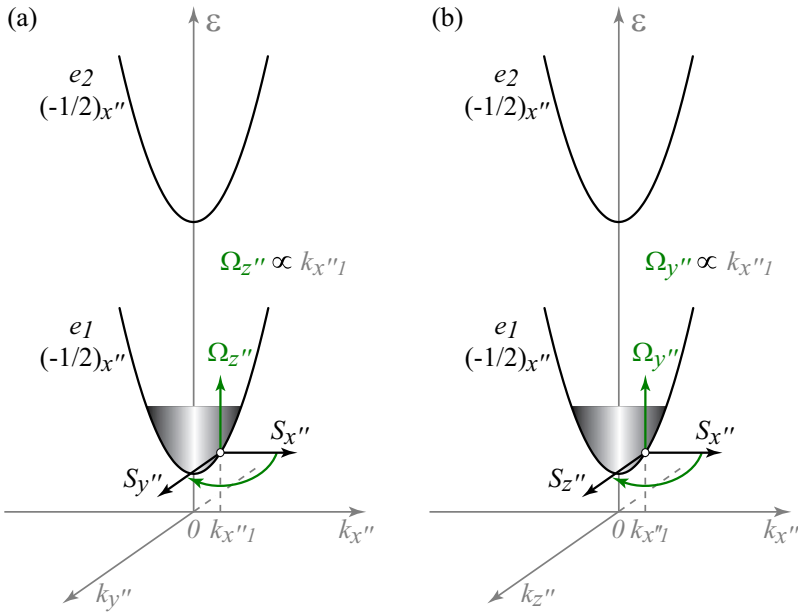

Figure 4.5: Spin-dependent model of the CPDE current. 2nd stage: spin rotation in an effective magnetic field caused by spin-orbit coupling.

These spin polarisations are indicated in Fig. 4.4(a) by antiparallel horizontal arrows. While optical excitation results in a spin polarisation at well determined wave vectors, the electrons in the upper subband have sufficient energy to emit *LO*-phonons and rapidly relax due to this process. Thus, the optically oriented in-plane spin $\boldsymbol{S}$ is determined by the spin polarisation $S_{x''}$ of the electrons in the ground conduction subband with the momentum $k_{x''1}$ (see Fig. 4.4(a)).

2nd stage: Intrinsic spin rotation

The second stage is the electron spin precession in an effective magnetic field $\boldsymbol{\Omega}$ originating from BIA/SIA induced spin-orbit coupling (see Subsec. 2.1.2). The orientation and the strength of this effective magnetic field is determined by the direction and the magnitude of the electron wave vector. Optical orientation in the first stage resulted in spin polarisation $S_{x''}$ of electrons with the wave vector $k_{x''1}$. The effective magnetic field linked to this wave vector has in the C_s point group two components, $\Omega_{z''} \propto k_{x''1}$ and $\Omega_{y''} \propto k_{x''1}$. As a consequence of the spin precession in both field components, new spin projections $S_{y''}$ and $S_{z''}$ appear as shown in figures 4.5(a) and 4.5(b), respectively. Under steady-state excitation, the generation rates of the spin components $S_{y''}$ and $S_{z''}$ are determined by the average angle of spin rotation in the effective magnetic field.

3rd stage: Spin-galvanic effect

In the third stage, the non-equilibrium spin polarisation obtained in the first two stages drive an electric current. This is due to the spin-galvanic effect caused by asymmetric spin-flip relaxation processes (see Subsec. 2.3.2). In (110)-oriented QW structures with both BIA and SIA, the relaxation of both non-equilibrium spin components $S_{y''}$ and $S_{z''}$ may drive an electric current in the x'' direction due to the non-vanishing tensor components $Q_{x''y''}$ and $Q_{x''z''}$ present in this symmetry

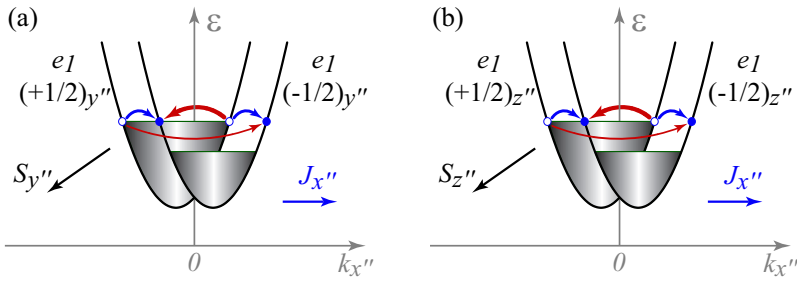

Figure 4.6: Spin-dependent model of the CPDE current. 3rd stage: asymmetrical spin relaxation resulting in an electric current flow due to the spin-galvanic effect.

as given by

$$j_{x''} = Q_{x''y''} S_{y''} \qquad \text{and} \qquad j_{x''} = Q_{x''z''} S_{z''}. \tag{4.6}$$

The conversion mechanism of the spin component $S_{y''}$ into the electric current $j_{x''}$ and the required spin-orbit splitting of the subbands due to $\sigma_{y''} k_{x''}$-terms in the effective Hamiltonian are briefly sketched in Fig. 4.6(a). The difference in carrier populations in the spin branches $\sigma_{y''} = \pm 1/2$ of the ground subband ($n_\uparrow > n_\downarrow$) causes spin relaxation. The asymmetry of the spin-flip relaxation processes results in the non-uniform population of the both spin sublevels and a consequent electric current in the x'' direction. The generation of an electric current due to the relaxation of the spin component $S_{z''}$ is shown in Fig. 4.6(b) where the spin splitting is induced by $\sigma_{z''} k_{x''}$-terms in the Hamiltonian. As it has been demonstrated in [90], the generation rates of the spin components $S_{y''}$ and $S_{z''}$ originating from the optically induced $S_{x''}$ are proportional to the derivative of the intersubband spectral absorbance. Thus, the CPDE current under oblique incidence due to the $T_{x''x''x''}$ tensor component is expected to invert its flow direction while passing the intersubband resonance maximum.

Summarizing all three stages, the microscopic model of the circular photon drag effect under oblique incidence is based on the optical spin orientation and the following asymmetric relaxation. Although the process of the last stage, spin-galvanic effect, was already studied, the first two stages, however, are new and can be considered as as a specific kind of the optical spin orientation which is caused by simultaneous transfer of the photon linear and angular momenta to the carriers and the subsequent spin polarisation alignment due to the spin-orbit interaction in asymmetrical low-dimensional structures.

Chapter 5

Magneto-gyrotropic photocurrents

Illumination of semiconductor materials can lead to generation of photocurrents. In the previous chapter, irradiation of (110)-grown GaAs-based QWs with mid-infrared circularly polarised light has revealed a circular photogalvanic effect and a completely new helicity-dependent phenomenon, the circular photon drag effect. Besides helicity-dependent phenomena, further access to electron spin and orbital features can provide magneto-gyrotropic photogalvanic effects (MGPGE), i.e., those photocurrents which arise in gyrotropic structures in the presence of an external magnetic field. The latter breaks the time inversion symmetry resulting in additional mechanisms of photocurrents which may be of both spin-dependent as well as diamagnetic nature. In the following sections, investigations of MGPGE currents induced by interband, inter- and intrasubband optical transitions in differently constituted QW structures are presented.

5.1 MGPGE in (001)-grown GaAs QWs

An exciting experimental discovery of the CPDE under intersubband absorption of light in GaAs-based QWs motivates to an advanced study of such media. In the present section, photocurrents induced by intersubband optical transitions in (001)-grown GaAs-based QWs subjected to an external magnetic field are considered. It will be shown that the observed magneto-induced photocurrents are related to the gyrotropy of the material caused by BIA and SIA terms. First, experimental studies of the MGPGE photocurrents under illumination with the linearly polarised light in the mid-infrared radiation range are presented. Thereafter, gained data are discussed in terms of both phenomenological and microscopical theory.

5.1.1 Experimental results

The MGPGE photocurrents have been detected in GaAs/GaAlAs QWs under irradiation with mid-infrared light at room and liquid helium temperatures. All experiments have been carried out on (001)-oriented multiple QW structures #3, #4 and #5 characterised by three different quantum well widths of 7.6 nm, 8.2 nm and 8.8 nm, respectively (see Tab. 3.1). These have been consciously chosen to be around 8 nm so that the separation energy between the lowest (e_1) and the second (e_2) conduction subbands matches the photon energy range of a CO_2-laser from 115

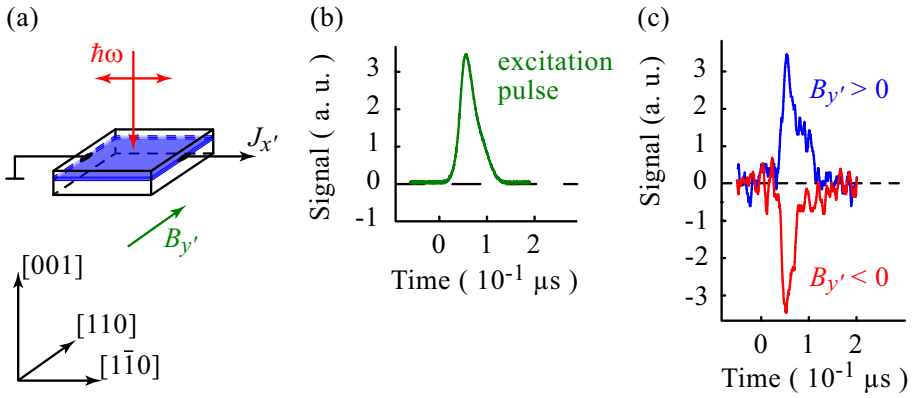

Figure 5.1: (a) Basic experimental geometry of the photogalvanic experiments in an external magnetic field $B_{y'}$, (b) signal pulse of a fast photon drag detector and (c) oscilloscope traces of the current in (001)-grown GaAs-based QWs obtained for pulsed excitation at $\lambda = 10.27$ μm and magnetic fields $B_{y'} = \pm 0.3$ T.

to 135 meV [89, 91]. In order to correlate the spectral dependence of the photocurrent to the absorption spectrum of the QWs, optical transmission measurements have been performed using a Fourier transform infrared spectrometer. The samples have been irradiated at normal incidence, i.e., along the growth direction, as well as at oblique incidence with an angle θ_0 between the light propagation and the QW confinement axis. In respect to the orientation of the crystallographic planes it is convenient to use the prime Cartesian coordinates (2.28)

$$x' \parallel [1\bar{1}0], \quad y' \parallel [110], \quad z' \parallel [001]\,,$$

where x' and y' lie in the QW plane and z' is the growth orientation. The external magnetic field $\boldsymbol{B}$ up to 1 T has been applied parallel to the interface plane.

Irradiation of samples with normally incident linearly polarised radiation in the absence of an external magnetic field causes no photocurrent. This result agrees with the phenomenological theory which does not allow any photocurrent at homogeneous excitation of structures belonging to D_{2d} or C_{2v} point group symmetries relevant for (001)-grown GaAs QW structures [10, 32]. A photocurrent response is obtained only when a magnetic field $\boldsymbol{B}$ is applied. The signal is solely detected in the direction perpendicular to the orientation of the magnetic field, independently whether $\boldsymbol{B}$ is aligned along x' or y'. Since the basic features of the signals remain the same in both geometries, it is sufficient to confine the further consideration on either one. The following results are presented for the photocurrents measured in the x' direction and magnetic field oriented along y' as shown in the Fig. 5.1(a). The signal follows the temporal structure of the laser pulse (Fig. 5.1(b)) and changes its sign upon inversion of the magnetic field direction from $B_{y'} > 0$ to $B_{y'} < 0$ (Fig. 5.1(c)). Besides the experimental geometry with normal incidence of the radiation, the magnetic field induced photocurrent has also been observed at oblique incidence. It should be noted that the excitation of QWs at oblique incidence results in a measurable electric current even at zero magnetic field due to the linear photogalvanic and photon drag effects (for review see [33]). In the present and following sections, magneto-induced currents J^{MGPGE} only are examined, i.e.,

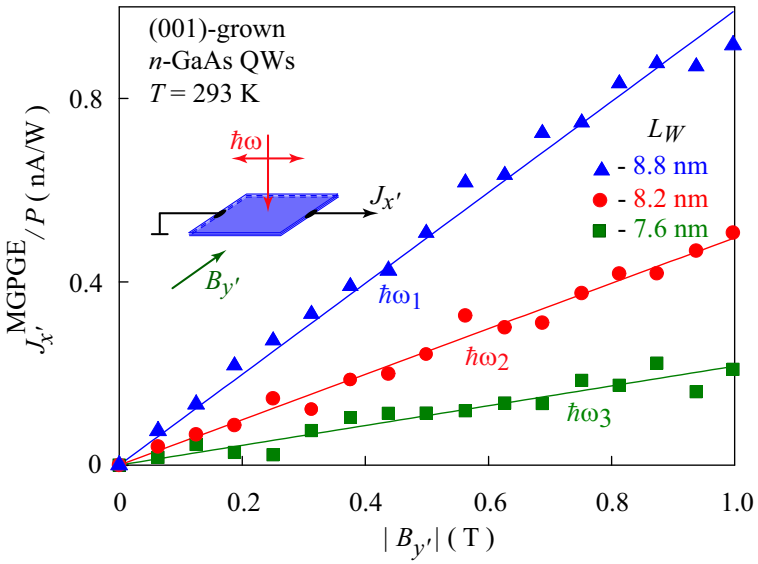

Figure 5.2: Magnetic field dependences of the MGPGE current measured in structures #3–5 of various quantum well width. Data are presented for normal incident mid-infrared radiation with $P \approx 1$ kW at three different photon energies corresponding to the signal maximum in each QW (see arrows in Fig. 5.4).

those currents which reverse their sign upon switching the magnetic field direction. For this reason, current responses $J_{x'}$ for the field aligned along the y' axis (B_+) and along $-y'$ (B_-) are determined and the data are evaluated after

$$J_{x'}^{MGPGE} = [J_{x'}(B_+) - J_{x'}(B_-)]/2\,. \tag{5.1}$$

Magnetic field and polarisation dependences of $J_{x'}^{MGPGE}$ are presented in figures 5.2 and 5.3. As it is shown in Fig. 5.2, the photocurrent exhibits linear dependence on the magnetic field strength in all investigated samples. Figure 5.3 demonstrates the essential difference between the magnetic field induced photocurrents excited at normal and at oblique incidence. While at normal incidence the current is almost independent of the radiation polarisation, at oblique incidence the magneto-induced photocurrent becomes polarisation-dependent: it reaches maximum for the radiation polarised in the incidence plane ($s+p$ - state, $\alpha = 0°$) and minimum for the orthogonal polarisation where radiation electric field has no component normal to the QW plane (s - state, $|\alpha| = 90°$). Figure 5.4 shows the spectral dependences of the photocurrent obtained in the range of photon energies accessible with CO_2-lasers. The data are obtained at normal incidence for a constant magnetic field $B = 0.3$ T in QW structures of various well widths L_W. It is seen that the photocurrent has a resonant character and the peak position energy (PPE) of the resonance shifts to the higher values for narrower QWs (blue shift) that is in accordance with the band structure considerations in the Subsec. 3.1.1. In the Fig. 5.5, the observed current in the sample with multiple QWs of 8.8 nm width is plotted as a function of photon energy $\hbar\omega$ together with the absorption spectrum. The spectral dependence of the photocurrent corresponds to that of intersubband absorption and can be well fitted by a Lorentzian. Decrease of the temperature from 293 K down to

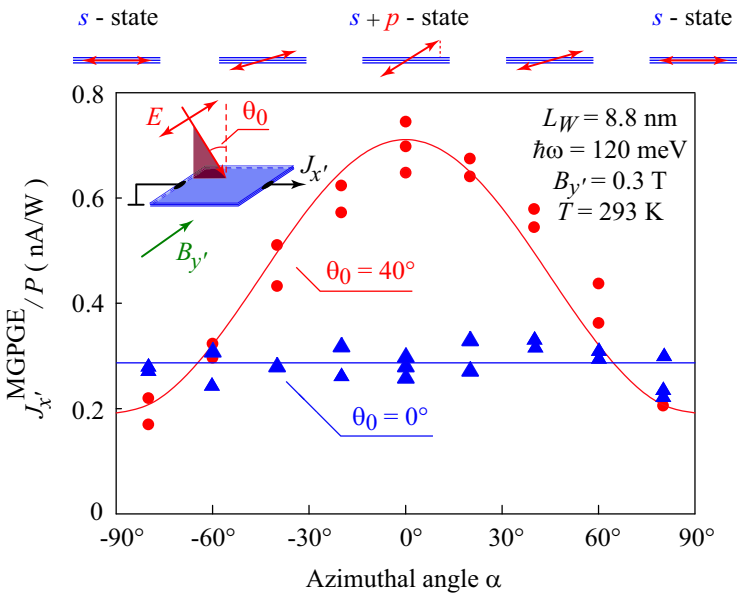

Figure 5.3: Polarisation dependences of the MGPGE current obtained in the sample #5 at normal ($\theta_0 = 0°$) and oblique ($\theta_0 = 40°$) incidence of mid-infrared radiation. In the latter case, the plane of incidence is $x'z'$ and azimuth angle $\alpha = 0°$ corresponds to the maximum value of p-polarisation. Solid curves are fits by an analytical expression given by Eq. (5.3) taking into account the light refraction and absorption in QW structure (see Eq. (5.2)).

12 K strongly enhances the current amplitude. Moreover, the photocurrent resonance performs a blue shift of about 2 meV and narrows if the temperature is reduced (see Fig. 5.6). All the observed features, the coincidence of the photocurrent and the absorbance spectra as well as the spectral shift of the photocurrent resonance peak by both variation of the QW width and temperature demonstrate distinctively that the observed photocurrent is caused by resonant transitions between the first and second electron subbands.

Now, the dependence of the MGPGE photocurrent on the angle of incidence θ_0 and the azimuth angle α is analysed. The QW structures under investigation are considered to be an absorbing uniaxial medium with the optical axis perpendicular to the structure surface. One may assume that in the investigated samples the anisotropy of the refractive index is sufficiently small ($n_{z'} \approx n_{\parallel} \approx n$), but the anisotropy of the absorbance is strong ($\eta_{z'} \gg \eta_{\parallel}$), where the subscripts z' and $\parallel$ correspond to the radiation polarised along the growth direction z' and parallel to the QW plane, respectively. In the case of linearly polarised radiation, the polarisation dependence of the structure absorbance $\eta(\alpha, \theta)$ following to [92] and Fresnel's laws is described by

$$\eta(\alpha, \theta) = t_p^2 \cos^2\alpha(\eta_{\parallel}\cos^2\theta + \eta_{z'}\sin^2\theta) + t_s^2\eta_{\parallel}\sin^2\alpha\,, \tag{5.2}$$

where θ is the angle of refraction in the QW structure, $\sin\theta = \sin\theta_0/n$, t_p and t_s are the transmission coefficients through the sample surface for p- and s-polarised components of the light electric field, respectively. Taking into account the polarisation-independent photocurrent at normal incidence as shown in Fig. 5.3, the polarisation dependence of the MGPGE current under oblique incidence

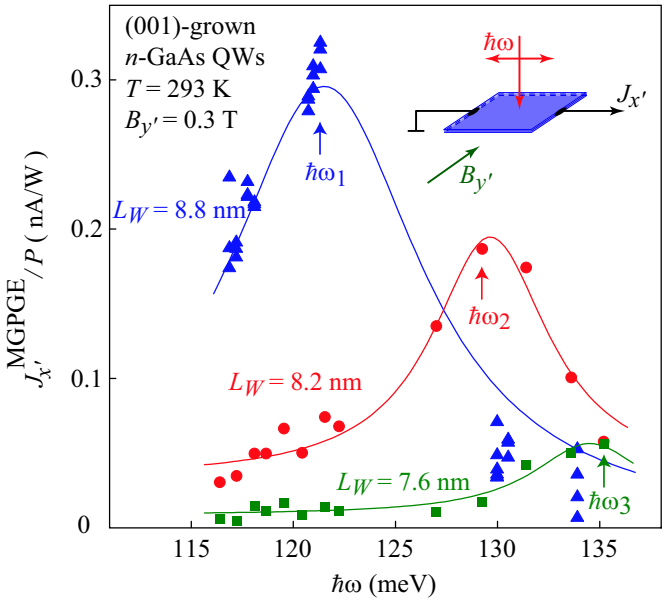

Figure 5.4: Spectral dependences of the MGPGE current obtained for samples #3–5 with various QW widths under normal incidence of the light at room temperature. Solid curves are fits to experimental data by Lorentz functions. Arrows indicate photon energies used in Fig. 5.2.

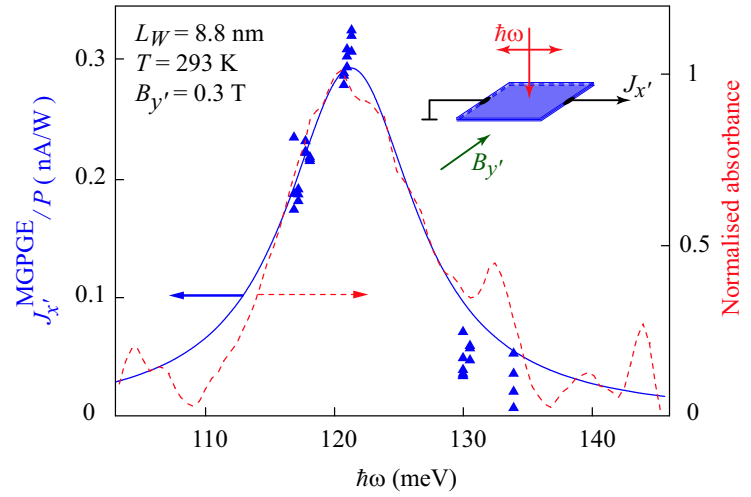

Figure 5.5: Spectral dependence of the MGPGE current obtained in the sample #5. Solid curve is a fit to experimental data (triangles) by a Lorentz function. The dashed curve shows the normalised absorbance spectrum measured in the multiple pass geometry.

may originate solely from the polarisation dependence of the radiation absorbance. In this case the current density has the form

$$j_{x'}^{MGPGE} = \zeta B_{y'} \frac{nc}{4\pi} E_0^2 \eta(\alpha, \theta), \tag{5.3}$$

where ζ is a parameter, E_0 is the electric field amplitude of incident light and c is the light velocity. While in the experiments the electric current $J_{x'}^{MGPGE}$ is measured, in the theoretical

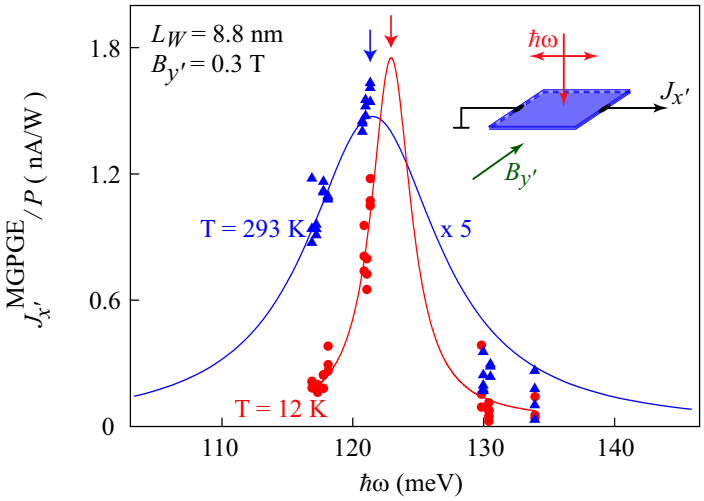

Figure 5.6: Spectral dependence of the MGPGE current obtained in the sample #5 under normal incidence of the light at $T = 12$ K (red) and $T = 293$ K. Solid curves are fits to experimental data by a Lorentz function. The arrows indicate the shift of the peak position energy.

consideration the current density $j^{MGPGE}_{x'}$ is used which is proportional to the current $J^{MGPGE}_{x'}$. The measured polarisation dependences of the photocurrent are fitted by equations (5.2) and (5.3) using, besides the ordinate scaling parameter ζ, the ratio $\eta_{z'}/\eta_{\|}$ as a fitting number. Figure 5.3 shows that the data can be well fitted by Eq. (5.2) for $\eta_{z'}/\eta_{\|} \approx 50$ supporting the assumption that the polarisation dependence of the photocurrent can solely be described by the polarisation dependence of absorption.

As demonstrated above, the MGPGE photocurrent is caused by direct inter-subband transitions. These are usually supposed to be excited by light with the polarisation vector having a nonzero component normal to the QW plane only (for review see [53]) corresponding in the present consideration to the absorbance $\eta_{z'}$. In contrast, the intersubband absorption of light polarised parallel to the QW plane $\eta_{\|}$ is generally expected to vanish because these transitions are forbidden by the dipole selection rules. However, these rules are valid in the framework of the simple one-band model only [52, 54] and it has been experimentally demonstrated that they are not rigorous [55]. The data obtained in this work support this conclusion and show that the absorbance of light with the polarisation vector parallel to the QW plane can be as large as 2 % of the absorbance of the light polarised along the QW growth direction.

5.1.2 Phenomenological analysis

The observed magneto-induced current is related to the gyrotropic properties of the investigated structures. The gyrotropic point group symmetry makes no difference between components of axial and polar vectors, and hence allows an electric current $j_\alpha \propto IB_\beta$, where I is the light intensity inside the sample and B_β are components of the applied magnetic field. The dependence of the photocurrent direction on the light polarisation and orientation of the magnetic field with respect

to the crystallographic axes may be obtained from symmetry considerations which do not require knowledge of the microscopic origin of the effect. Particularly, the MGPGE current in response to linearly polarised radiation and within the linear regime in the magnetic field strength is given by the first term on the rhs of the Eq. (2.26). Now, experimentally studied (001)-grown GaAs-based asymmetrical QW structures of C_{2v} symmetry are considered. In structures belonging to this point group, components of the MGPGE current for $\boldsymbol{B} \parallel y'$ are described by [62]

$$j_{x'} = [C_1(e_{x'}^2 + e_{y'}^2) + C_2(e_{x'}^2 - e_{y'}^2) + C_3\, e_{z'}^2)]B_{y'}I\,, \tag{5.4}$$

$$j_{y'} = C_4 e_{x'} e_{y'} B_{y'} I\,, \tag{5.5}$$

where $(e_{x'}, e_{y'}, e_{z'})$ are components of the unit polarisation vector $\boldsymbol{e}$ inside the medium that is assumed to be real for the linearly polarised radiation and I is the light intensity inside the medium related to the electric field of the incident light E_0 by $I = (ncE_0^2/4\pi)[(t_s^2 - t_p^2)\sin^2\alpha + t_p^2]$. The linearly independent coefficients $C_1 \div C_4$ can be nonzero in QWs of the C_{2v} symmetry and are related to components of the fourth-rank pseudotensor $\phi_{\alpha\beta\gamma\delta}$ (see Sec. 2.4) by

$$\begin{aligned} C_1 &\propto (\phi_{x'y'x'x'} + \phi_{x'y'y'y'})/2 \\ C_2 &\propto (\phi_{x'y'x'x'} - \phi_{x'y'y'y'})/2 \\ C_3 &\propto \phi_{x'y'z'z'} \\ C_4 &\propto 2\phi_{y'y'x'y'} = 2\phi_{y'y'y'x'} \end{aligned} \tag{5.6}$$

and can be extracted directly from the experiment. The fact that at normal incidence ($e_{z'} = 0$, $e_{x'}^2 + e_{y'}^2 = 1$) only a polarisation-independent photocurrent in the direction perpendicular to the magnetic field was observed demonstrates that the coefficients C_2 and C_4 in the present experiments are negligibly small as compared to C_1. At oblique incidence, the polarisation-dependent current contribution determined by the coefficient C_3 is also detected which is found out to be much stronger than the coefficient C_1. Such a behaviour is similar to the polarisation dependence of the QW absorbance η where, in accordance with Eq. (5.2), the radiation polarised in the QW plane causes weaker optical transitions than that having nonzero out-of-plane component of the polarisation vector. As it has been shown, current $\boldsymbol{j}$ can be described solely by the polarisation dependence of η. In this model, the parameters C_1 and C_3 in the phenomenological expression Eq. (5.4) are given by $C_1 = \zeta\eta_{\parallel}$ and $C_3 = \zeta\eta_z$.

5.1.3 Microscopic theory

Microscopically, magneto-gyrotropic photocurrents in QW structures can be of both spin-dependent as well as diamagnetic origin. The proposed spin-dependent mechanisms of photocurrents include asymmetry of direct optical transitions between Rashba–Dresselhaus spin-split branches of the lowest electron subband [93–95], spin-dependent asymmetry of the scattering-assisted radiation absorption by free carriers and spin-dependent energy relaxation of the electron gas heated by the radiation [20, 68] as well as asymmetry of spin-flip relaxation processes [19, 28]. The diamagnetic mechanisms reported so far comprise magnetic field induced photocurrents caused by

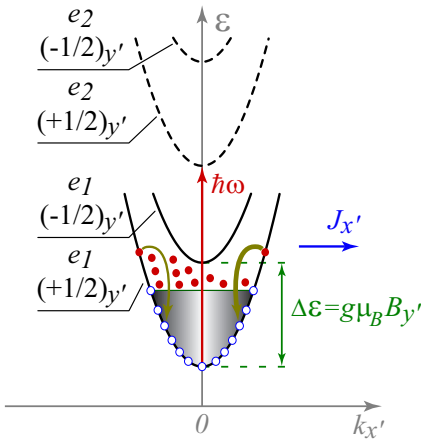

Figure 5.7: Mechanism of MGPGE current at intersubband resonance induced by spin-dependent asymmetry of energy relaxation.

a diamagnetic shift of energy bands [53, 63–66] and diamagnetic corrections to electron-phonon interaction [61, 96, 97]. Various microscopic models of the MGPGE induced by resonant optical transitions between the subbands e_1 and e_2 in the presence of an in-plane magnetic field are considered in detail in [62]. Here, two spin-dependent as well as two diamagnetic mechanisms models are reviewed stressing the most favourable scenarios. For the sake of simplicity, those magneto-induced photocurrents excited at oblique incidence with p-polarised radiation only are concerned. This particular case can be described in a simple single-band model where the intersubband optical transitions are induced by the $e_{z'}$ component of the polarisation vector only. In the phenomenological theory, this contribution to the current corresponds to the last term on the rhs of Eq. (5.4) proportional to the parameter C_3.

Spin-dependent mechanisms of the MGPGE caused by intersubband optical transitions

The group of spin-related MGPGE mechanisms involves spin-dependent asymmetry of photoexcitation and/or relaxation in QWs with equilibrium spin polarisation due to the Zeeman effect and the asymmetry of spin relaxation, i.e., the spin-galvanic effect. However, the model based on the asymmetry of the photoexcitation can be neglected, since the current formation, in contrast to the absorbance, was shown to be polarisation-independent. Two relevant mechanisms considered below are non-sensitive to the polarisation state of the radiation and follow the spectral dependence of the QW absorbance $\eta(\hbar\omega)$.

The first mechanism is based on the spin-dependent asymmetry of electron relaxation and is considered in detail in the Subsec. 2.4.2 for electron gas heated by the Drude-like absorption of the terahertz radiation. The mechanism is based on processes of energy relaxation and, therefore, does not relate on details of optical excitation, besides the strength of absorption. Figure 5.7 sketches the basic physics of this mechanism. Its principle is mostly the same as it was shown above, besides the fact that the electron gas heating proceeds not by means of Drude-like absorption of

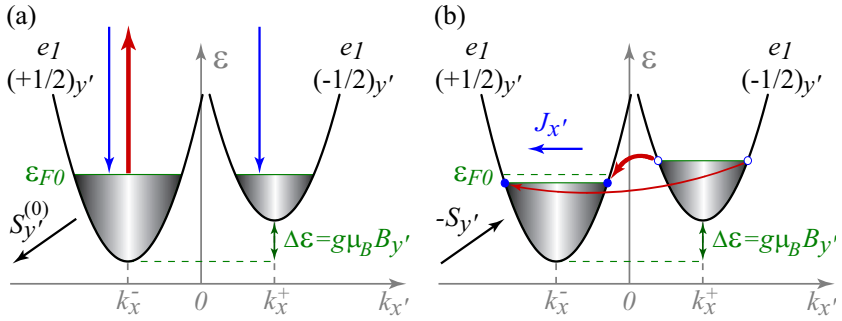

Figure 5.8: Mechanism of MGPGE current at intersubband transitions due to asymmetry of spin relaxation (spin-galvanic effect).

the terahertz light, but by the resonant absorption of the mid-infrared radiation (red arrow) and the subsequent electron scattering to the ground subband. After the emission of optical phonons, the energy of electrons becomes smaller than $\hbar\omega_{LO}$ and the relaxation continues due to the emission of acoustic phonons. The spin-dependent asymmetry of the energy relaxation (downward bent arrows of different thickness) leads to the zero-bias spin accumulation on the edges of the sample. An application of an external magnetic field introduces an equilibrium spin polarisation $\boldsymbol{S^{(0)}}$ in the system. As a result, the pure spin currents are converted into an electric current which is given by Eq. (2.38).

An asymmetry of spin-flip relaxation processes may also be responsible for the current formation and has been previously considered in [28]. It represents in fact the spin-galvanic effect [19] where the current is linked to non-equilibrium spin polarisation

$$j_i = Q_{ij}(S_j - S_j^{(0)})\,. \tag{5.7}$$

Here $\boldsymbol{S}$ is the average non-equilibrium electron spin and $\boldsymbol{S}^{(0)}$ is its equilibrium value. This mechanism requires spin-flip processes together with a non-equilibrium spin polarisation which results from the photoinduced depolarisation of electron spins in the system with equilibrium polarisation $\boldsymbol{S}^{(0)}$ caused by the Zeeman effect. The process of spin depolarisation caused by resonant intersubband transitions to the subband e_2 and a subsequent return to the ground subband e_1 is shown qualitatively in Fig. 5.8(a) by red and blue arrows, respectively. Indeed, due to the fact that in equilibrium electrons preferably occupy the lower spin sublevel (here: $\sigma_{y'} = +1/2$), optical transitions, being proportional to the electron concentration, predominantly excite this branch (thick red arrow). Optically excited electrons under energy relaxation return to both spin sublevels (blue arrows) leading to non-equilibrium spin polarisation. The following spin relaxation (Fig. 5.8(b)) results in the spin-galvanic current which has been considered in the Subsec. 2.3.2. An estimation of this photocurrent for the DP spin relaxation mechanism yields

$$j_{x'} \sim e\tau_p^{(1)}\, S_{y'}^{(0)}\, \frac{\chi^{(1)}_{x'y'}}{\hbar}\, \frac{I\eta(\hbar\omega)}{\varepsilon_{21}}\,, \tag{5.8}$$

where $\chi^{(1)}$ is the constant of $\boldsymbol{k}$-linear spin-orbit splitting of the subband e_1 due to BIA and SIA contributions and $S_{y'}^{(0)}$ is given by Eq. (2.36).

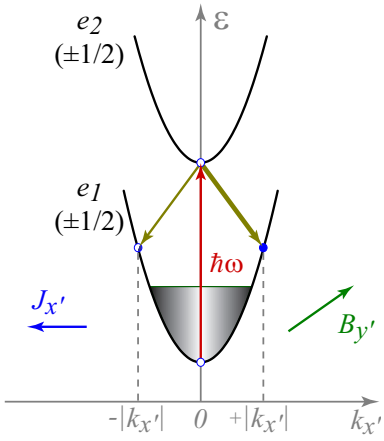

Figure 5.9: Mechanism of MGPGE current at intersubband resonance induced by asymmetric free carrier relaxation due to $\boldsymbol{k}$-linear diamagnetic terms in the scattering amplitude.

Diamagnetic mechanisms of the MGPGE caused by intersubband optical transitions
The group of diamagnetic mechanisms comprises two current contributions. The first one originates from the diamagnetic band shift of subbands and the second one stems from the $\boldsymbol{k}$-linear diamagnetic corrections to the scattering amplitude. In the following, for the simplicity, linear-in-$\boldsymbol{k}$ corrections caused by the SIA are considered.

As it has been demonstrated in the Subsec. 2.4.1, an in-plane magnetic field applied to an asymmetric 2DEG induces a diamagnetic shift of the electron spectrum in $\boldsymbol{k}$-space in each size-quantised subband [53]. The electric current driven by the relative diamagnetic shift of the subbands is expected to be strong compared to the spin-dependent mechanisms due to its non-relativistic nature. However, this mechanism predicts a current inversion at the intersubband absorption resonance which contradicts the experimental observations (see Fig. 5.5). In contrast, the proposed diamagnetic contribution below predicts a photocurrent which spectral dependence follows the QW intersubband absorbance.

The mechanism based on the $\boldsymbol{k}$-linear diamagentic terms in the amplitude of scattering to the ground conduction subband is up to now the most favourable scenario of the MGPGE caused by intersubband optical transitions. In the previous models, such scattering has been considered to be independent on the electron wave vector $\boldsymbol{k}$. The present model, however, demonstrates that the asymmetry of these relaxation processes can lead to a current generation. The basic features of this mechanism are depicted in Fig. 5.9. The direct intersubband optical transitions are shown by a vertical red arrow and the subsequent intersubband scattering to the ground subband by tilted downward yellow arrows. In gyrotropic quantum wells subjected to an external magnetic field, the matrix element of intersubband scattering by static defects or phonons contains an additional term proportional to $(B_{x'}k_{y'} - B_{y'}k_{x'})$. Therefore, the scattering rates to final states with positive and negative wave vectors $k_{x'}$ become different as reflected in Fig. 5.9 by arrows of different thickness. Such an imbalance caused by asymmetry of the intersubband scattering results in an electric current in the ground subband which is proportional to the applied magnetic field and de-

cays with the momentum relaxation time $\tau_p^{(1)}$. It should be mentioned that the energy relaxation of the electrons within the ground subband, which follows the intersubband scattering, becomes also asymmetrical in the presence of an in-plane magnetic field [96,97] and contributes the total current. The estimations of the $\boldsymbol{k}$-linear diamagnetic corrections in the electron scattering amplitude and the corresponding MGPGE current are given in [62] demonstrating that this current contribution becomes nonzero in asymmetric QW structures and may even determine the MGPGE behaviour in real structures.

Summarizing the microscopic analysis, it has been demonstrated that both spin-dependent as well as diamagnetic mechanisms may cause the observed current induced by intersubband optical transitions in the presence of an in-plane external magnetic field in (001)-grown asymmetrical GaAs/GaAlAs QWs. Unfortunately, these models can not be distinguished qualitatively. Based on quantitative estimations [62], the strongest current contribution is expected to originate from $\boldsymbol{k}$-linear diamagnetic terms in the scattering amplitude yielding asymmetric relaxation of carriers in $\boldsymbol{k}$-space. Investigating spin and orbital features, it should be noted that spin-dependent and diamagnetic mechanisms might be qualitatively distinguished in structures where the g-factor can be varied, e.g., by temperature tuning in DMS materials [69] or by well width variation in QW structures [98–100]. Indeed, while spin-dependent mechanisms are proportional to the g-factor, diamagnetic mechanisms are non-sensitive to the Zeeman splitting. Another way is the unilateral enhancement of the spin-dependent mechanisms in structures with both large spin-orbit coupling and g-factor such as HgTe-based QWs.

5.2 MGPGE in (001)-grown HgTe QWs

In the previous section, a novel MGPGE under intersubband resonance in GaAs-based QWs has been observed. However, a distinctive qualitative separation between spin-dependent and diamagnetic mechanisms of the current formation was not possible. Emphasizing the first group of the phenomena, i.e., the spin photocurrents, one can expect their enhancement in systems with large spin-orbit coupling. In particular case of the spin investigation by means of pure spin currents, a large g-factor is of an additional interest. Therefore, quantum well structures based on HgTe appear to be very attractive especially for the study of fundamental spin-orbit effects. Indeed, narrow gap HgTe-based QWs are characterised by an extraordinary large Rashba spin-orbit splitting which can reach values up to 30 meV [101, 102] and a large g-factor of about -20 [103]. Even though an amplification of the spin currents is anticipated, the orbital features of the carriers should not be excluded a priori from the general treatment of the phenomena. The current section focuses on studies of MGPGE in (001)-grown HgTe-based QWs.

5.2.1 Experimental results

The MGPGE has been detected in the HgTe/HgCdTe QW structures under illumination with terahertz as well as mid-infrared radiation in the range from liquid helium up to room temperature. All measurements have been carried out on samples #6,#7,#8 and #9 which are entirely characterised

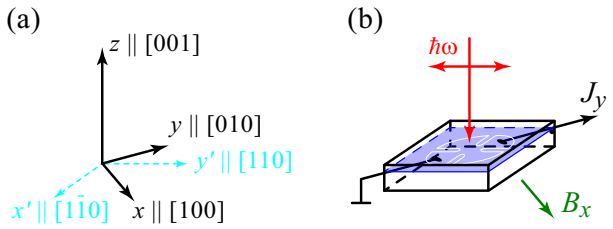

Figure 5.10: (a) Cubic (black) and prime (light blue) coordinate systems as given by equations (2.6) and (2.28), respectively, and (b) basic geometry of the photogalvanic experiments on HgTe-based QW structures under normal incident excitation in mid-infrared and terahertz range in the presence of an in-plane magnetic field $\boldsymbol{B}$.

in the Subsec. 3.1.2 and feature QW widths of 5, 8, 12 and 22 nm, respectively. Optical excitation occurred at normal incidence in order to exclude the photon drag effect [104,105] and other known mechanisms of current generation at oblique incidence [32,33].

Mid-infrared excitation

Mid-infrared radiation with photon energies about 120 meV causes in all samples used in experiments direct interband optical transitions. Irradiating samples at normal incidence, for the in-plane magnetic field $\boldsymbol{B}$, a photocurrent signal in the perpendicular direction has been observed. In the cubic Cartesian system (2.6),

$$x \parallel [100], \quad y \parallel [010], \quad z \parallel [001],$$

where x and y are oriented along the cubic axes in the QW plane and z indicates the confinement axis (see Fig. 5.10(a)), an application of the magnetic field $\boldsymbol{B}$ along x generates photocurrent $\boldsymbol{J}$ in y direction as shown in the Fig. 5.10(b). The signal depends linearly on the radiation power up to $P \approx 1.2$ kW, the highest power used in the mid-infrared experiments with Q-switched CO_2-laser as an excitation source. In Fig. 5.11 the magnetic field dependence of the photocurrent is plotted for the structure with the well width of 12 nm. The data are obtained at $T = 200$ K for two polarisation states of the radiation with the electric field $\boldsymbol{E}$ of the light wave aligned parallel and perpendicularly to the magnetic field. In both cases, the signal is an odd function of $\boldsymbol{B}$. Its strength and behaviour upon variation of $\boldsymbol{B}$ depends, however, on the orientation of the radiation electric field vector. Figure 5.12 shows the dependence of the photocurrent J_y on the orientation of polarisation plane specified by the angle α. The data can be well fitted by the equation

$$J_y(\alpha, B_x) = J_0(B_x) + J_1(B_x)\cos 2\alpha + J_2(B_x)\sin 2\alpha. \tag{5.9}$$

Below it will be demonstrated that exactly these dependences follow from the theory. Recording signals for two fixed polarisation directions, it is possible to extract two individual contributions: the polarisation-independent background J_0 and the amplitude of one of the polarisation-dependent

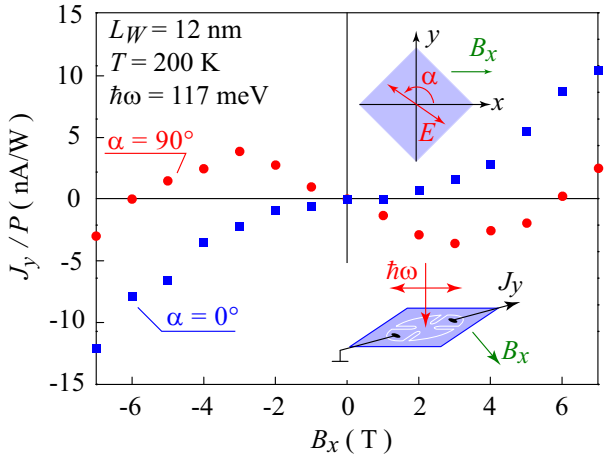

Figure 5.11: Magnetic field dependence of the MGPGE current measured in a HgTe-based QW structure #8 with the well width L_W=12 nm at $T = 200$ K for two states of polarisation ($\alpha = 0°, 90°$). Data are presented for mid-infrared radiation with $\hbar\omega = 117$ meV and $P \approx 0.3$ kW. The insets show the experimental geometry and the orientation of the light electric field $\boldsymbol{E}$ and the external magnetic field $\boldsymbol{B}$ with respect to the sample orientation.

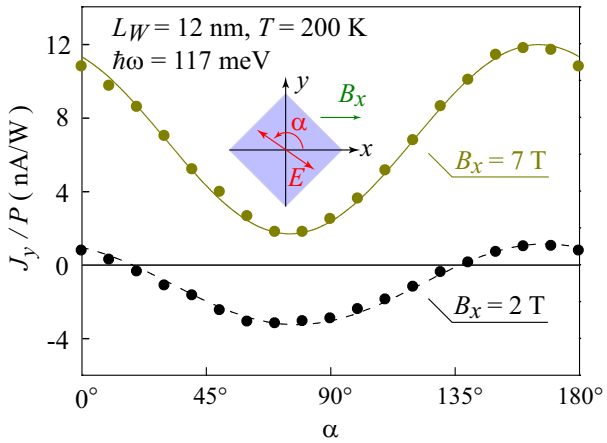

Figure 5.12: Polarisation dependences of the MGPGE current at mid-infrared excitation in the sample #8 at $T = 200$ K for two magnetic field strengths. The data are fitted after equations (5.9) and (5.14). The inset shows the orientation of the light electric field $\boldsymbol{E}$ and the external field $\boldsymbol{B}$ with respect to the sample orientation.

contributions J_1[1]

$$J_0 = \frac{J_y(0°) + J_y(90°)}{2}, \quad J_1 = \frac{J_y(0°) - J_y(90°)}{2}. \tag{5.10}$$

Figure 5.13 shows magnetic field dependences of J_0 and J_1 for two samples with the well widths of 8 nm and 22 nm at $T = 200$ K. The signal behaviour is different for these structures. While for the QW with $L_W = 8$ nm the photocurrent depends linearly on the magnetic field, in the structure

[1]Since both polarisation-dependent components J_1 and J_2 in Eq. (5.9) stem from the same microscopic mechanism [28], it is sufficient to focus on either contribution.

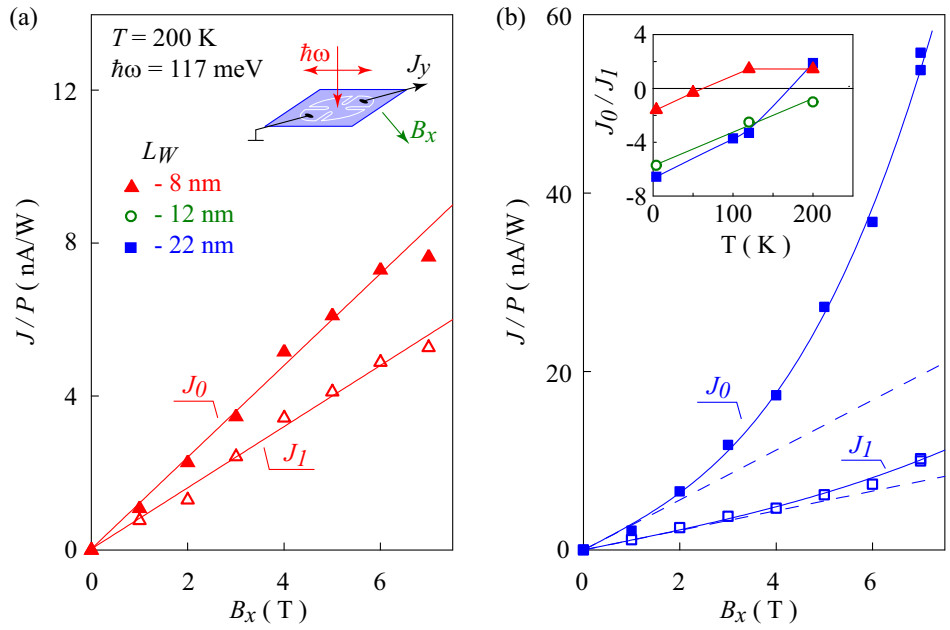

Figure 5.13: Magnetic field dependence of the polarisation-independent current J_0 and polarisation-dependent current J_1 obtained for (a) sample #7 with $L_W = 8$ nm and (b) sample #9 with $L_W = 22$ nm at $T = 200$ K. The data are fitted after equations (5.11) and (5.14). For the narrow structure in (a) the fitting is limited by linear terms. Dashed lines in (b) demonstrate the linear contribution only. Insets show the experimental geometry and temperature dependence of the ratio J_0/J_1 for QWs with $L_W = 8$, 12 and 22 nm at $B = 1$ T.

with $L_W = 22$ nm the current can be described by a superposition of linear-in-B and cubic-in-B terms:

$$J_y(B) = aB + bB^3 \ . \tag{5.11}$$

Figure 5.13(b) demonstrates that the B^3-term is more pronounced in the polarisation-independent photocurrent J_0. Therefore, the attention below will be focussed in particular on it because the measurements reveal that this contribution dominates the total current in the almost entire temperature range, even at low magnetic fields where the total photocurrent is mostly linear-in-B as shown in the inset in Fig. 5.13(b) for $B = 1$ T. While the linear dependence of the photocurrent on magnetic field is previously reported for various structures (for review see [28, 29]), the observation of the cubic in magnetic field photocurrent is unexpected and has not been detected so far. Moreover, the last term in Eq. (5.11) corresponding to J_0 is strong and overcomes the linear-in-B contribution at the magnetic field about 6 T. Similar behaviour is observed in the structure with $L_W = 12$ nm. However, in this sample the coefficients a and b for polarisation-independent photocurrent J_0 have opposite signs resulting in a sign inversion observed for B about 4 T (see Fig. 5.14(a)). In the structure with $L_W = 5$ nm the signals were too small to conclude definitely on the magnetic field dependence, which has been, however, measured at the excitation with terahertz radiation. The decrease of the temperature drastically affects the experimental data. At intermediate temperature of 120 K, it has been observed that the linear-in-B contribution in QW with $L_W = 22$ nm changes

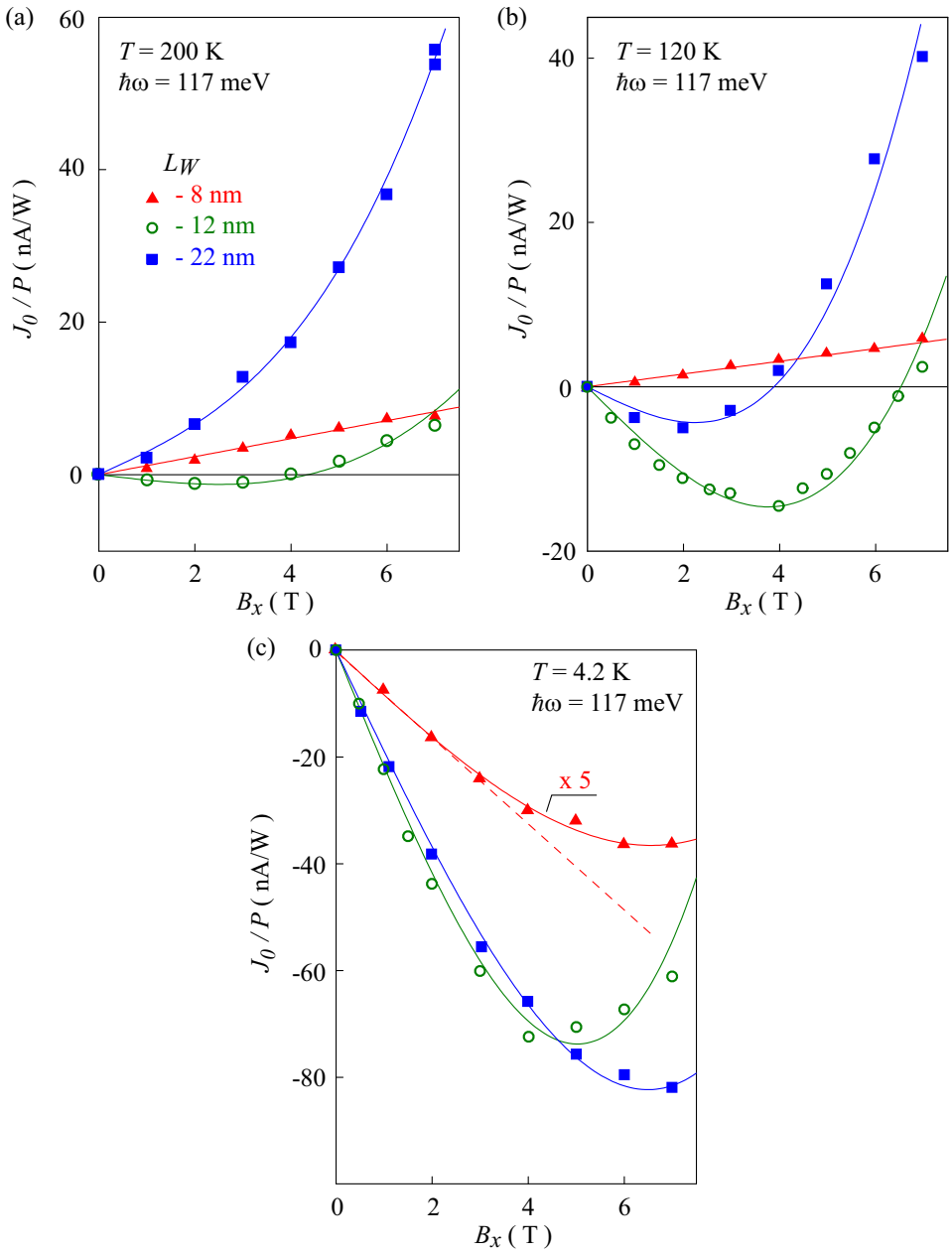

Figure 5.14: Magnetic field dependences of the current J_0 obtained in samples #7–9 of three different well widths at three different temperatures. Data are fitted after equations (5.11) and (5.14). The dashed red line in (c) is plotted according to the linear law.

its sign (see Fig. 5.14(b)). With rising B, the magnitude of the B^3-term causes the sign inversion of the photocurrent J_0. In the sample with $L_W = 8$ nm the data are still well described by the linear-in-B dependence. Further reduction of temperature to the liquid helium conditions results in the sign inversion of the linear-in-B current in structure with $L_W = 8$ nm as well yielding also the cubic-in-B component (see Fig. 5.14(c)). Now, the magnetic field dependences in all samples are described by sum of linear- and cubic-in-B terms with pre-factors of opposite signs. The total

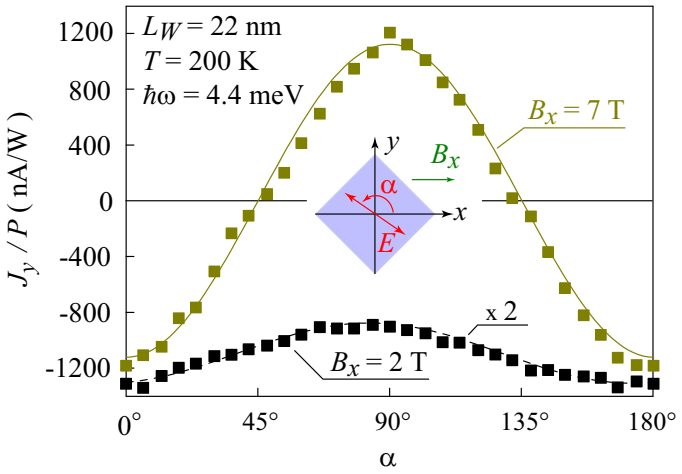

Figure 5.15: Polarisation dependences of the MGPGE current excited by terahertz radiation ($\hbar\omega$ = 4.4 meV) in the sample #9 with L_W = 22 nm at T = 200 K for two magnetic field strengths. The data are fitted after equations (5.9) and (5.14). The inset shows the orientation of the light electric field $\boldsymbol{E}$ and the magnetic field $\boldsymbol{B}$ with respect to the sample orientation.

current tends to the sign inversion, however, at substantially higher magnetic fields B.

Terahertz excitation

Spectral dependence of the MGPGE current may provide an important information on its origin. Therefore, excitation of HgTe/HgCdTe QW structures with the light in the terahertz range appears to be of a high advantage. In this optical region, the photon energies within several meV are much smaller than the energy gap and the inter(sub)band separation. Therefore, such radiation causes only Drude-like optical transitions. In the terahertz range, magneto-induced photocurrents have been observed in all structures, including sample with L_W = 5 nm, and at all wavelengths used. Like in the mid-infrared range, the signal depends on the radiation polarisation (see Fig. 5.15) and is well described by Eq. (5.9). Figure 5.16(a) shows the magnetic field dependence of the polarisation-independent photocurrent J_0 obtained in the wide QW with L_W = 22 nm in response to the radiation of the photon energy $\hbar\omega$ = 4.4 meV demonstrating that also in the terahertz range the current is well described by the Eq. (5.11) with significant contribution of the cubic-in-B term at high fields. At liquid helium temperature, a peak in the magnetic field function[2] has been detected. It has a maximum at $B \approx 4$ T and a half-width of about 0.75 T. Decreasing the photon energy of the applied radiation down to $\hbar\omega$ = 2.5 meV, the peak position shifts to lower magnetic field values ($B \approx 2.3$ T) scaling linearly with the photon energy (see Fig. 5.16(b)). At higher photon energy $\hbar\omega$ = 8.4 meV, no peak has been detected at $B \leq 7$ T. Similar behaviour is also detected in the polarisation-dependent contribution J_1, however, the peak in this contribution is much less pronounced. The most favourable explanation of the peak appearance is the ionisation of the partially occupied impurity levels at low temperatures [106]. The spectral dependence of the four MGPGE contributions, i.e., linear- and cubic-in-B components of currents J_0 and J_1, is

[2] A dip for the absolute value of the signal.

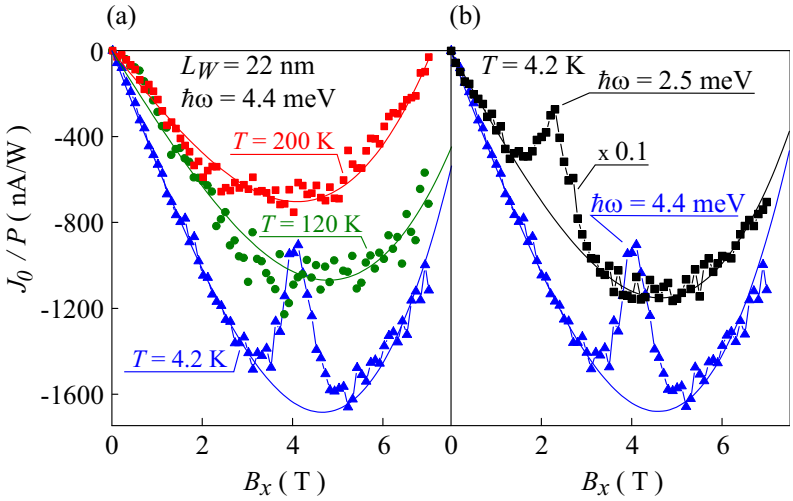

Figure 5.16: Magnetic field dependences of the photocurrent J_0 excited by terahertz radiation in the sample #9 with $L_W = 22$ nm. (a) The photocurrent is measured in response to the radiation with photon energy of $\hbar\omega = 4.4$ meV at three temperatures. (b) The photocurrent is measured at liquid helium temperature (4.2 K) in response to the radiation of two photon energies. The lines are plotted according to equations (5.11) and (5.14).

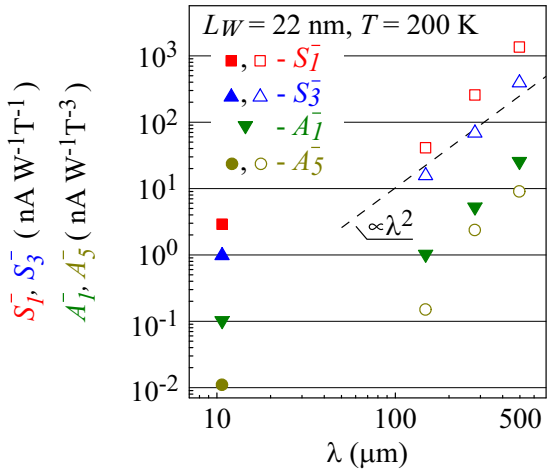

Figure 5.17: Wavelength dependences of the absolute values of coefficients S_1^-, S_3^-, A_1^- and A_5^- (see Eq. (5.14)) obtained for sample #9 at $T = 200$ K. Full symbols correspond to negative values of the coefficients. The dashed line is plotted according to the wavelength square law.

demonstrated in the Fig. 5.17. One can see that moving from the mid-infrared range ($\lambda = 10.6\,\mu$m) to the longest wavelength used in the terahertz spectrum ($\lambda = 496\,\mu$m), all current contributions drastically increase by more than two orders of magnitude. Moreover, some contributions invert their sign with wavelength variation (full symbols).

In contrast to wide QWs, in the narrowest QW sample with $L_W = 5$ nm the photocurrent was found to behave only linearly on the magnetic field B. This is demonstrated in Fig. 5.18(a) for both polarisation-dependent and -independent photocurrents obtained at $T = 200$ K and excitation with

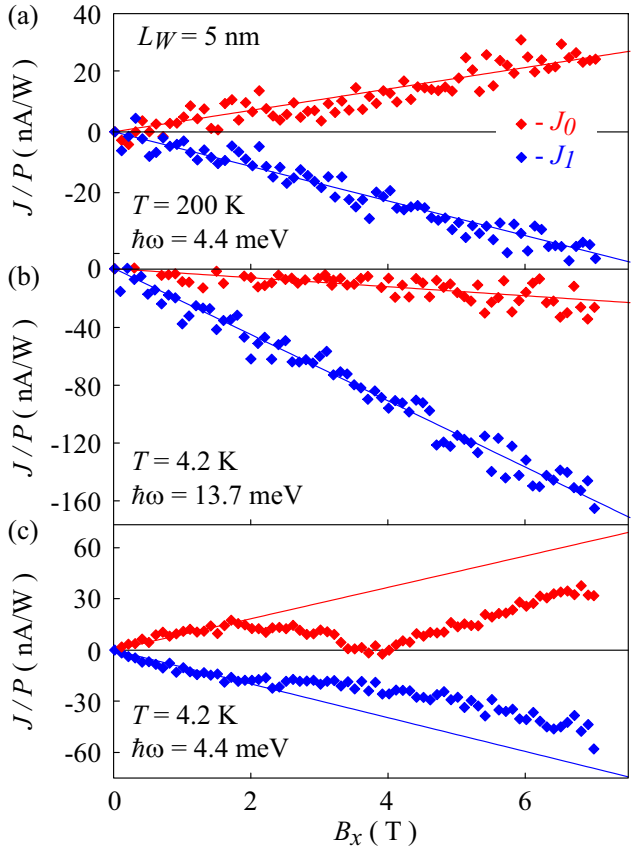

Figure 5.18: Magnetic field dependence of photocurrents J_0 (red) and J_1 (blue) excited by terahertz radiation in the sample #6 with $L_W = 5$ nm. (a) The data are presented for $T = 200$ K and $\hbar\omega = 4.4$ meV. ((b)–(c)) Photocurrents measured at $T = 4.2$ K in response to the radiation with the photon energies (b) $\hbar\omega = 13.7$ meV and (c) $\hbar\omega = 4.4$ meV. The full lines are plotted according to equations (5.11) and (5.14) with coefficients b and $A^{-}_{1,5}$ equal to zero.

the photon energy $\hbar\omega = 4.4$ meV. The linear behaviour of the photocurrent is observed even at low temperatures down to 4.2 K applying radiation with higher photon energy of $\hbar\omega = 13.7$ meV (see Fig. 5.18(b)). At excitation with lower energy $\hbar\omega = 4.4$ meV, however, this behaviour is masked by a wide dip presented in the magnetic field dependence of the photocurrent (see Fig. 5.18(c)). At this photon energy the magnetic field position of the dip is close to that observed in the QW with $L_W = 22$ nm ($B \approx 4$ T), but it is much wider and characterised by a half-width of at least 3 T. Like in the wide QWs, at higher photon energies no dip has been detected for $B \leq 7$ T allowing one to analyse the magnetic field dependence unaffected by the dip.

5.2.2 Theoretical discussion

The most surprising experimental result is definitely the observation of the cubic-in-B contribution to the MGPGE current. Before attempting to understand its microscopic origin, first, an approach of phenomenological description should be made.

Phenomenological description

Considering the symmetry of the structure under investigation as well as experimental geometry it is possible to derive the phenomenological equations for the observed photocurrents. Holding the linear and cubic in the magnetic field strength B terms, MGPGE current for unpolarised or linearly polarised radiation at normal incidence is given by [80]

$$\begin{aligned} j_\alpha = &\sum_{\beta\gamma\delta} \phi_{\alpha\beta\gamma\delta}\, B_\beta\, \frac{e_\gamma e_\delta^\star + e_\delta e_\gamma^\star}{2} I \\ &+ \sum_{\beta\mu\nu\gamma\delta} \Xi_{\alpha\beta\mu\nu\gamma\delta}\, B_\beta B_\mu B_\nu\, \frac{e_\gamma e_\delta^\star + e_\delta e_\gamma^\star}{2} I\,. \end{aligned} \tag{5.12}$$

Here $\boldsymbol{\phi}$ and $\boldsymbol{\Xi}$ are fourth- and sixth-rank pseudotensors, respectively, being symmetric in the last two indices, e_γ are components of the unit vector of light polarisation, and I is the light intensity set as $I = E_0^2$. Determination of the non-vanishing components of pseudotensors $\boldsymbol{\phi}$ and $\boldsymbol{\Xi}$ requires the knowledge about the point group affiliation of the investigated structures. The analysis given in the Subsec. 3.1.2 has revealed that all HgTe-based QWs are asymmetrical and, thus, belong to the C_{2v} point group symmetry. In this case, the tensors $\boldsymbol{\phi}$ and $\boldsymbol{\Xi}$ have six and twelve linearly independent components, respectively. Assuming normally incident linearly polarised or unpolarised light and the in-plane magnetic field, in the prime coordinate system (2.28) the Eq. (5.12) is reduced to set of normalised current projections [80]

$$\begin{aligned} j_{x'}/I = &\left[S_1 B_{y'} + 2S_2 B_{y'} P_{\rm lin} + 2S_3 B_{x'} P'_{\rm lin}\right] \\ &+ B_{y'}[A_1 B^2 + A_2(B_{x'}^2 - B_{y'}^2)] \\ &+ 2B_{y'}[A_3 B^2 + A_4(B_{x'}^2 - B_{y'}^2)] P_{\rm lin} \\ &+ 2B_{x'}[A_5 B^2 + A_6(B_{x'}^2 - B_{y'}^2)] P'_{\rm lin}\,, \\ j_{y'}/I = &\left[S'_1 B_{x'} + 2S'_2 B_{x'} P_{\rm lin} + 2S'_3 B_{y'} P'_{\rm lin}\right] \\ &+ B_{x'}[A'_1 B^2 + A'_2(B_{x'}^2 - B_{y'}^2)] \\ &+ 2B_{x'}[A'_3 B^2 + A'_4(B_{x'}^2 - B_{y'}^2)] P_{\rm lin} \\ &+ 2B_{y'}[A'_5 B^2 + A'_6(B_{x'}^2 - B_{y'}^2)] P'_{\rm lin}\,, \end{aligned} \tag{5.13}$$

where S_i and A_j are the linearly independent components of the tensors $\boldsymbol{\phi}$ and $\boldsymbol{\Xi}$, respectively. The polarisation dependence of the photocurrent is determined by the Stokes parameters $P_{\rm lin}$ and $P'_{\rm lin}$ given in Eq. (2.31). Since the magnetic field in the experiments was oriented along the cubic x axis and the current measured along y, the set of equations (5.13) can be rewritten as follows

$$\begin{aligned} j_y/I = &B_x(-S_1^- + S_2^- \sin 2\alpha - S_3^- \cos 2\alpha) \\ &+B_x^3(-A_1^- + A_3^- \sin 2\alpha - A_5^- \cos 2\alpha), \end{aligned} \tag{5.14}$$

where $S_l^- = (S_l - S'_l)/2$, $A_l^- = (A_l - A'_l)/2$ and α is an angle between the linear polarisation direction and the x axis. From these relations, the polarisation-independent and polarisation-dependent contributions to the MGPGE current measured in the experiment can be expressed in

terms of the non-vanishing components as

$$J_0 \propto -(B_x S_1^- + B_x^3 A_1^-), \tag{5.15}$$

$$J_1 \propto -(B_x S_3^- + B_x^3 A_5^-), \tag{5.16}$$

$$J_2 \propto (B_x S_2^- + B_x^3 A_3^-).$$

Equation (5.14) describes well the macroscopic features of the photocurrent. In accordance with the experimental data, it contains both linear- and cubic-in-B contributions and fully characterises the observed polarisation dependences in both mid-infrared as well as terahertz range. Figure 5.13 shows that at low fields ($B \leq 1$ T) the linear parts of the total photocurrents dominate possessing both polarisation-independent J_0 as well as polarisation-dependent J_1 contributions which are given by the coefficients S_1^- and S_3^-, respectively. The temperature dependence of the ratio $J_0/J_1 = S_1^-/S_3^-$ is presented in the inset to Fig. 5.13(b) and shows that polarisation-independent contribution J_0 (S_1^-) dominates the total photocurrent over almost the entire temperature range. In the narrowest QW with $L_W = 5$ nm and in QW with $L_W = 8$ nm at high temperature the linear-in-B behaviour remains up to the highest magnetic fields applied. In other samples, by contrast, for $B > 1$ T the cubic-in-B contribution is clearly detected and even dominates the photocurrent. In fact, all experimental data is properly described in terms of the phenomenological theory. However, the microscopic origin of the observed linear-in-B and cubic-in-B photocurrent contributions is not clear so far.

Microscopical approach

In the following approach, the microscopic roots of the observed photocurrent and especially of the cubic-in-B contribution are concerned. For this purpose, the knowledge about the band structure of the material is of essential importance. Depending on the actual well width and temperature, the ordering of bands in HgTe/HgCdTe QWs is either normal or inverted. As mentioned in the Subsec. 3.1.2, in a definite well width region above $L_{\text{inv}} = 6.3$ nm, simple temperature variation allows to switch between trivial and non-trivial regimes. The band structure of the QW with $L_W = 8$ nm at liquid helium and room temperatures is sketched in the Fig. 5.19 together with the respective Fermi energies and possible direct optical transitions corresponding to the photon energy $\hbar\omega = 117$ meV used in the experiment with mid-infrared radiation. The band structure calculated using the eight-band $\boldsymbol{k}\cdot\boldsymbol{p}$ model in envelope function approximation [79, 80, 107] excludes, however, the strong Rashba spin splitting of subbands. The latter are labelled as heavy-hole- (hh_i), electron- (e_i) and light-hole-like (lh_i) in accordance with the properties of the corresponding wave functions at $k_\parallel = 0$ [108]. Figure 5.19 demonstrates that while at 4.2 K nanostructures with 8 nm wide wells are characterised by the inverted band structure, at room temperature they have a trivial band sequence. At fixed temperature of 4.2 K, the band ordering is normal below the critical width of about 6.3 nm and inverted above this value [25]. So far the critical width of the band ordering inversion depends on two parameters, however, for the analysis of the experimental data only several relevant cases are concerned. The lowest conduction band states for all samples used in the experiments and two characteristic temperatures, 4 K and 200 K, are given in Tab. 5.1. The analysis of the band structure of the investigated samples reveals that the nonlinear MGPGE

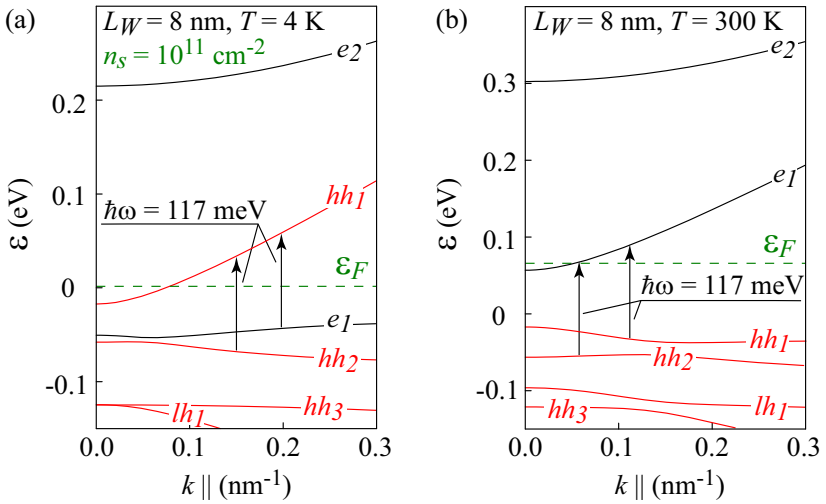

Figure 5.19: Calculated band structure for 8 nm QW at (a) $T = 4.2$ K and (b) $T = 300$ K. Arrows show optical transitions induced by mid-infrared radiation with photon energy of $\hbar\omega = 117$ meV.

T	5 nm	8 nm	12 nm	22 nm
4 K	e_1	hh_1	hh_1	hh_1
200 K	e_1	e_1	hh_1	hh_1

Table 5.1: Lowest conduction subband in dependence on QW width and temperature as calculated using the eight-band $\boldsymbol{k}\cdot\boldsymbol{p}$ model.

current is detected solely in structures with inverted band ordering where the lowest conduction subband is formed by p-type orbitals. Fixing the experimentally found mutual coherence of the band type and current behaviour, possible microscopic mechanisms of the nonlinear effect should be considered.

In the terahertz spectral range ($\hbar\omega = 3 \div 14$ meV), the radiation absorption is dominated by Drude-type processes in the lowest conduction subband (see Tab. 5.1). In this case, the photocurrent is mainly caused by asymmetry of the electron scattering by phonons and static defects in the magnetic field [29]. The scattering due to the diamagnetic terms is discussed in [61, 64] and up to now considered to be less probable as the spin-dependent emission of phonons leading to generation of the pure spin currents due to the spin-dependent asymmetry of the photoexcitation or/and hot electron relaxation. The electric current arises, hence, by means of their conversion owing to application of the magnetic field. The conversion current is for small fields proportional to the Zeeman splitting which is for QW structures with normal band ordering linear in the field strength (compare Sec. 5.1). However, in HgTe-based QWs with inverted band structure, the partially occupied ground conduction subband is formed from the Γ_8-band (hh_1) states (see Fig. 5.19(a)). In this case, the Zeeman splitting Δ_Z in the in-plane magnetic field depends strongly nonlinear on B [11, 109]. Since the conversion mechanism predicts $j(\boldsymbol{B}) \propto \Delta_Z(\boldsymbol{B})$, the photocurrent exhibits a nonlinear be-

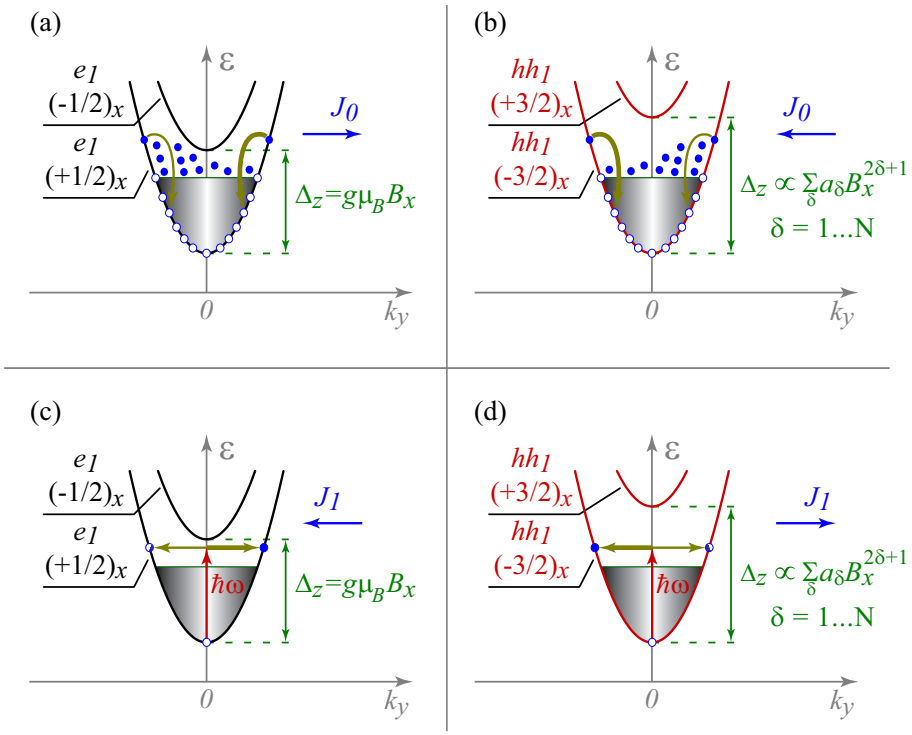

Figure 5.20: Mechanism of MGPGE current due to the magnetic-field-induced conversion of pure spin photocurrents. ((a)–(b)) Polarisation-independent current J_0 due to the spin-dependent asymmetry of energy relaxation in (a) electron- and (b) heavy-hole-like subbands. ((c)–(d)) Polarisation-dependent current J_1 due to the spin-dependent asymmetry of photoexcitation in (c) electron- and (d) heavy-hole-like subbands. While the Zeeman splitting in electron-type subbands is linear-in-B, in the heavy-hole-type subbands the magnetic field conversion occurs due to the odd-in-B contributions starting with B^3.

haviour in the applied magnetic field owing to nonlinear Zeeman effect. On the other hand, in the narrow QW with $L_W = 5$ nm and QW with $L_W = 8$ nm at high temperatures, the ground conduction subband is formed from the Γ_6-band (e_1) states (see Fig. 5.19(b)). Here, the Zeeman splitting is linear-in-B, and a noticeable cubic-in-B contribution to the photocurrent is absent as observed in the experiments. Figure 5.20 demonstrates the conversion of pure spin currents originating from the spin-dependent asymmetry of the hot electron relaxation in structures with (a) normal and (b) inverted band ordering leading to the polarisation-independent photocurrent J_0. The simultaneous observation of the polarisation-dependent current J_1 in the experiment can be attributed to the magnetic field conversion of the spin currents due to the asymmetry of the photoexcitation as shown in figures 5.20(c) and (d). The spin-dependent mechanism under free-carrier absorption may also be responsible for the photocurrent caused by mid-infrared radiation. Although the contribution from the Drude processes to the total absorption does not seem to be dominant in the spectral range where interband transitions are possible, it may nevertheless determine the photocurrent. This scenario is supported by the drastic spectral dependence of the photocurrents demonstrated in Fig. 5.17. Indeed, the photocurrent strength increases by more than one order of magnitude

with increasing wavelength, the dependence usually detected for Drude-like absorption [33]. The detection of the polarisation-dependent current J_1 in this spectral range is an additional support for this mechanism.

Summarizing the experimental results and band structure calculations, the MGPGE photocurrent in quantum wells with the inverted band sequence becomes strongly nonlinear. The most probable microscopic explanation is based on the nonlinear conversion of pure spin currents in an external magnetic field due to the nonlinear Zeeman splitting. From practical point of view, the method of the MGPGE can be utilised for the characterisation of the material band structure providing, for instance, a quick experimental check of topologically non-trivial state required for the quantum spin hall phase.

5.3 MGPGE in (013)-grown HgTe QWs

In the previous section, it has been demonstrated that the nonlinear behaviour of the MGPGE photocurrent is related to the inverted band ordering in nanostructures. In particular case of the (001)-grown HgTe-based QWs with the heavy-hole-like subband as the lowest conduction band, the photocurrent dependence upon in-plane external magnetic field has been considered as a sum of linear- and cubic-in-B contributions. In this context, narrow bandgap HgTe-based nanomaterials with even lower symmetry appear to be of an additional interest. Indeed, the decrease of the symmetry may enhance the nonlinear behaviour and provide an useful information towards understanding of the microscopical origin of the nonlinear photocurrent formation.

In the present section, a (013)-oriented HgTe/HgCdTe QW structure is studied. Media grown along such a specific direction belong to the C_1 point group which possesses only the identity as a symmetry operation and represents, therefore, the lowest possible structure symmetry. Since in the previous section the nonlinear behaviour has been detected only in structures with an inverted band ordering, a (013)-grown structure with a wide quantum well has been chosen. In this case, the inverted band ordering is present up to room temperature allowing to study the nonlinear MGPGE current in a wide temperature range.

5.3.1 Experimental results

The MGPGE photocurrents have been detected in the (013)-grown asymmetrical QW structure #10 with 21 nm width single quantum well under illumination with mid-infrared radiation in the range from liquid helium up to room temperature. Moreover, the observed currents depend on the orientation of the electric field vector of the incident light. However, in the following discussion, photocurrents as a function of an external magnetic field only at a fixed polarisation state of the radiation are concerned as these feature the structure under investigation. Similar to the previous section, all measurements have been carried out under normal incidence of light. Although such geometry does not exclude magnetic field independent photocurrents, however, influence of different mechanisms of the photocurrent formation arising in an oblique geometry may be minimised. Indeed, symmetry considerations for the present material allow even at normal incidence different

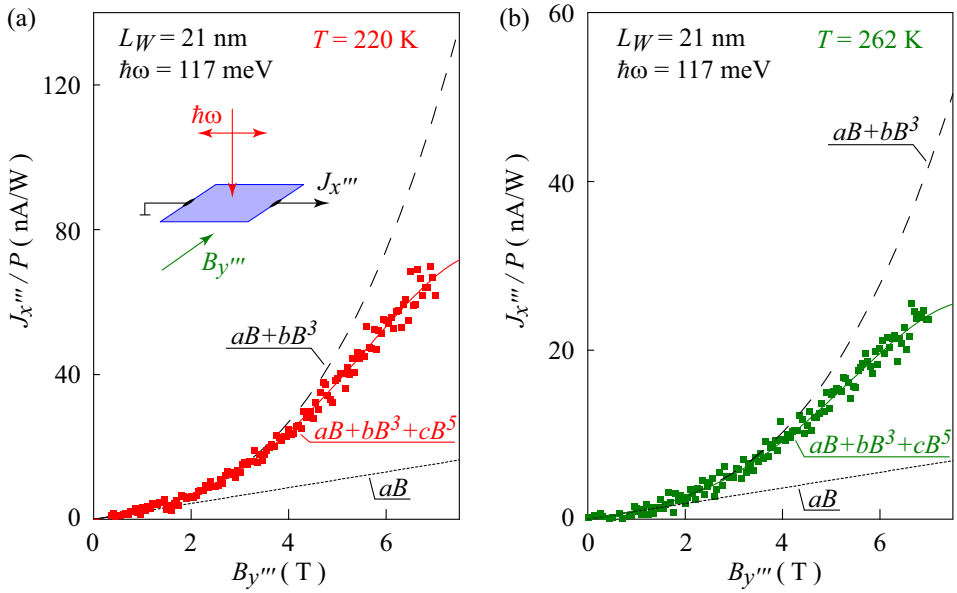

Figure 5.21: Magnetic field dependences of the MGPGE current $J_{x'''}$ at mid-infrared excitation with photon energy of $\hbar\omega = 117$ meV in (013)-oriented HgTe-based QW structure #10 with $L_W = 21$ nm at (a) $T = 220$ K and (b) $T = 262$ K. The solid lines are plotted according to Eq. (5.17). The doted and dashed lines demonstrate the linear-in-B current and the sum of linear- and cubic-in-B contributions, respectively. The inset shows the experimental geometry.

magnetic field dependent as well as independent current contributions. Therefore, all magnetic field dependences are evaluated after Eq. (5.1)

$$J^{MGPGE} = [J(B_+) - J(B_-)]/2\,,$$

allowing one to analyse the odd-in-B currents unaffected by another contributions. Illuminating samples at normal incidence, for the magnetic field $\boldsymbol{B}$ parallel to the interface plane a photocurrent signal in the perpendicular direction has been detected. It should be noted that generally in structures with C_1 symmetry the photocurrent flow direction is not bound and, hence, may rotate at an arbitrary angle in the plane of interface due to the variation of the wavelength and temperature as it has been observed in this sample studying the CPGE currents [47]. Here, the photocurrent projection on the axis perpendicular to the direction of the applied magnetic field has been measured. In the following, the magnetic field is denoted as $B_{y'''}$ and the current as $J_{x'''}$ building a right-handed system with the sample growth direction z'''. In figures 5.21(a) and (b) the MGPGE photocurrent is demonstrated as a function of an in-plane magnetic field at high temperatures of 220 K and 262 K, respectively. In both cases the current is strongly nonlinear and can be described by a superposition of linear-, cubic- *and* fifth-power-in-B terms:

$$J_{x'''}(B) = aB + bB^3 + cB^5\,. \tag{5.17}$$

While the linear- and cubic-in-B contributions a and b are positive, the fifth-order contribution c is negative. Reduction of the temperature reveals same general results. Figure 5.22 demonstrates the

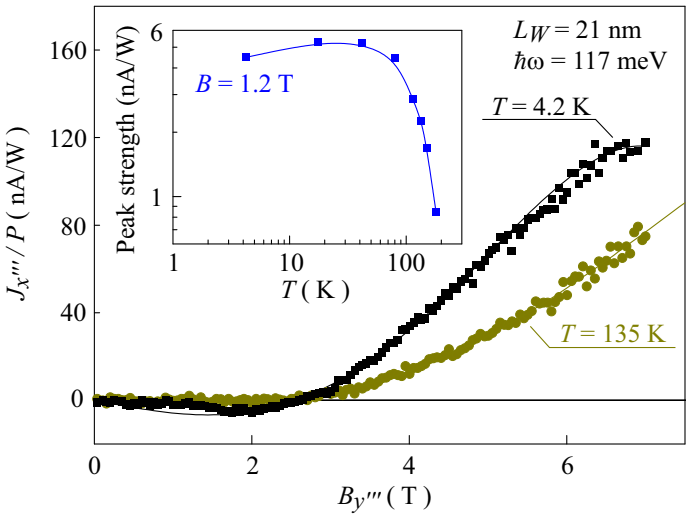

Figure 5.22: Magnetic field dependences of the MGPGE current $J_{x'''}$ obtained in the sample #10 at $T = 4.2$ K and $T = 135$ K. The data are fitted after Eq. (5.17). The observed peak at $B = 1.2$ T is shown in the inset as a temperature function of the amplitude.

current $J_{x'''}$ as a function of the field $B_{y'''}$ at 4.2 K and 135 K. Here, in contrast to the nonlinear contributions, the linear current inverts its flow direction along the x'''-axis.

Unexpected for the mid-infrared region is an observation of a resonant peak. It has a maximum at the magnetic field $B = 1.2$ T and a half-width of 1.1 T. The peak amplitude is of about 5 nA/W at 4.2 K and decays as a function of temperature as shown in the inset in Fig. 5.22. Up to now, the origin of the peak is not clear. The scenario of the resonant activation of the indium donor levels by the radiation with the photon energies about 120 meV is not very probable though.

Behaviour of the current components a, b and c in the range from liquid helium up to room temperature is demonstrated in the Fig. 5.23 whereas the full symbols represent the current inverted values. As it can be seen, all current contributions increase by one order of magnitude with the temperature decrease and scale in the same manner. However, while nonlinear contributions b and c hold their sign, the current a inverts its direction along x''' while passing the temperature of about 180 K. The conductance of the sample under day light as a function of temperature is shown by dashed line. It decreases by less than two times with the temperature. In order to check whether the conductance affects the current strength, the Hall geometry is considered. The characteristical SdH oscillations have been observed in the transport measurements and are shown by dash-doted line in the inset in Fig. 5.23. However, the odd-in-B current $J_{x'''}$ in the out-of-plane magnetic field $B_{z'''}$ (red line) has neither conductance proportionality nor any recognizable functional dependence.

5.3.2 Discussion and outlook

In the previous section, an observation of nonlinear MGPGE photocurrent in (001)-oriented QWs with heavy-hole-like subband in the ground conduction band has been reported and considered to be a sum of linear- and cubic-in-B current contributions. Detection of the nonlinear current

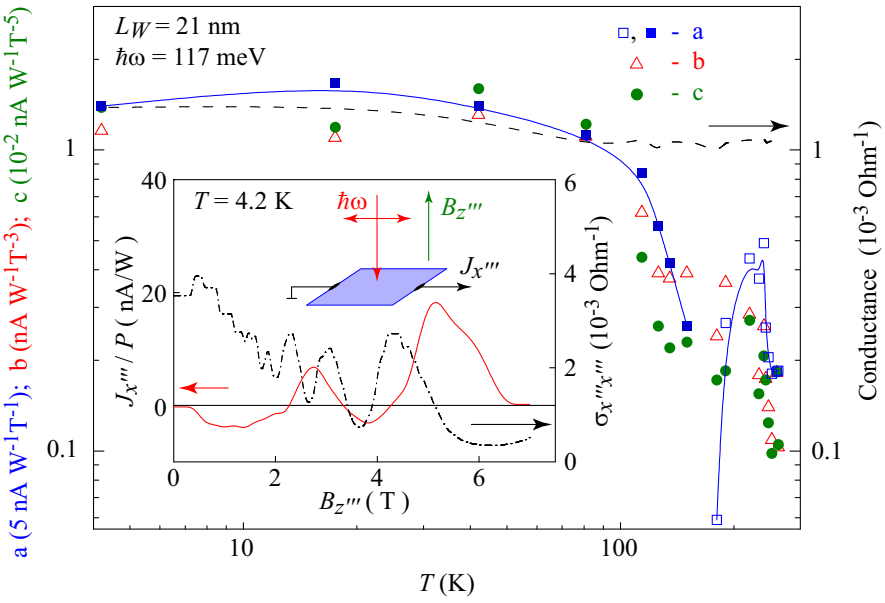

Figure 5.23: Temperature dependences of the absolute values of coefficients a, b and c (see Eq. (5.17)) obtained for the sample #10 at mid-infrared excitation in the in-plane magnetic field. Full symbols correspond to negative values of the coefficients. Dashed line shows the conductance at day light conditions. The inset demonstrates the magnetic field dependences of the MGPGE current $J_{x'''}$ (red line) and conductance $\sigma_{x'''x'''}$ (dash-doted line) in the out-of-plane field.

in (013)-grown QWs is in a fully agreement with the inverted band ordering in these structures present at all temperatures. Although the current strength is comparable to that observed in (001)-grown structures, in (013)-oriented material the next order of the odd-in-B current contribution has been detected. Probably the reduction of the symmetry down to the C_1 point group enhances the nonlinear behaviour in materials with inverted band sequence. Although the new fifth-order-in-B contribution was found to be very small, at high fields, however, it already codetermines the total photocurrent which tends, hence, to decline at magnetic fields above 7 T. Generally speaking, the presence of the nonlinearity does not allow to exclude the higher orders of the odd-in-B MGPGE current contributions.

It should be noted that in media of C_1 symmetry, photocurrents may flow in any arbitrary direction in the interface plane. Studies of the CPGE currents in (013)-grown QW structures have revealed that the helicity-dependent currents rotate in the QW plane upon variation of temperature as well as photon energies of the radiation [47] which is in agreement with the phenomenological theory. As a matter of fact, the MGPGE currents considered here may flow in any direction in the QW plane as well. Therefore, experimentally measured photocurrents in x''' direction represent only the projection of the total photocurrent on this axis. The temperature dependence of the linear-in-B MGPGE current projection is demonstrated in Fig. 5.23 which is characterised by a coefficient a in the Eq. (5.17). This current is positive at high temperatures and changes its sign

about 180 K. Additional temperature measurements of the current in the orthogonal y''' direction would give a definite answer whether the linear current performs a flip or a kind of rotation in the QW plane. Important result is a uniform behaviour of both nonlinear contributions upon temperature variation. The cubic- and the fifth-order-in-B MGPGE current projections given by coefficients b and c in Eq. (5.17) are of opposite signs and increase by one order of magnitude while temperature decreases from the room down to the liquid helium temperature as shown by red and green symbols in Fig. 5.23, respectively. Similar temperature dependences and, moreover, opposite signs of both nonlinear current projections support an assumption of the same microscopic origin of the both nonlinear photocurrents. Indeed, the sign of the nonlinear currents is expected to alternate with every successive order of the odd-in-B function. One of the probable mechanisms of the current formation is the nonlinear conversion of pure spin currents due to the nonlinear Zeeman spin splitting of the heavy-hole-type subband $\Delta_{\mathrm{Z}}(\boldsymbol{B}) \propto \Sigma a_\delta B_{y'''}^{2\delta+1}$ (see figures 5.19(b) and (d)) where $\mathrm{sign}(a_\delta) = -\mathrm{sign}(a_{\delta+1})$ and $\delta = 1...N$. However, other spin-dependent as well as diamagnetic origins can not be excluded. Moreover, a set of microscopic mechanisms contributing to the total current must be expected as far the linear and nonlinear current components exhibit different behaviour upon temperature variation.

Chapter 6

Conclusion

In terms of the present work, the experimental method of photoinduced currents has been exploited as it provides an access to the spin and orbital properties of electrons and holes in nanostructures. The conducted measurements in GaAs-based QW structures have revealed a number of new photogalvanic phenomena. Among them is a novel helicity-dependent current, circular photon drag effect, which has been observed in (110)-grown QWs under intersubband absorption of circularly polarised light. The developed microscopic model is related to the spin-dependent processes and bases on the optical spin orientation and the subsequent asymmetric spin-flip relaxation. While the last stage is the spin-galvanic effect where a non-equilibrium spin drives a charge current, in first two steps a specific kind of the magneto-optical spin injection occurs. It is caused by simultaneous transfer of the photon linear and angular momenta to the carriers and the subsequent spin rotation in the effective magnetic field due to the linear spin-orbit coupling terms arising in gyrotropic structures with spin-orbit interaction.

Investigations of photocurrents in (001)-oriented QWs exposed to external magnetic field have revealed a new magneto-induced current under intersubband absorption of light. It has been demonstrated that the observed effect is related to the gyrotropic feature of the material. Analysing the experimental data and taking into account the theoretical estimations, the most probable microscopic explanation of the detected magneto-gyrotropic photocurrent under intersubband resonance is the diamagnetic mechanism based on the asymmetric phonon emission by resonantly excited electrons in the upper conduction subband.

Expecting a strong enhancement of spin-dependent effects in narrow bandgap materials, magneto-gyrotropic photogalvanic experiments in HgTe-based QWs with both normal and inverted band ordering have been performed. Here, considerable photoresponses have been detected which are by two orders of magnitude stronger than those obtained in GaAs samples in the same excitation range. Moreover, an exciting result is a discovery of a nonlinear magneto-gyrotropic photocurrent which is shown to cohere with the type of the lowest conduction band. While in wide wells with the heavy-hole-like subband the current is strongly nonlinear, in narrow wells with usual band sequence the effect scales linearly with the applied field. Microscopically, observation of spectral and polarisation dependences in (001)-oriented QWs support the model of zero-bias spin separation in both mid-infrared and terahertz excitation regions due to spin-dependent asymmetry of

Drude-type photoexcitation and hot electron relaxation processes. In the second step, application of the magnetic field converts the pure spin currents into electric current due to the Zeeman effect which is either linear or nonlinear in dependence whether the subband is of electron- or heavy-hole-type. Investigating the inverted band ordering regime in (013)-grown structures, the detection of two nonlinear components of opposite sign endorses the already mentioned mechanism since the nonlinear Zeeman splitting can be developed in series of odd contributions with alternating signs.

An important result has been obtained regarding the intersubband absorption of the radiation. Experimental studies of the photogalvanic effects under intersubband resonance of the normally incident light in GaAs-based QWs have demonstrated that the usually applied selection rules are not rigorous. Although the resonant transitions between the first and second subbands in QWs are forbidden for the light with the polarisation vector parallel to the QW plane by dipole selection rules, the admixture of valence to conduction band in the framework of the Kane model may, however, soften them. Measurements of the magneto-gyrotropic photocurrents in (001)-oriented structures under normal and oblique incidence have revealed that the normal incidence absorbance is nonzero and as large as 2 % of the absorbance of light polarised out of the QW plane. Studying magneto-induced currents in HgTe-based structures at low temperatures, resonant drops in the current magnitude in the magnetic field functions have been observed. Under terahertz excitation, the field position of the drop scales linearly with the photon energy. The favourable explanation is the ionisation of partially occupied shallow impurity states.

References

[1] E.L. Wolf, *Nanophysics and Nanotechnology. An Introduction to Modern Concepts in Nanoscience* (Wiley-VCH, 2006).

[2] S.M. Sze, *Semiconductor Devices. Physics and Technology* (Wiley, 2002).

[3] M.J. Kelly, *Low-Dimensional Semiconductors* (Oxford Univ. Press, 1995).

[4] G.E. Moore, *Cramming more components onto integrated circuits*, Electronics **38**, 114-117 (1965).

[5] N.A. Gershenfeld and I.L. Chuang, *Bulk Spin-Resonance Quantum Computation*, Science **275**, 350 (1997).

[6] M.A. Nielsen and I.L. Chuang, *Quantum Computation and Quantum Information* (Cambridge Univ. Press, 2000).

[7] S. Maekawa, ed., *Concepts in Spin Electronics*, in Series on Semiconductor Science and Technology, eds. R.J. Nicholas and H. Kamimura (Oxford Univ. Press, 2006).

[8] D.D. Awschalom, D. Loss, and N. Samarth, eds., *Semiconductor Spintronics and Quantum Computation*, in Nanoscience and Technology, eds. P. Avouris, K. von Klitzing, H. Sakaki, and R. Wiesendanger (Springer, 2002).

[9] E. Hirota, H. Sakakima, and K. Inomata, *Giant Magneto-Resistance Devices* (Springer, 2002).

[10] S.D. Ganichev and W. Prettl, *Spin photocurrents in quantum wells*, J. Phys.: Condens. Matter **15**, R935-R983 (2003).

[11] R. Winkler, *Spin-Orbit Coupling Effects in Two-Dimensional Electron and Hole Systems*, in Springer Tracts in Modern Physics, Vol.191 (Springer, 2003).

[12] M.I. D'yakonov and V.I. Perel', *Spin orientation of electrons associated with the interband absorption of light in semiconductors*, Zh. Eksp. Teor. Fiz. **60**, 1954 (1971) [Sov. JETP **33**, 1053 (1971)].

[13] M.I. D'yakonov and V.I. Perel', *Spin relaxation of conduction electrons in noncentrosymmetric semiconductors*, Fiz. Tverd. Tela **13**, 3581 (1971) [Sov. Phys. Solid State **13**, 3023 (1972)].

[14] M.I. D'yakonov and V.Yu. Kachorovskii, *Spin relaxation of two-dimensional electrons in noncentrosymmetric semiconductors*, Fiz. Tekh. Poluprovodn. **20**, 178 (1986) [Sov. Phys. Semicond. **20**, 110 (1986)].

[15] N.S. Averkiev and M.I. Dyakonov, *Feasibility of optical orientation of equilibrium electrons in semiconductors*, Pis'ma Zh. Eksp. Teor. Fiz. **13**, 206 (1971) [Sov. JETP Lett. **13**, 144 (1971)].

[16] N.S. Averkiev and M.I. Dyakonov, *Current due to inhomogenity of the spin orientation of electrons in a semiconductor*, Fiz. Tekh. Poluprovodn. **17**, 629 (1983) [Sov. Phys. Semicond. **17**, 393 (1983)].

[17] A.A. Bakun, B.P. Zakharchenya, A.A. Rogachev, M.N. Tkachuk, and V.G. Fleisher, *Observation of a surface photocurrent caused by optical orientation of electrons in a semiconductor*, Pis'ma Zh. Eksp. Teor. Fiz. **40**, 464 (1984) [Sov. JETP Lett. **40**, 1293 (1984)].

[18] M.I. Dyakonov, ed., *Spin Physics in Semiconductors*, in Springer Series in Solid State Sciences, eds. M. Cardona, P. Fulde, K. von Klitzing, H.-J. Queisser, R. Merlin, and H. Störmer (Springer, 2008).

[19] S.D. Ganichev, E.L. Ivchenko, V.V. Bel'kov, S.A. Tarasenko, M. Sollinger, D. Weiss, W. Wegscheider, and W. Prettl, *Spin-Galvanic Effect*, Nature **417**, 153 (2002).

[20] S.D. Ganichev, V.V. Bel'kov, S.A. Tarasenko, S.N. Danilov, S. Giglberger, C. Hoffmann, E.L. Ivchenko, D. Weiss, W. Wegscheider, C. Gerl, D. Schuh, J. Stahl, J. De Boeck, G. Borghs, and W. Prettl, *Zero-bias spin separation*, Nature Physics **2**, 609 (2006).

[21] S.D. Ganichev, E.L. Ivchenko, S.N. Danilov, J. Eroms, W. Wegscheider, D. Weiss, and W. Prettl, *Conversion of Spin into Directed Electric Current in Quantum Wells*, Phys. Rev. Lett. **86**, 4358 (2001).

[22] M. Bieler, N. Laman, H.M. van Driel, and A.L. Smirl, *Ultrafast spin-polarized electrical currents injected in a strained zinc blende semiconductor by single color pulses*, Appl. Phys. Lett. **86**, 061102 (2005).

[23] C.L. Yang, H.T. He, Lu Ding, L.J. Cui, Y.P. Zeng, J.N. Wang, and W.K. Ge, *Spectral Dependence of Spin Photocurrent and Current-Induced Spin Polarization in an InGaAs/InAlAs Two-Dimensional Electron Gas*, Phys. Rev. Lett. **96**, 186605 (2006).

[24] M. König, S. Wiedmann, C. Brüne, A. Roth, H. Buhmann, L.W. Molenkamp, X.-L. Qi, and S.-C. Zhang, *Quantum Spin Hall Insulator State in HgTe Quantum Wells*, Science **318**, 766 (2007).

[25] M. König, H. Buhmann, L.W. Molenkamp, T. Hughes, C.-X. Liu, X.-L. Qi, and S.-C. Zhang, *The Quantum Spin Hall Effect: Theory and Experiment*, J. Phys. Soc. Jpn. **77**, 031007 (2008).

[26] S.A. Tarasenko, *Orbital mechanism of circular photogalvanic effect in quantum wells*, JETP Lett. **85**, 182 (2007).

[27] P. Olbrich, S.A. Tarasenko, C. Reitmaier, J. Karch, D. Plohmann, Z.D. Kvon, and S.D. Ganichev, *Observation of the orbital circular photogalvanic effect*, Phys. Rev. B **79**, 121302 (2009).

[28] V.V. Bel'kov, S.D. Ganichev, E.L. Ivchenko, S.A. Tarasenko, W. Weber, S. Giglberger, M. Olteanu, H.-P. Tranitz, S.N. Danilov, Petra Schneider, W. Wegscheider, D. Weiss, and W. Prettl, *Magneto-gyrotropic photogalvanic effects in semiconductor quantum wells*, J. Phys.: Condens. Matter **17**, 3405-3428 (2005).

[29] V.V. Bel'kov and S.D. Ganichev, *Magneto-gyrotropic effects in semiconductor quantum wells*, Semicond. Sci. Technol. **23**, 114003 (2008).

[30] S.D. Ganichev, W. Weber, J. Kiermaier, S.N. Danilov, P. Olbrich, D. Schuh, W. Wegscheider, D. Bougeard, G. Abstreiter, and W. Prettl, *All-electric detection of the polarization state of terahertz laser radiation*, J. Appl. Phys. **103**, 114504 (2008).

[31] S.N. Danilov, B. Wittmann, P. Olbrich, W. Eder, W. Prettl, L.E. Golub, E.V. Beregulin, Z.D. Kvon, N.N. Mikhailov, S.A. Dvoretsky, V.A. Shalygin, N.Q. Vinh, A.F.G. van der Meer, B. Murdin, and S.D. Ganichev, *Fast detector of the ellipticity of infrared and terahertz radiation based on HgTe quantum well structures*, J. Appl. Phys. **105**, 013106 (2009).

[32] E.L. Ivchenko, *Optical Spectroscopy of Semiconductor Nanostructures* (Alpha Science International, 2005).

[33] S.D. Ganichev and W. Prettl, *Intense Terahertz Excitation of Semiconductors*, in Series on Semiconductor Science and Technology, eds. R.J. Nicholas and H. Kamimura (Oxford Univ. Press, 2006).

[34] E.L. Ivchenko, Yu.B. Lyanda–Geller, and G.E. Pikus, *Photocurrent in structures with quantum wells with an optical orientation of free carriers*, Pis'ma Zh. Eksp. Teor. Fiz. **50**, 156 (1989) [JETP Lett. **50**, 175 (1989)].

[35] G. Dresselhaus, *Spit-Orbit Coupling Effects in Zinc Blende Structures*, Phys. Rev. **100**, 580, (1955).

[36] Y.A. Bychkov and E.I. Rashba, *Properties of a 2D electron gas with lifted spectral degeneracy*, Pis'ma Zh. Eksp. Teor. Fiz. **39**, 66 (1984) [Sov. JETP Lett. **39**, 78 (1984)].

[37] E.A. de Andrada e Silva, *Conduction-subband anisotropic spin splitting in III-V semiconductor heterojunctions*, Phys. Rev. B **46**, 1921 (1992).

[38] N.S. Averkiev, L.E. Golub, and M. Willander, *Spin relaxation anisotropy in two-dimensional semiconductor systems*, J. Phys.: Condens. Matter **14**, 271 (2002).

[39] G.E. Pikus and A.N. Titkov, *Spin Relaxation under Optical Orientation in Semiconductors*, in *Optical Orientation*, eds. F. Meier and B.P. Zakharchenya (Elsevier Science Publishers, 1984).

[40] Y. Ohno, R. Terauchi, T. Adachi, F. Matsukura, and H. Ohno, *Spin Relaxation in GaAs*(110) *Quantum Wells*, Phys. Rev. Lett. **83**, 4196 (1999).

[41] E.L. Ivchenko and G.E. Pikus, *New photogalvanic effects in gyrotropic crystalls*, Pis'ma Zh. Eksp. Teor. Fiz. **27**, 640 (1978) [JETP Lett. **27**, 604 (1978)].

[42] V.I. Belinicher, *Space-oscillating photocurrent in crystals without symmetry center*, Phys. Lett. A **66**, 213 (1987).

[43] V.M. Asnin, A.A. Bakun, A.M. Danishevskii, E.L. Ivchenko, G.E. Pikus, and A.A. Rogachev, *Observation of a photo-emf that depends on the sign of the circular polarization of the light*, Pis'ma Zh. Eksp. Teor. Fiz. **28**, 80 (1978) [JETP Lett. **28**, 74 (1978)].

[44] S.D. Ganichev, H. Ketterl, W. Prettl, E.L. Ivchenko, and L.E. Vorobjev, *Circular photogalvanic effect induced by monopolar spin orientation in p-GaAs/AlGaAs multiple-quantum wells*, Appl. Phys. Lett. **77**, 3146 (2000).

[45] S.D. Ganichev, V.V. Bel'kov, Petra Schneider, E.L. Ivchenko, S.A. Tarasenko, D. Schuh, W. Wegscheider, D. Weiss, and W. Prettl, *Resonant inversion of circular photogalvanic effect in n-doped quantum wells*, Phys. Rev. B **68**, 035319 (2003).

[46] S.D. Ganichev, U. Rössler, W. Prettl, E.L. Ivchenko, V.V. Bel'kov, R. Neumann, K. Brunner, and G. Abstreiter, *Removal of spin degeneracy in p-SiGe quantum wells demonstrated by spin photocurrents*, Phys. Rev. B **66**, 075328 (2002).

[47] B. Wittmann, S.N. Danilov, Z.D. Kvon, N.N. Mikhailov, S.A. Dvoretsky, R. Ravash, W. Prettl, and S.D. Ganichev, *Photogalvanic effects in HgTe quantum wells*, Proc. 13th Int. Conf. on Narrow Gap Semiconductors (NGS-13), Guildford, UK (2007).

[48] W. Weber, S.D. Ganichev, S.N. Danilov, D. Weiss, W. Prettl, Z.D. Kvon, V.V. Bel'kov, L.E. Golub, Hyun-Ick Cho, and Jung-Hee Lee, *Demosntration of Rashba spin splitting in GaN-based heterostructures*, Appl. Phys. Lett. **87**, 262106 (2005).

[49] K.S. Cho, C.-T. Liang, Y.F. Chen, Y.Q. Tang, and B. Shen, *Spin-dependent photocurrent induced by Rashba-type spin splitting in* $Al_{0.25}Ga_{0.75}N/GaN$ *heterostructures*, Phys. Rev. B **75**, 085327 (2007).

[50] S. Giglberger, L.E. Golub, V.V. Bel'kov, S.N. Danilov, D. Schuh, C. Gerl, F. Rohlfing, J. Stahl, W. Wegscheider, D. Weiss, W. Prettl, and S.D. Ganichev, *Rashba and Dresselhaus spin splittings in semiconductor quantum wells measured by spin photocurrents*, Phys. Rev. B **75**, 035327 (2007).

[51] R.L. Liboff, *Primer for point and space groups* (Springer, 2004).

[52] E.L. Ivchenko and S.A. Tarasenko, *Monopolar Optical Orientation of Electron Spins in Bulk Semiconductors and Heterostructures*, Zh. Eksp. Teor. Fiz. **126**, 426 (2004) [JETP **99**, 379 (2004)].

[53] T. Ando, A.B. Fowler, and F. Stern, *Electronic properties of two-dimensional systems*, Rev. Mod. Phys. **54**, 437 (1982).

[54] R.J. Warburton, C. Gauer, A. Wixforth, J.P. Kotthaus, B. Brar, and H. Kroemer, *Intersubband resonances in InAs/AlSb quantum wells: Selection rules, matrix elements, and the depolarization field*, Phys. Rev. B **53**, 7903 (1996).

[55] H.C. Liu, M. Buchanan, and Z.R. Wasilewski, *How good is the polarization selection rule for intersubband transitions?*, Appl. Phys. Lett. **72**, 1682 (1998).

[56] L.E. Golub, *New Mechanism of the Spin-Galvanic Effect*, Pis'ma Zh. Eksp. Teor. Fiz. **85**, 479 (2007) [JETP Lett. **85**, 393 (2007)].

[57] Discussion with S.A. Tarasenko.

[58] A.V. Andrianov and I.D. Yaroshetskii, *Magnetic-field-induced circular photovoltaic effect in semiconductors*, Pis'ma Zh. Eksp. Teor. Fiz. **40**, 131 (1984) [JETP Lett. **40**, 882 (1984)].

[59] V.V. Bel'kov, P. Olbrich, S.A. Tarasenko, D. Schuh, W. Wegscheider, T. Korn, C. Schüller, D. Weiss, W. Prettl, and S.D. Ganichev, *Symmetry and Spin Dephasing in* (110)*-Grown Quantum Wells*, Phys. Rev. Lett. **100**, 176806 (2008).

[60] V. Lechner, L.E. Golub, P. Olbrich, S. Stachel, D. Schuh, W. Wegscheider, V.V. Bel'kov, and S.D. Ganichev, *Tuning of structure inversion asymmetry by the δ-doping position in* (001)*-grown GaAs quantum wells*, Appl. Phys. Lett. **94**, 242109 (2009).

[61] S.A. Tarasenko, *Electron scattering in quantum wells subjected to an in-plane magnetic field*, Phys. Rev. B **77**, 085328 (2008).

[62] H. Diehl, V.A. Shalygin, S.N. Danilov, S.A. Tarasenko, V.V. Bel'kov, D. Schuh, W. Wegscheider, W. Prettl, and S.D. Ganichev, *Magneto-gyrotropic photogalvanic effects due to intersubband absorption in quantum wells*, J. Phys.: Condens. Matter **19**, 436232 (2007).

[63] A.A. Gorbatsevich, V.V. Kapaev, and Yu.V. Kopaev, *Asymmetric nanostructures in a magnetic field*, Pis'ma Zh. Eksp. Teor. Fiz. **57**, 565 (1993) [JETP Lett. **57**, 580 (1993)].

[64] O.V. Kibis, *Anisotropic momentum transfer in low-dimensional electron systems in a magnetic field*, Pis'ma Zh. Eksp. Teor. Fiz. **66**, 551 (1997) [JETP Lett. **66**, 588 (1997)].

[65] Yu.A. Aleshchenko, I.D. Voronova, S.P. Grishechkina, V.V. Kapaev, Yu.V. Kopaev, I.V. Kucherenko, V.I. Kadushkin, and S.I. Fomichev, *Magnetic-field-induced photovoltaic effect in an asymmetric system of quantum wells*, Pis'ma Zh. Eksp. Teor. Fiz. **58**, 377 (1993) [JETP Lett. **58**, 384 (1993)].

[66] I.V. Kucherenko, L.K. Vodop'yanov, and V.I. Kadushkin, *Photovoltaic effect in an asymmetric GaAs/AlGaAs nanostructure produced as a result of laser excitation*, Fiz. Tekh. Poluprovodn. **31**, 872 (1997) [Semiconductors **31**, 740 (1997)].

[67] S.A. Tarasenko and E.L. Ivchenko, *Pure spin photocurrents in low-dimensional structures*, Pis'ma Zh. Eksp. Teor. Fiz. **81**, 292 (2005) [JETP Lett. **81**, 231 (2005)].

[68] S.D. Ganichev, S.N. Danilov, V.V. Bel'kov, S. Giglberger, S.A. Tarasenko, E.L. Ivchenko, D. Weiss, W. Jantsch, F. Schäffler, D. Gruber, and W. Prettl, *Pure spin currents induced by spin-dependent scattering processes in SiGe quantum well structures*, Phys. Rev. B **75**, 155317 (2007).

[69] S.D. Ganichev, S.A. Tarasenko, V.V. Bel'kov, P. Olbrich, W. Eder, D.R. Yakovlev, V. Kolkovsky, W. Zaleszczyk, G. Karczewski, T. Wojtowicz, and D. Weiss, *Spin Currents in Diluted Magnetic Semiconductors*, Phys. Rev. Lett. **102**, 156602 (2009).

[70] Y.K. Kato, R.C. Myers, A.C. Gossard, and D.D. Awschalom, *Observation of the spin Hall effect in semiconductors*, Science **306**, 1910 (2004).

[71] D.E. Aspnes, *GaAs lower conduction-band minima: Ordering and band properties*, Phys. Rev. B **14**, 5331 (1976).

[72] Y.P. Varshni, *Temperature dependence of the energy gap in semiconductors*, Physica **34**, 149 (1967).

[73] F. Möglich and R. Rompe, *Über den Einfluß der Wärmedehnung auf das Absorptionsspektrum von Isolatoren*, Zeitschrift für Physik **119**, 472 (1942).

[74] L.D. Landau and E.M. Lifshitz, *Quantum Mechanics: Non-Relativistic Theory* (Pergamon Press, 1977).

[75] F. Szmulowicz, M.O. Manasreh, C.E. Stutz, and T. Vaughan, *Temperature and many-body effects on the intersubband transition in a $GaAs/Al_{0.30.7}As$ multiple quantum well*, Phys. Rev. B **50**, 11618 (1994).

[76] J.P. Laurenti, J. Camassel, A. Bouhemadou, B. Toulouse, R. Legros, and A. Lusson, *Temperature dependence of the fundamental absorption edge of mercury cadmium telluride*, J. Appl. Phys **67**, 6454 (1990).

[77] Discussion with C. Brüne.

[78] Z.D. Kvon, S.N. Danilov, S.D. Ganichev, N.N. Mikhailov, and S.A. Dvoretsky, *Cyclotron resonance in a two-dimensional semimetal*, 14th Int. Conf. on Narrow Gap Semiconductors and Systems (NGS^2-14), Sendai, Japan (2009).

[79] E.G. Novik, A. Pfeuffer-Jeschke, T. Jungwirth, V. Latussek, C.R. Becker, G. Landwehr, H. Buhmann, and L.W. Molenkamp, *Band structure of semimagnetic $Hg_{1-y}Mn_yTe$ quantum wells*, Phys. Rev. B **72**, 035321 (2005).

[80] H. Diehl, V.A. Shalygin, L.E. Golub, S.A. Tarasenko, S.N. Danilov, V.V. Bel'kov, E.G. Novik, H. Buhmann, C. Brüne, L.W. Molenkamp, E.L. Ivchenko, and S.D. Ganichev, *Nonlinear magnetogyrotropic photogalvanic effect*, Phys. Rev. B **80**, 075311 (2009).

[81] O. Svelto, *Principles of Lasers* (Plenum Press, 1998).

[82] S.D. Ganichev, W. Prettl, and I.N. Yassievich, *Deep impurity-center ionization by far-infrared radiation*, Fiz. Tverd. Tela **39**, 1905 (1997) [Phys. Solid State **39**, 1703 (1997)].

[83] T. Adachi, Y. Ohno, F. Matsukura, and H. Ohno, *Spin relaxation in n-modulated doped GaAs/AlGaAs*(110) *quantum wells*, Physica E **10**, 36-39 (2001).

[84] O.Z. Karimov, G.H. John, R.T. Harley, W.H. Lau, M.E. Flatté, M. Henini, and R. Airey, *High Temperature Gate Control of Quantum Well Spin Memory*, Phys. Rev. Lett. **24**, 246601 (2003).

[85] E.L. Ivchenko and G.E. Pikus, *Photogalvanic Effects in Semiconductors*, in *Problems of Modern Physics, Collected Papers in Commemoration of the 100th Anniversary of the Birth of A.F. Ioffe*, eds. V.M. Tuchkevich and V.Ya. Frenkel (Nauka, 1980) [*Photogalvanic Effects in Noncentrosymmetric Crystals*, in *Semiconductor Physics*, eds. V.M. Tuchkevich and V.Ya. Frenkel (Cons. Bureau, 1986)].

[86] V.I. Belinicher, *On the mechanisms underlying the circular drag effect*, Fiz. Tverd. Tela **23**, 3461 (1981) [Sov. Phys. Solid State **23**, 2012 (1981)].

[87] H. Diehl, V.A. Shalygin, V.V. Bel'kov, Ch. Hoffmann, S.N. Danilov, T. Herrle, S.A. Tarasenko, D. Schuh, C. Gerl, W. Wegscheider, W. Prettl, and S.D. Ganichev, *Spin photocurrents in* (110)*-grown quantum well structures*, New J. Phys. **9**, 349 (2007).

[88] E. Hecht, *Optics*, pp. 72-75 (Addison-Wesley, 1974).

[89] S.D. Ganichev, Petra Schneider, V.V. Bel'kov, E.L. Ivchenko, S.A. Tarasenko, W. Wegscheider, D. Weiss, D. Schuh, B.N. Murdin, P.J. Phillips, C.R. Pidgeon, D.G. Clarke, M. Merrick, P. Murzyn, E.V. Beregulin, and W. Prettl, *Spin-galvanic effect due to optical spin orientation in n-type GaAs quantum well structures*, Phys. Rev. B **68**, 081302 (2003).

[90] V.A. Shalygin, H. Diehl, Ch. Hoffmann, S.N. Danilov, T. Herrle, S.A. Tarasenko, D. Schuh, C. Gerl, W. Wegscheider, W. Prettl, and S.D. Ganichev, *Spin Photocurrents and the Circular Photon Drag Effect in* (110)*-Grown Quantum Well Structures*, Pis'ma Zh. Eksp. Teor. Fiz. **84**, 666 (2006) [JETP Lett. **84**, 570 (2006)].

[91] S. Tsujino, M. Rüfenacht, H. Nakajima, T. Noda, C. Metzner, and H. Sakaki, *Peak position of the intersubband absorption spectrum of quantum wells with controlled electron concentrations*, Phys. Rev. B **62**, 1560 (2000).

[92] M. Born and E. Wolf, *Principles of Optics*, pp. 840-843 (Cambridge Univ. Press, 1999).

[93] L.I. Magarill, *Photogalvanic effect in a two-dimensional system subjected to a parallel magnetic field*, Fiz. Tverd. Tela **32**, 3558 (1990) [Sov. Phys. Solid State **32**, 2064 (1990)].

[94] A.P. Dmitriev, S.A. Emel'yanov, S.V. Ivanov, P.S. Kop'ev, Ya.V. Terent'ev, and I.D. Yaroshetskii, *Giant photocurrent in 2D structures in a magnetic field parallel to the 2D layer*, Pis'ma Zh. Eksp. Teor. Fiz. **54**, 279 (1991) [JETP Lett. **54**, 273 (1991)].

[95] S.A. Emel'yanov, Ya.V. Terent'ev, A.P. Dmitriev, and B.Ya. Mel'tser, *Electron spin resonance in GaSb–InAs–GaSb semimetal quantum wells*, Pis'ma Zh. Eksp. Teor. Fiz. **68**, 768 (1998) [JETP Lett. **68**, 810 (1998)].

[96] O.V. Kibis, *New quantum electron transport phenomena in low-dimensional systems in a magnetic field*, Phys. Lett. A **244**, 432 (1998).

[97] A.G. Pogosov, M.V. Budantsev, O.V. Kibis, A. Pouydebasque, D.K. Maude, and J.C. Portal, *Thermomagnetic effect in a two-dimensional electron gas with an asymmetric quantizing potential*, Phys. Rev. B **61**, 15603 (2000).

[98] E.L. Ivchenko and A.A. Kiselev, *Electron g factor of quantum wells and superlattices*, Fiz. Tekh. Poluprovodn. **26**, 1471 (1992) [Sov. Phys. Semicond. **26**, 827 (1992)].

[99] R.M. Hannak, M. Oestreich, A.P. Heberle, W.W. Rühle, and K. Köhler, *Electron g factor in quantum wells determined by spin quantum beats*, Sol. State Comm. **93**, 313 (1995).

[100] P. Le Jeune, D. Robart, X. Marie, T. Amand, M. Brousseau, J. Barrau, V. Kalevich, and D. Rodichev, *Anisotropy of the electron Landé g factor in quantum wells*, Semicond. Sci. Technol. **12**, 380 (1997).

[101] Y.S. Gui, C.R. Becker, N. Dai, J. Liu, Z.J. Qiu, E.G. Novik, M. Schäfer, X.Z. Shu, J.H. Chu, H. Buhmann, and L.W. Molenkamp, *Giant spin-orbit splitting in a HgTe quantum well*, Phys. Rev. B **70**, 115328 (2004).

[102] J. Hinz, H. Buhmann, M. Schäfer, V. Hock, C.R. Becker, and L.W. Molenkamp, *Gate control of the giant Rashba effect in HgTe quantum wells*, Semicond. Sci. Technol. **21**, 501 (2006).

[103] M. von Truchsess, V. Latussek, C.R. Becker, and E. Batke, *Landau-split and spin-split cyclotron resonance of two-dimensional electron systems in HgTe quantum wells*, J. Cryst. Growth **159**, 1104 (1996).

[104] I.D. Yaroshetskii and S.M. Ryvkin, *The Photon Drag of Electrons in Semiconductors*, in *Problems of Modern Physics, Collected Papers in Commemoration of the 100th Anniversary of the Birth of A.F. Ioffe*, eds. V.M. Tuchkevich and V.Ya. Frenkel (Nauka, 1980) [*The Photon Drag of Electrons in Semiconductors*, in *Semiconductor Physics*, eds. V.M. Tuchkevich and V.Ya. Frenkel (Cons. Bureau, 1986)].

[105] A.F. Gibson and M.F. Kimmit, *Photon Drag Detection*, in Infrared and Millimeter Waves, Vol. 3, Detection of Radiation, ed. K.J. Button (Academic Press, 1980).

[106] R.A. Stradling, L. Eaves, R.A. Hoult, N. Miura, P.E. Simmonds, and C.C. Bradley, *Zeeman spectroscopy of the shallow donor states in GaAs and InP*, in Symp. on GaAs (1972).

[107] M.G. Burt, *Fundamentals of envelope function theory for electronic states and photonic modes in nanostructures*, J. Phys.: Condens. Matter **11**, R53 (1999).

[108] M. von Truchsess, A. Pfeuffer-Jeschke, V. Latussek, C.R. Becker, and E. Batke, *Spectroscopy of interface states in HgTe/$Hg_{1-x}Cd_xTe$ superlattices*, J. Cryst. Growth **184/185**, 1190 (1998).

[109] H.W. van Kesteren, E.C. Cosman, W.A.J.A. van der Poel, and C.T. Foxon, *Fine structure of excitons in type-II GaAs/AlAs quantum wells*, Phys. Rev. B **41**, 5283 (1990).

Acknowledgement

A thesis is a result of many intellectual struggles over several years demanding both experimental and theoretical efforts. During that period, I was fortunate to be able to work in a group with an extremely enjoyable and stimulating working atmosphere. Now, I would like to use the opportunity to thank all the people that I benefitted from in one way or the other.

Above all, I would like to express my sincere gratitude to Prof.Dr. Sergey Ganichev for giving me the opportunity to work in his group and mentoring me over years. He has always been willing to listen to any problem and to provide helpful suggestions. Without his guidance and patience, this thesis would not exist in this form.

I am also greatly indebted to Dr. Sergey Danilov and Dr. Vadim Shalygin who have accompanied my experimental efforts. Numerous theoretical discussions with Prof.Dr. Eugeneous Ivchenko, Prof.Dr. Vasily Bel'kov, Prof.Dr. Sergey Tarasenko, Prof.Dr. Leonid Golub and Dr. Mischa Glasov have significantly contributed to deepen my understanding of basic and complex problems.

In addition, I would like to thank Prof.Dr. Ze-Don Kvon, Dr. Dieter Schuh and Christoph Brüne for the preparation of high quality samples.

I am very grateful to all the people who were willing to proofread drafts in various stages of this thesis: Dr. Sergey Danilov, Josef Kamann, Martin Wenger and Carl Thompson.

Over the past years, I have been sharing a room with other colleagues. I have been always been fortunate to meet these officemates that always created a pleasant working atmosphere. My deepest thanks go to Dr. Stephan Giglberger, Dr. Wolfgang Weber, Simon Seidl, Josef Kiermaier, Peter Olbrich, Johannes Karch, Vera Lechner, Juri Allerdings, Bernhard Wittmann, Christoph Brinsteiner, Thomas Schönberger, Sebastian Stachel, Josef Kamann, Christoph Drexler, Chongyun Jiang, Cynthia Karl and Faina Lomakina. With respect to the whole group, I would like to thank every member who attended and kept the „Kaffeerunde“ alive.

I acknowledge sincerely the help of Ulla Turba, Edita Neliupsyte and Aki Takahara who have supported and encouraged me.

My special thank is addressed to my mental master Shigemi Inagaki Shihan for his teachings and inspirations.

And last but not least, I thank sincerely my parents and my grandfather for all kinds of support I obtained from them.